Dynamics of Ocean Buoys and Athlete Motion for Energy Harvesting

by

Zach Ballard

Department of Mechanical Engineering and Materials Science
Duke University

Date: _____

Approved:

_____
Brian Mann, Supervisor

_____
Henri Gavin

_____
Laurens Howle

_____
Lawrie Virgin

Dissertation submitted in partial fulfillment of the requirements for the degree of Doctor of Philosophy in the Department of Mechanical Engineering and Materials Science
in the Graduate School of Duke University
2013

Abstract

Dynamics of Ocean Buoys and Athlete Motion for Energy Harvesting

by

Zach Ballard

Department of Mechanical Engineering and Materials Science
Duke University

Date: _____

Approved:

_____
Brian Mann, Supervisor

_____
Henri Gavin

_____
Laurens Howle

_____
Lawrie Virgin

An abstract of a dissertation submitted in partial fulfillment of the requirements for the degree of Doctor of Philosophy in the Department of Mechanical Engineering and Materials Science
in the Graduate School of Duke University
2013

Abstract

Small scale energy harvesting has become a prevalent area of study over the last decade. These harvesters are used in a wide range of applications, including the powering of remote sensors for structural health in buildings or bridges, tsunami, submarine and wildlife detection in the ocean, as well as general motion analysis of systems. Though many designs have been created to harvest energy for these purposes, the nonlinear dynamics of both the harvester and, when applicable, its housing (i.e. buoy casing) are widely ignored. Because of this, a significant amount of available power is lost through the limitations of linear designs.

The first part of this dissertation gives an overview of commonly used linear energy harvesting designs and gives a brief explanation of the limitations of a linear design. Both a simple inertial and linearized magnet-coil model are analytically and numerically studied. This sets the stage for improvement of energy harvesters to operate at a wider range of frequencies by including the inherent nonlinearities of the harvester and/or its environment.

In the second part, the nonlinear dynamics of ocean buoys of standard, fundamental shapes (spherical and cylindrical) due to wave loading is studied. Experimental, as well as numerical and analytical analysis is performed on these designs. Also given is a description of common wave-loading devices that can be used in a laboratory setting (wavemakers), as well as for the specific device used to obtain experimental data. Additionally, a simple dynamical system is excited by the buoy motion, which

is used to calculate the power available if the system was used as an energy harvester.

The last part of this dissertation looks at the nonlinear dynamics of human motion, with a focus on running events. Analysis is performed on running subjects in order to determine the amount of energy available, as well the frequencies where the most energy is available. This information is then used to recreate the motion numerically, which makes it possible to design a simple energy harvester that operates efficiently in such an environment. This harvester is used to power a timing mechanism that gives frequent and useful information about the athlete's position and speed.

Contents

List of Tables

List of Figures

Acknowledgements

Firstly, I'd like to thank Dr. Brian Mann for advising me throughout my graduate career, and always being available whenever I needed him. He gave me the freedom to sculpt my research into something that I would enjoy and learn a lot from.

1

Introduction

Vibratory energy harvesting is the process of collecting energy from the natural vibrations of an environment to power a device (usually small-scale, often used for monitoring or storing). In general, though ambient vibrations do not provide a significant amount of theoretically available power (milli-watt scale, at most), it is often sufficient to power devices used for specific purposes, such as monitoring the structural health of a bridge [21] . In this example, the device was designed to monitor the bridge for faults in order to prevent a catastrophic failure. Ambient vibration can come from varying sources, including ocean waves [57], temperature gradients [46], human motion [17], noise [30], and fluid-structure interaction (i.e. flutter, vortex shedding) [1].

Energy harvesting from vibratory excitation sources has also been used frequently [5, 51] to power systems where it is difficult to replace a power source. One example of this need is in deep ocean sensors where it would be difficult to periodically replace a battery. If this system were able to harvest energy from the surrounding environment, it could be continually powered without a need for replacing or repairing parts. In order to obtain the highest amount of energy from the surrounding environment, it is

essential to know the dynamic attributes of the environment, and how the harvester will respond.

The most commonly used mechanisms for energy conversion are piezoelectricity and electromagnetic induction. A diagram of each setup can be seen in Figs. 1.1 and 1.2, respectively. In general, these types of harvester devices operate most efficiently at higher frequencies. The types of excitation sources being studied, however, consist of very low frequency energy ($< 5\ Hz$). Therefore, when designing energy harvesters to operate efficiently in these scenarios, we will employ different designs that can utilize this low frequency motion.

Additionally, this research focuses more on the complex dynamics of devices that will eventually contain harvesters, such as a buoy. As with the harvesters themselves, harvester casings or containers can be tuned to create large motions in a specific forcing environment. For example, even if an energy harvesting system inside of a buoy is extremely efficient, the energy it can potentially collect is directly proportional to the motion of the buoy. Therefore, if the buoy can be designed to have a natural frequency near the most common frequencies present in a particular part of the ocean, for example, the harvester has a much larger chance of collecting large amounts of energy.

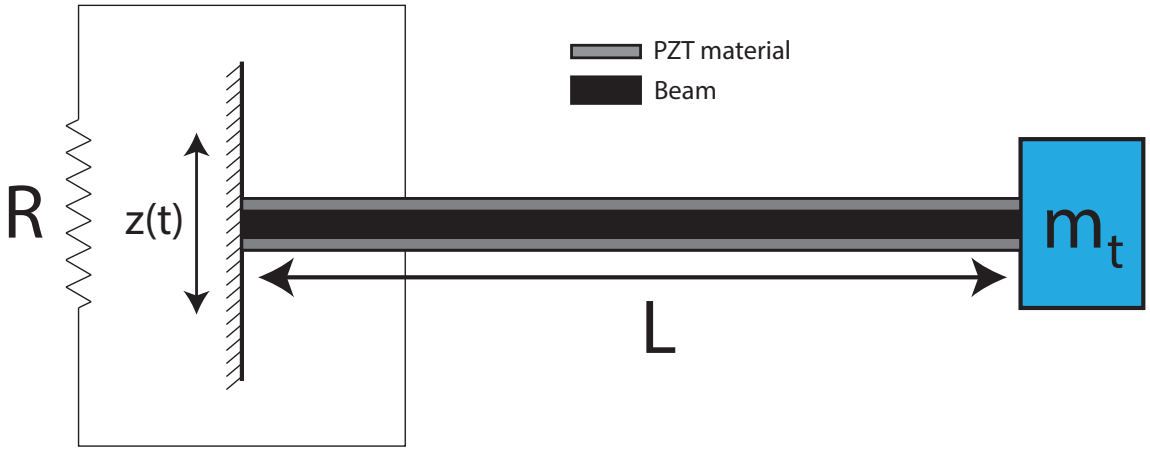

FIGURE 1.1: This figure shows a cantilevered beam that includes a tip mass m_t used for tuning. The piezoelectric material (shown in gray) allows energy to be created from the beam vibration.

Currently, the common energy harvester is a linear design. This means that large amounts of energy can be harvested at or near the system's natural frequency, but little anywhere else. For a man-made system with a known operating frequency, the harvester can be tuned to match this frequency and the linear design would be sufficient. For extracting energy from ambient vibration, however, the linear design falls short. A graphical representation of this is shown in Fig. 1.3. Since the vibration will occur at multiple frequencies which may change over time, the harvester must be able to operate at more than one frequency.

An example of a linear design can be seen in an article by Agamloh [29]. The paper describes the creation of a linear magnetic energy harvester designed to collect energy from the vertical oscillatory motion of a cylindrical buoy. In this example, not only is the harvester itself designed to be linear, only the vertical oscillations of the buoy are utilized. One of the goals of the current study is to further analyze the complex 2D/3D motion of buoys in order to utilize available motions in all directions.

In addition to a limited study of the nonlinear dynamics of vibratory energy harvesters, little emphasis is placed on the housing or external casing for these harvesters. For example, though the frequency spectrum of the waves for a specific part of the ocean may be known and the harvester may be designed to operate in this region, the size and shape of the buoy has a large effect on how this motion is transmitted from the ocean waves to the harvester. Understanding the nonlinear dynamic response of different buoy shapes can help significantly increase the efficiency of the system.

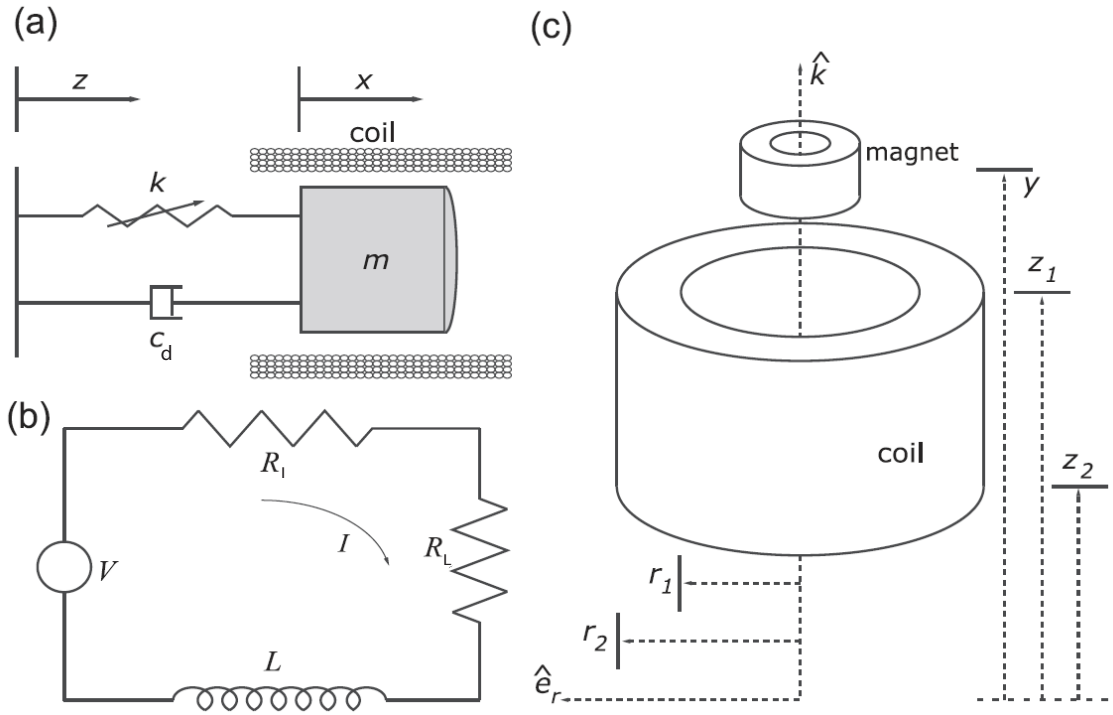

FIGURE 1.2: Taken from [51], this figure shows a common design for energy harvesting from electromagnetic induction.

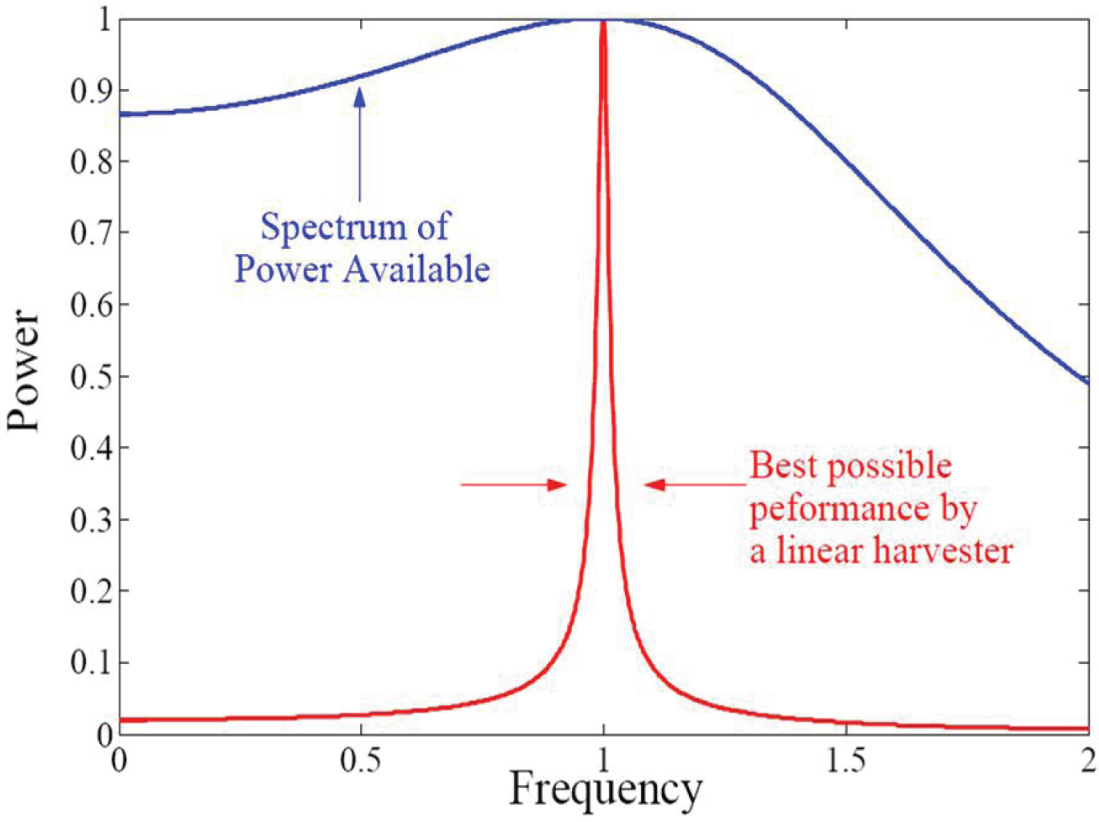

FIGURE 1.3: Taken from [60], this figure shows how linear energy harvesting designs, though efficient near the natural frequency, is extremely inefficient at all other frequencies.

1.1 Research Contributions

The main objective of this work is to analyze the nonlinear dynamics of multiple systems that have previously been simplified to a linear form or ignored completely. While the application of this research is to increase the efficiency of ambient vibratory energy harvesters, the focus is placed more on the external housing and how it interacts with the surrounding environment, as opposed to the nonlinear dynamics of the harvester itself. The dynamics of multiple systems, including ocean buoys, human motion, and a horizontal pendulum are experimentally and theoretically investigated in order to determine the prevalent frequency content and overall nonlinearity.

1.1.1 Ocean Energy Harvesters

Initially, this research focuses on how different buoy shapes interact with an external wave forcing environment. Since these systems have been traditionally studied as linear systems, the motion is both modeled inaccurately and loses potential for greater use of the vibratory environment. These shapes are studied numerically, experimentally and analytically in order to determine a full and accurate analysis of the nonlinear responses inherent in these systems.

1.1.2 Running and Walking Dynamics of the Athlete

Many studies have been performed on the dynamics of human motion, and for many activities with varying motion attributes. There have also been a wide range of studies on how to harvest energy from different aspects of this motion. The main contributions for this section will consist of a way to describe human motion through parameter identification, as well as a novel energy harvesting design that will be used for transmitting valuable data about the motion itself.

1.2 Thesis Organization

Chapter 2 provides descriptions of analytical methods commonly used in the analysis of complex nonlinear dynamical systems. This includes, but is not limited to, Harmonic Balance, Lagrange's Equation, and Numerical Continuation. Also provided are simple examples of how these methods are employed.

Chapter 3 gives a mathematical overview of common linear energy harvesting designs. The designs are solved for analytically using the analytical methods discussed in the previous chapter. These systems are shown to have a very limited bandwidth centered around the linear natural frequency. This and other shortcomings of linear systems and how they can be improved, often by incorporating inherent nonlinearities, are also discussed.

Chapter 4 provides a brief overview of the different designs of wave tanks that can be used in a laboratory setting to produce artificial waves. Since the study of different motions of multiple buoy shapes is desired, an accurate formulation of the fluid dynamics in the experimental tank is required. Forcing parameters, such as the wave height and frequency, are essential for fully understanding the experimental buoy response and how it compares to numerical simulation. Single flap, double flap and plunging wavemakers are discussed and analyzed.

The two most common and simple shapes for buoys used in energy harvesting are spherical and cylindrical. Chapter 5 and 6 derive the equations of motion for both of these systems in two dimensions. The buoys are then analyzed using analytical, numerical, and experimental methods. Relevant parameters are also varied to determine parameter sets that maximize motion, and therefore energy harvesting potential.

Chapter 7 observes the dynamics of human motion, with a focus on walking and running dynamics. Experimental data is gathered using the image processing soft-

ware implemented in previous chapters. Trials are run for multiple human subjects for a wide range of walking/running speeds. This data is then recreated numerically to determine frequencies where the largest amount of energy is available. In addition, a harvester is designed in order to collect energy from the subjects motion. This energy will potentially be used in order to power an intelligent measurement device.

2

Theoretical Methods

This chapter describes some of the commonly used tools and analytical methods for determining equations of motion and general behavior of dynamical systems. Most of the systems being studied are too complex to be analyzed with simpler methods (i.e. force balance). In order to fully understand the nonlinear and/or multi-frequency motion of these systems, multiple methods for deriving equations of motion and solving nonlinear equations are employed. This includes, but isn't limited to, Lagrange's equation, harmonic balance, and numerical continuation.

2.1 Lagrange's Equation

Lagrange's equation is an energy-based method that uses the energy of a system to derive the governing equations of motion. The generalized form of Lagrange's equation is written as

$$\frac{d}{dt}\left(\frac{\partial T}{\partial \dot{q}}\right) - \frac{\partial T}{\partial q} + \frac{\partial V}{\partial q} = Q \tag{2.1}$$

where T and V are the kinetic and potential energies respectively, q is the generalized coordinate, and Q is the generalized force. For example, consider the simple spring-mass system shown in Fig. 2.1. The formulas for the energy of this system are

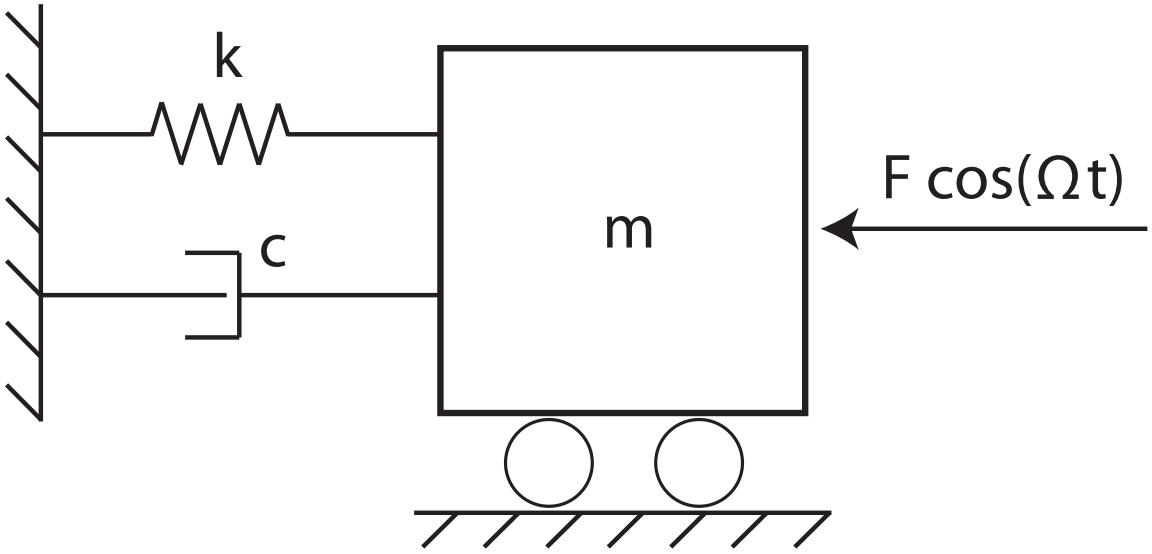

FIGURE 2.1: Simple spring-mass-damper system with spring constant k, damping coefficient c, and mass m.

$$T = \frac{1}{2}m\dot{x}^2, \;\; V = \frac{1}{2}kx^2. \tag{2.2}$$

The dissipation of the system can be taken into account using the Rayleigh dissipation function, which is defined as

$$R = \frac{1}{2}c\dot{x}^2. \tag{2.3}$$

This term can be incorporated into Eqn. 2.1, resulting in a final Lagrangian of

$$\frac{d}{dt}\left(\frac{\partial T}{\partial \dot{q}}\right) - \frac{\partial T}{\partial q} + \frac{\partial V}{\partial q} + \frac{\partial R}{\partial \dot{q}} = Q \tag{2.4}$$

Choosing x as the generalized coordinate and plugging the energies and external force into Eqns. 2.4, the equation becomes

$$\frac{d}{dt}(m\dot{x}) - 0 + c\dot{x} + kx = F\cos\Omega t \tag{2.5}$$

which gives the equation of motion

$$m\ddot{x} + c\dot{x} + kx = F\cos\Omega t. \tag{2.6}$$

2.2 Harmonic Balance

Harmonic balance is a method used to find an analytical solution to a system exhibiting oscillatory motion. As the name suggests, the solution (x, for example) is assumed to be harmonic, such as

$$x = A\sin\Omega t + B\cos\Omega t \quad \text{or} \quad r\cos(\Omega t + \phi) \tag{2.7}$$

where Ω is the forcing frequency, $r = \sqrt{A^2 + B^2}$, and the phase shift ϕ is

$$\phi = \arctan\frac{A}{B}. \tag{2.8}$$

This solution is then plugged into the equation of motion and the harmonics ($\sin\Omega t$,$\cos\Omega t$) are balanced, which gives algebraic equations used to solve for the response. As an example, consider the same system shown in Fig. 2.1. First, c is written as $2\zeta\omega_n$, where ζ is the damping ratio and $\omega_n = \sqrt{k/m}$ is the natural frequency of the system. Plugging in the first solution form from Eqn. 2.7, the equation of motion becomes

$$\begin{aligned}\left(-mA\Omega^2 - 2\zeta\omega_n B\Omega + kA\right)\sin\Omega t + \\ \left(-mB\Omega^2 + 2\zeta\omega_n A\Omega + kB\right)\cos\Omega t = F\cos\Omega t\end{aligned} \tag{2.9}$$

Grouping the sin and cos terms and solving gives

$$A = \frac{2B\zeta\omega_n\Omega}{m(\omega_n^2 - \Omega^2)} \quad \text{and} \quad B = \frac{F(\omega_n^2 - \Omega^2)}{m((\omega_n^2 - \Omega^2)^2 + (2\zeta\omega_n\Omega)^2)} \tag{2.10}$$

Simplifying these equations and solving for the magnitude r gives

$$r = \frac{F/m}{\sqrt{(\omega_n^2 - \Omega^2)^2 + (2\zeta\omega_n\Omega)^2}} \tag{2.11}$$

2.3 Numerical Continuation

Another helpful method for determining responses of nonlinear systems is numerical continuation. Numerical continuation is a broad area of study which includes multiple methods for determining approximate solutions to nonlinear equations/systems of equations. As an example, say there is a system of ordinary differential equations, such as

$$\dot{x} = F(x, \lambda) \tag{2.12}$$

where x is the state vector and λ is a specific parameter. If the function $F(x, \lambda)$ is smooth, it's possible for there to be an equilibrium solution x_0 and parameter λ_0 where

$$f(x_0, \lambda_0) = 0. \tag{2.13}$$

Once this initial solution is found, λ can be slowly varied to determine new equilibrium solutions. In this instance, we are performing numerical continuation for only one parameter.

There are different methods to determine an initial guess for the equilibrium solution as the parameter is varied. These methods often have trade-offs between speed and accuracy, and have different benefits for specific systems/equations. Firstly,

there is tangent continuation. For this method, the slope of the equilibrium curve in the $x - \lambda$ plane is determined at the equilibrium point x_n with parameter value λ_n. The initial guess for x_{n+1} is then simply the point that intersects the tangent line and the new parameter value λ_{n+1}, as is shown in Fig. 2.2. This method of

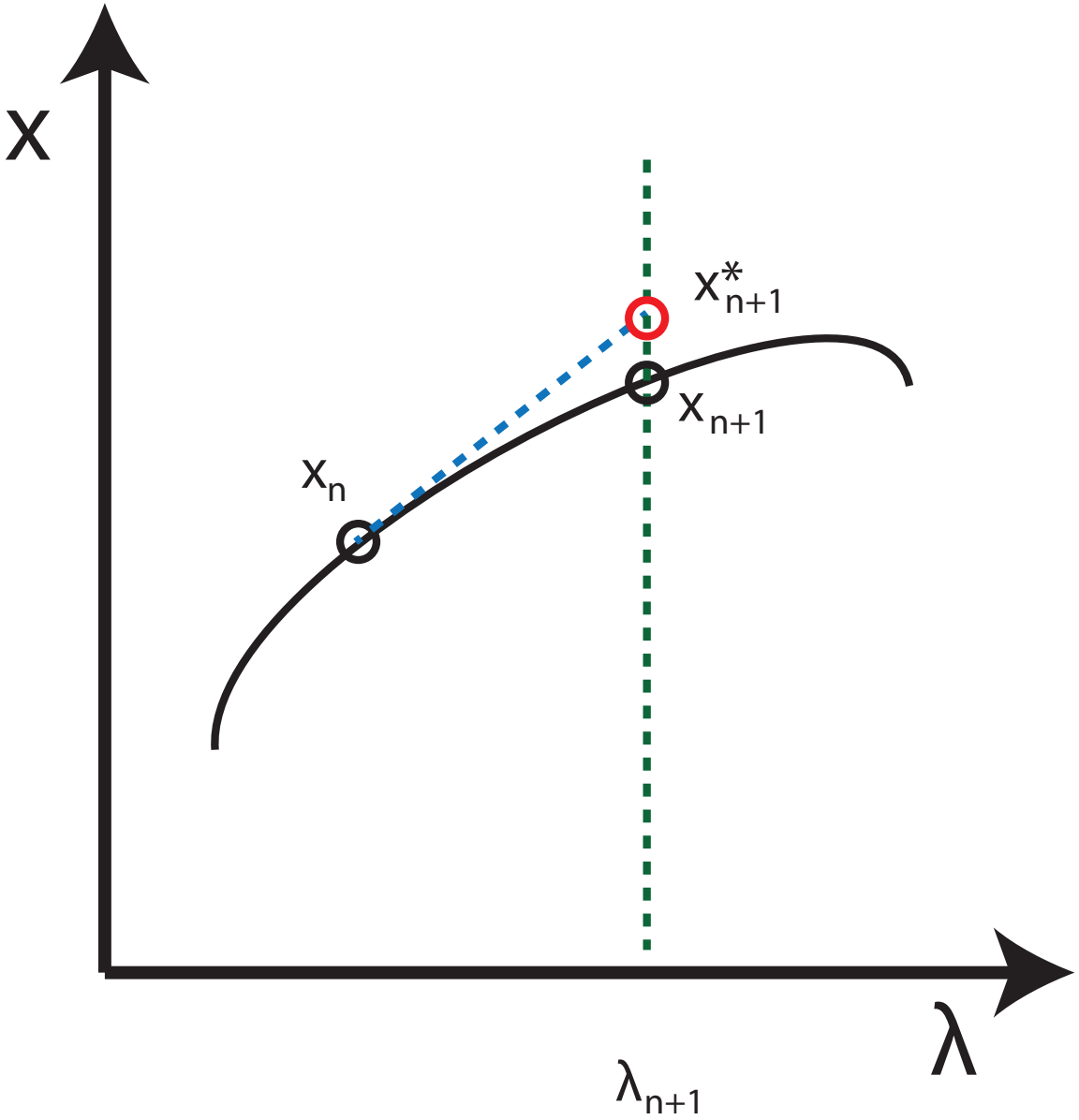

FIGURE 2.2: Illustration of the tangent prediction for numerical continuation. Shows the initial guess x^*_{n+1} and the corrected value x_{n+1}

guessing, however, is slow and often inaccurate. The method is generally improved

by adding an additional constraint to the system. The most common way of doing this is called pseudo-arclength continuation. In addition to Eqn. 2.13, we add the constraint equation

$$(\lambda - \lambda_0)\dot{\lambda} + (x - x_0)\dot{x} - \delta s = 0, \tag{2.14}$$

where δs is the change in arclength s. By enforcing this constraint, the continuation method can continually change step size, which is helpful for increasing the rate of calculation, as well as handling sharp curves in the plane. This method is used briefly in the following chapters in order to validate previously derived numerical and analytical solutions.

2.3.1 Numerical Continuation Example

Consider the system

$$\dot{x} = x^2 - \lambda, \tag{2.15}$$

which is a common example of a system with a saddle node bifurcation, and can be seen in Fig. 2.3. In this equation, λ is the bifurcation parameter. As this value changes, the number of fixed points, as well as their stability, are altered. The three scenarios can be seen in Table 2.1. This system, of course, is directly solvable. However, the process used in this example can be applied to a system without the need for an analytical solution. A helpful diagram showing the algorithm for numerical continuation can be seen in Fig. 2.4.

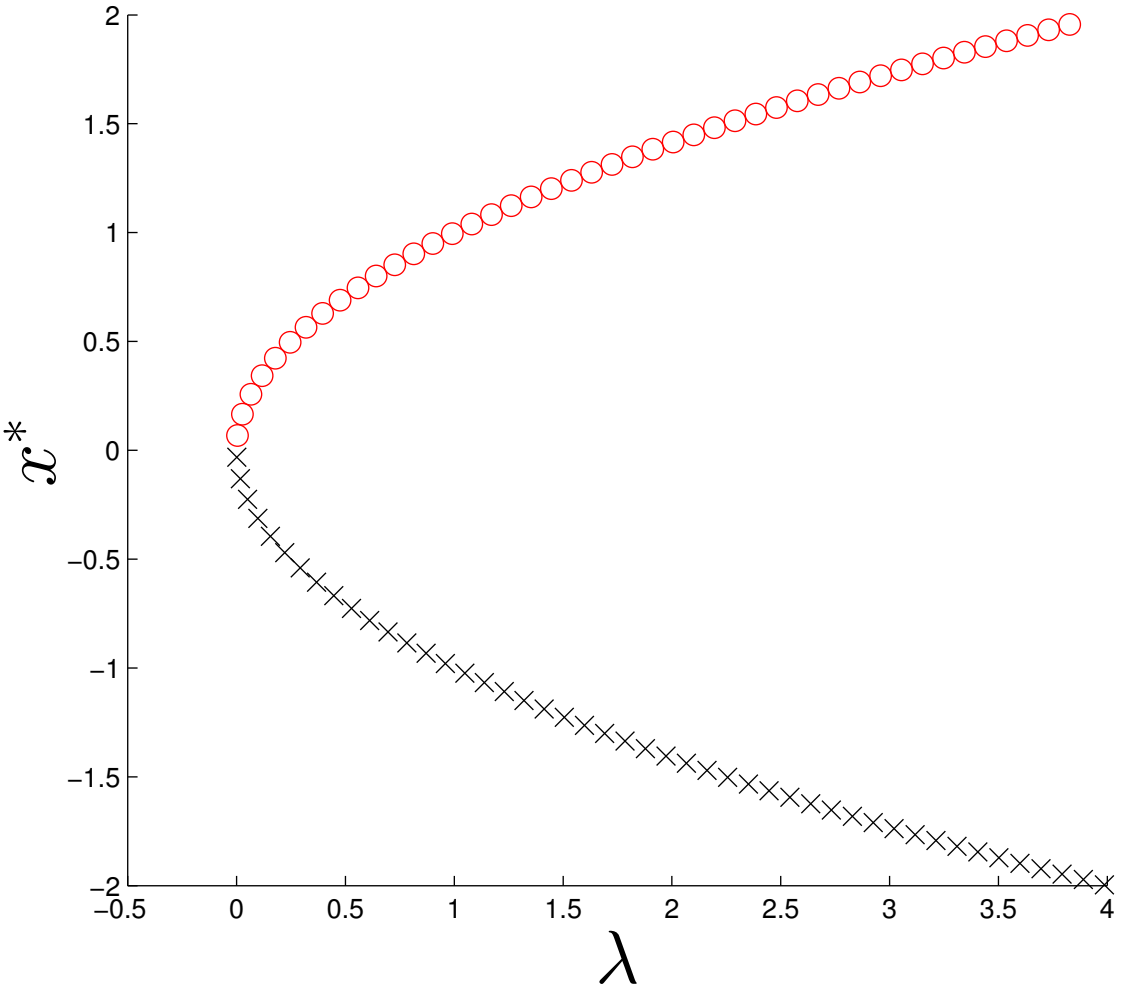

FIGURE 2.3: Saddle node bifurcation with stable points shown as black x's and unstable points shown as red o's.

Table 2.1: Fixed Points and Stability of Saddle Node Bifurcation System

λ	Fixed Points	Stability
< 0	none	-
$= 0$	0	saddle
> 0	$-\sqrt{\lambda}$, $\sqrt{\lambda}$	stable, unstable

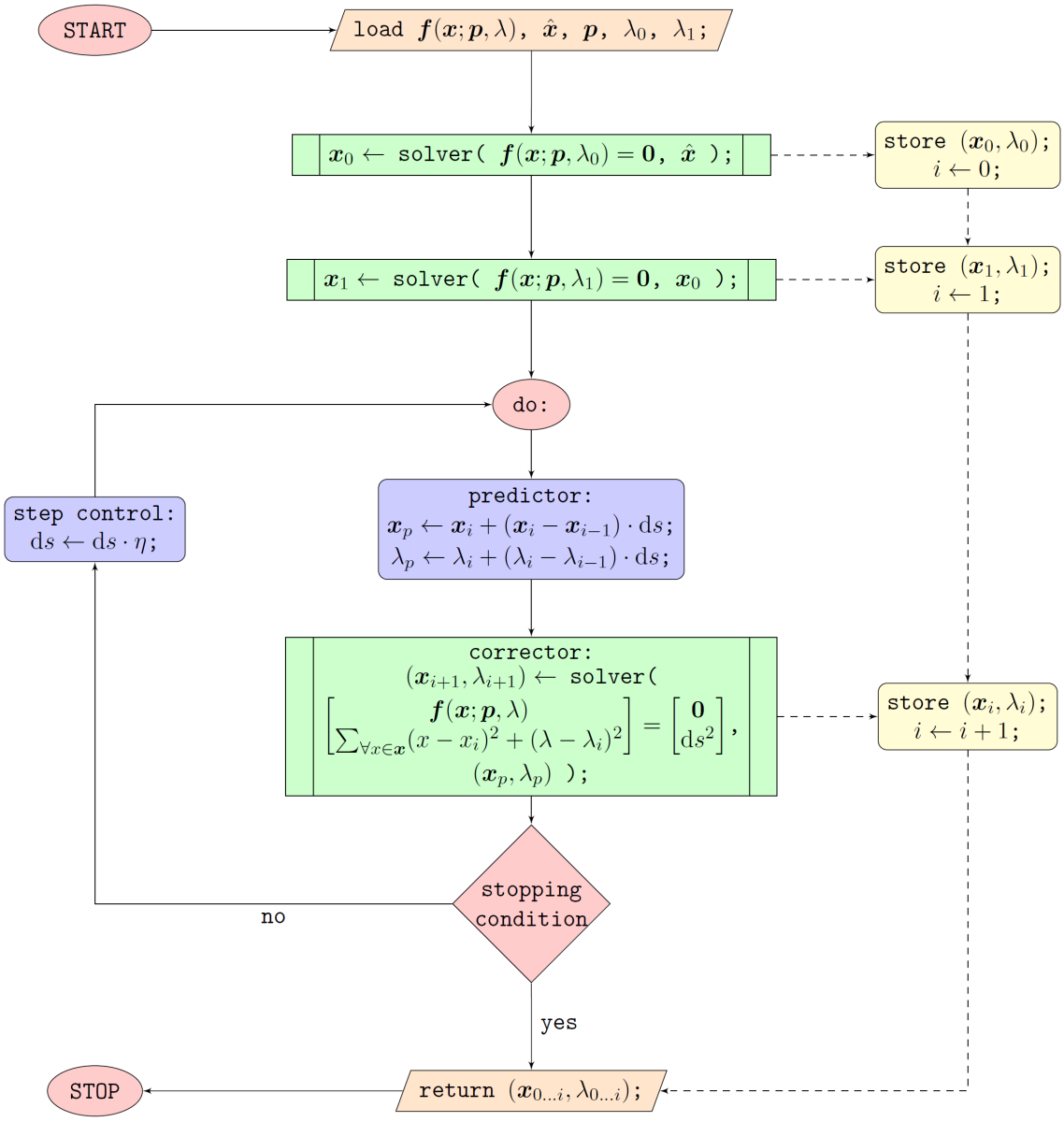

FIGURE 2.4: Provided by [Clark McGehee], flowchart of numerical continuation algorithm.

3

Linear Energy Harvesting

This chapter derives the governing equations for multiple linear designs. Additionally, the response of each system is investigated. Though a nonlinear harvester will be designed and eventually be used, understanding the linear case is preparatory to studying the more complex nonlinear systems.

3.1 Base-Excited Mechanical Oscillator

A common and simple form of an energy harvester is normally represented as a second order spring-mass-damper system, a diagram of which can be seen in Fig. 3.1. The external vibration source $v(t)$ causes the oscillation $z(t)$ of the mass m. The harvested energy is that which is dissipated within the damper, and is extracted through a transduction mechanism. The equation of motion for this system is written as

$$m[\ddot{z}(t) + \ddot{v}(t)] + c_t\dot{z} + kz(t) = 0, \tag{3.1}$$

where c_t is the damping coefficient, k is the spring constant, and $v(t)$ is defined as

$$v(t) = V \sin(\Omega t) \tag{3.2}$$

This equation assumes the motion of the mass $z(t)$ does not have a large effect on the external vibration $v(t)$. Assuming a sinusoidal response, the steady-state solution to this equation becomes

$$z(t) = \frac{\Omega^2}{\sqrt{(\frac{k}{m} - \Omega^2)^2 + (\frac{c_t \Omega}{m})^2}} V \sin(\Omega t - \phi), \tag{3.3}$$

and the phase shift is written as

$$\phi = \tan^{-1}\left(\frac{c_t \Omega}{k - \Omega^2 m}\right) \tag{3.4}$$

From Eq. 3.3, it becomes obvious that the maximum energy is gained when the excitation frequency becomes $\sqrt{k/m}$, which is the natural frequency of the system ω_n. The average power dissipated per cycle can be solved by assuming

$$P_d = \frac{1}{T} \int_0^T (c_t \dot{z})\, \dot{z}\, dt, \tag{3.5}$$

which results in

$$P_d = \frac{m \zeta_t V^2 \left(\frac{\Omega}{\omega_n}\right)^3 \Omega^3}{\left[1 - \left(\frac{\Omega}{\omega_n}\right)^2\right]^2 + \left[2\zeta_t \left(\frac{\Omega}{\omega_n}\right)\right]^2}, \tag{3.6}$$

where ζ_t is the damping ratio, written as

$$\zeta_t = \frac{c_t}{2 m \omega_n}. \tag{3.7}$$

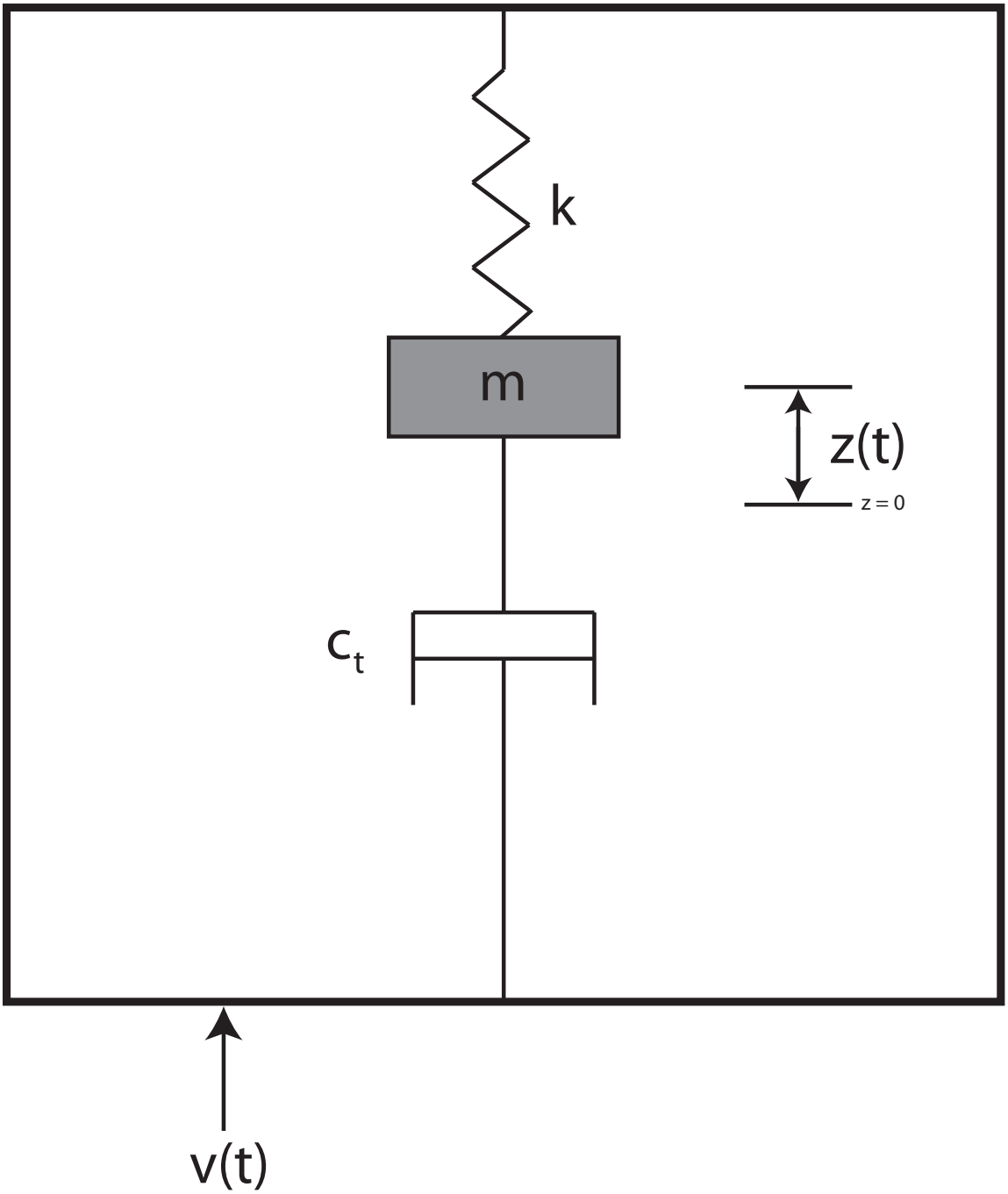

FIGURE 3.1: Inertial linear energy harvester with mass m, spring k and damper c_t, which includes parasitic losses and those due to energy extracted through transduction.

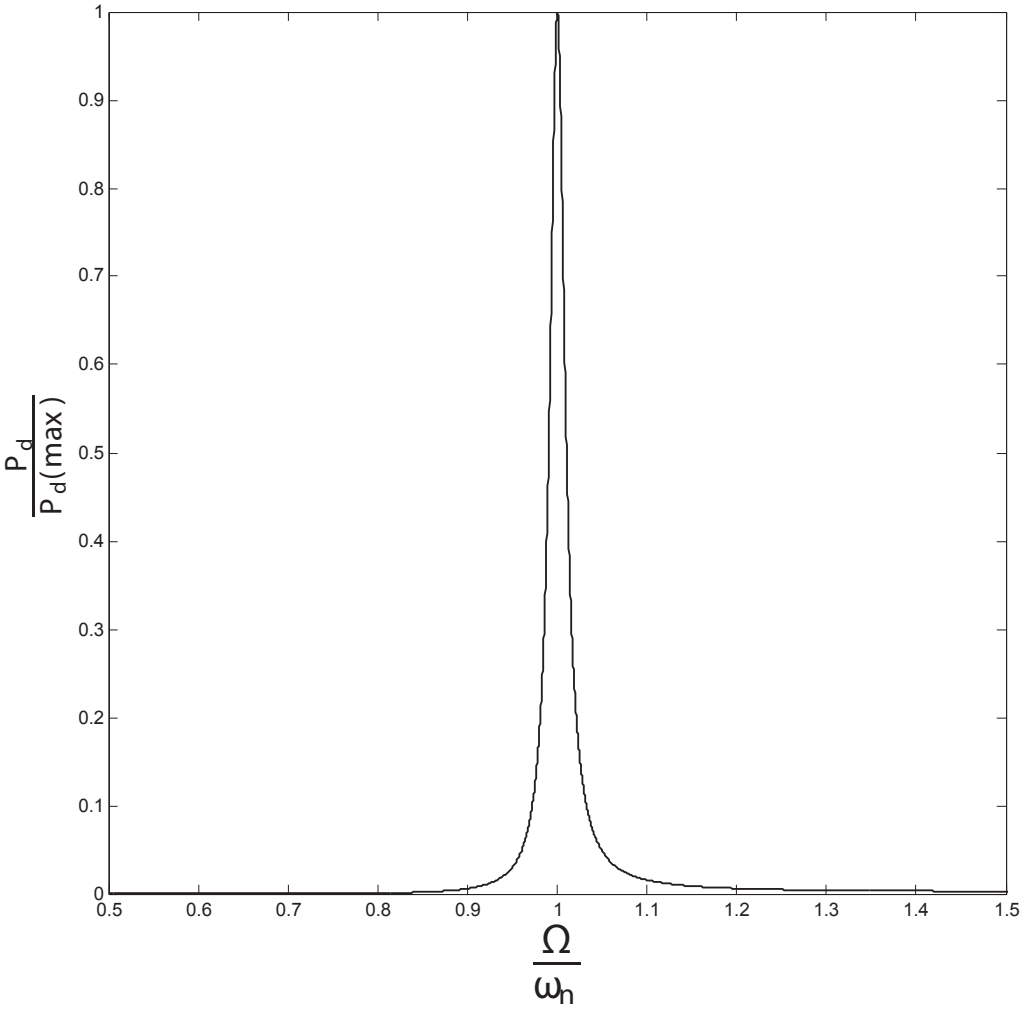

FIGURE 3.2: Response of the harvester with varying excitation frequency Ω. Shows the narrow bandwidth of the harvester: has a large response near the natural frequency ω_n but a significantly smaller response at all other frequencies.

3.2 Coupled Electromechanical Harvester

Another common energy harvester that is modeled as a linear system is the magnet-coil harvester, shown in Fig. 3.3. This system uses electromagnetic induction in order to convert energy. The derivation of the equations of motion will be performed using Lagrange's equation, as in [51]. First, the kinetic energy of the system can be written as

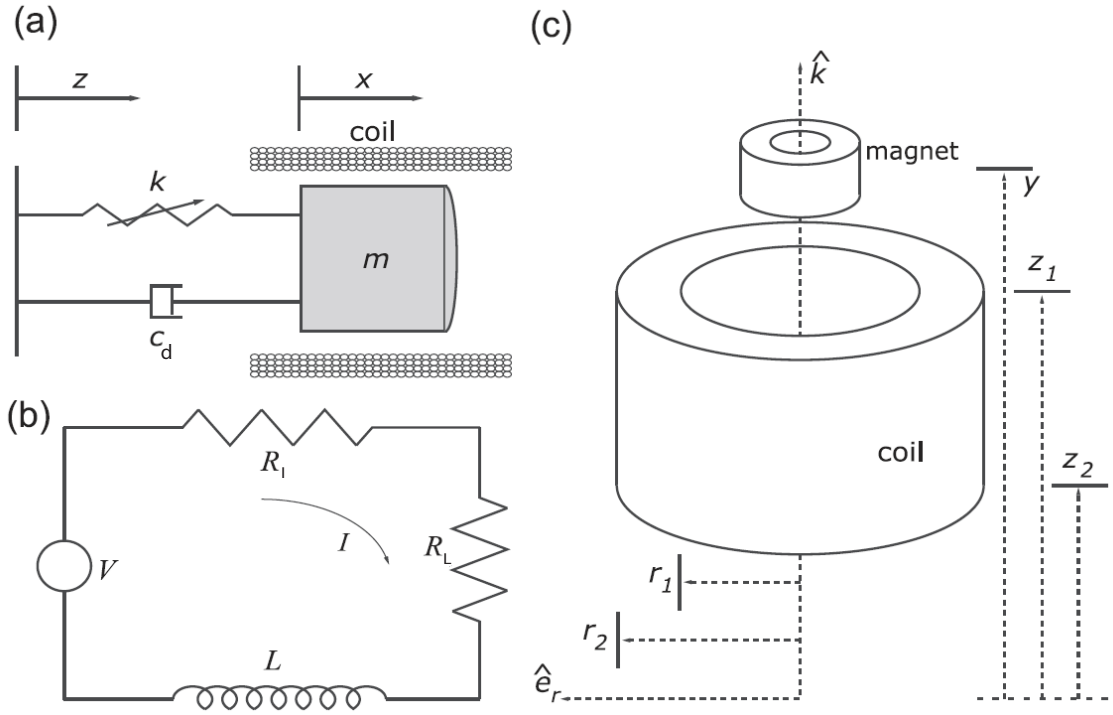

FIGURE 3.3: Taken from [51], this diagram shows a) the mechanical system, b) the electrical circuit, and c) the coil and magnet

$$T = \frac{1}{2}m\dot{x}^2 + \frac{1}{2}L\dot{q}^2 + \Theta\dot{q}y \tag{3.8}$$

where x is the position of the mass m, L is the inductance, q is a generalized coordinate for charge, Θ is a coupling coefficient for the transducer (with units of $\frac{Coulombs \cdot Ohms}{meter}$), and y is the relative position between between the mass and the base of the system, or $x - z$. The potential energy can be written as

$$U = \frac{1}{2}ky^2 \tag{3.9}$$

where k is an equivalent spring constant for the linear case. The equation for the dissipated power in the system is described as

$$D = \frac{1}{2}c_d\dot{y}^2 + \frac{1}{2}(R_E + R_I)\dot{q}^2. \tag{3.10}$$

where c_d is a linear dissipation constant and R_E and R_I are the external load and internal coil resistances, respectively. Using Lagrange's equation in terms of the relative position y and dividing by the mass m, the equation of motion becomes

$$\ddot{y} + 2\zeta\omega_n\dot{y} + \omega_n^2 y - \frac{\Theta}{m}I = \Gamma \sin \Omega t \tag{3.11}$$

where $\omega_n = \sqrt{k/m}$ is the natural frequency, $\zeta = c_d/2m\omega_n$ is the damping ratio, $\Gamma = A/m$ is the excitation amplitude, and $\dot{q}$ has been replaced by the current I. The differential equation for the electrical system can be written as

$$\dot{I} + \rho I + \frac{\Theta}{L}\dot{y} = 0 \tag{3.12}$$

where $\rho = (R_E + R_I)/L$ is the ratio of total resistance to the inductance, and is also representative of the ratio of the current response rate to that of the velocity.

3.2.1 Analytical Linear Coupling Response

By assuming solutions of the form $y = C_1 \sin \Omega t + C_2 \cos \Omega t$ and $I = C_3 \sin \Omega t + C_4 \cos \Omega t$, plugging them into Eqs. 3.11 and 3.12 and balancing harmonics, the following four equations are produced

$$-2\zeta\omega_n\Omega C_1 + (\Omega^2 - \omega_n^2)C_2 + \frac{\Theta}{m}C_4 = 0, \tag{3.13}$$

$$(\Omega^2 - \omega_n^2)C_1 + 2\zeta\omega_n\Omega C_2 + \frac{\Theta}{m}C_3 + \Gamma = 0, \tag{3.14}$$

$$-\frac{\Theta}{L}\Omega C_1 - \Omega C_3 - \rho C_4 = 0, \tag{3.15}$$

$$\frac{\Theta}{L}\Omega C_2 + \Omega C_4 - \rho C_3 = 0. \tag{3.16}$$

C_3 and C_4 are then found in terms of the dynamic responses C_1 and C_2 and written as

$$C_3 = \frac{\Theta\Omega}{L}\frac{\rho C_2 - \Omega C_1}{\rho^2 + \Omega^2} \tag{3.17}$$

and

$$C_4 = \frac{\Theta\Omega}{L}\frac{\rho C_1 + \Omega C_2}{\rho^2 + \Omega^2}. \tag{3.18}$$

Now the solution form for the mechanical response is changed to

$$y = r\cos(\Omega t + \phi) \tag{3.19}$$

where $r^2 = C_1^2 + C_2^2$ and ϕ is the phase shift. By plugging the equations for C_3 and C_4 back into Eqs. 3.13 and 3.14, squaring and adding the results and solving, the mechanical response amplitude r is found to be

$$r = \frac{\Gamma}{\sqrt{\left(2\zeta\omega_b\Omega + \frac{\Omega\rho\Theta^2}{mL(\rho^2+\Omega^2)}\right)^2 + \left(\left(1 - \frac{\Theta^2}{mL(\rho^2+\Omega^2)}\right)\Omega^2 - \omega_n^2\right)^2}} \tag{3.20}$$

and using Eqs. 3.17 and 3.18, the electrical response becomes

$$I = \sqrt{C_3^2 + C_4^2} = \frac{\Omega\Theta}{L\sqrt{\rho^2 + \Omega^2}} \tag{3.21}$$

Figure 3.4 shows the frequency response of the mechanical system with a small coupling coefficient Θ, and the power is shown in Fig. 3.5. The dissipated power can be found by using Eq. 3.21 and the relationship

$$P = I^2 R. \tag{3.22}$$

As seen in Fig. 3.4, the system has a large response at its natural frequency ω_n but significantly less when that frequency is varied. This shows the main disadvantage of using linear systems for energy harvesting: a usable amount of energy can only be gained if the harvester operates at a frequency close to the natural frequency. Operating anywhere else would make the harvester extremely inefficient. Since a large majority of excitation sources that can be used to harvest energy have varying frequencies, this is not an ideal design.

Additionally, the amount of energy harvested is greatly dependent not only on the mechanical parameters, but those of the electrical components. For example, changing the value of the resistor has a significant effect on the efficiency of the system. This can be seen in Fig. 3.6. In this figure, the potential power is shown to have a maximum located where the external resistance R_E is equal to that of the internal coil resistance R_I.

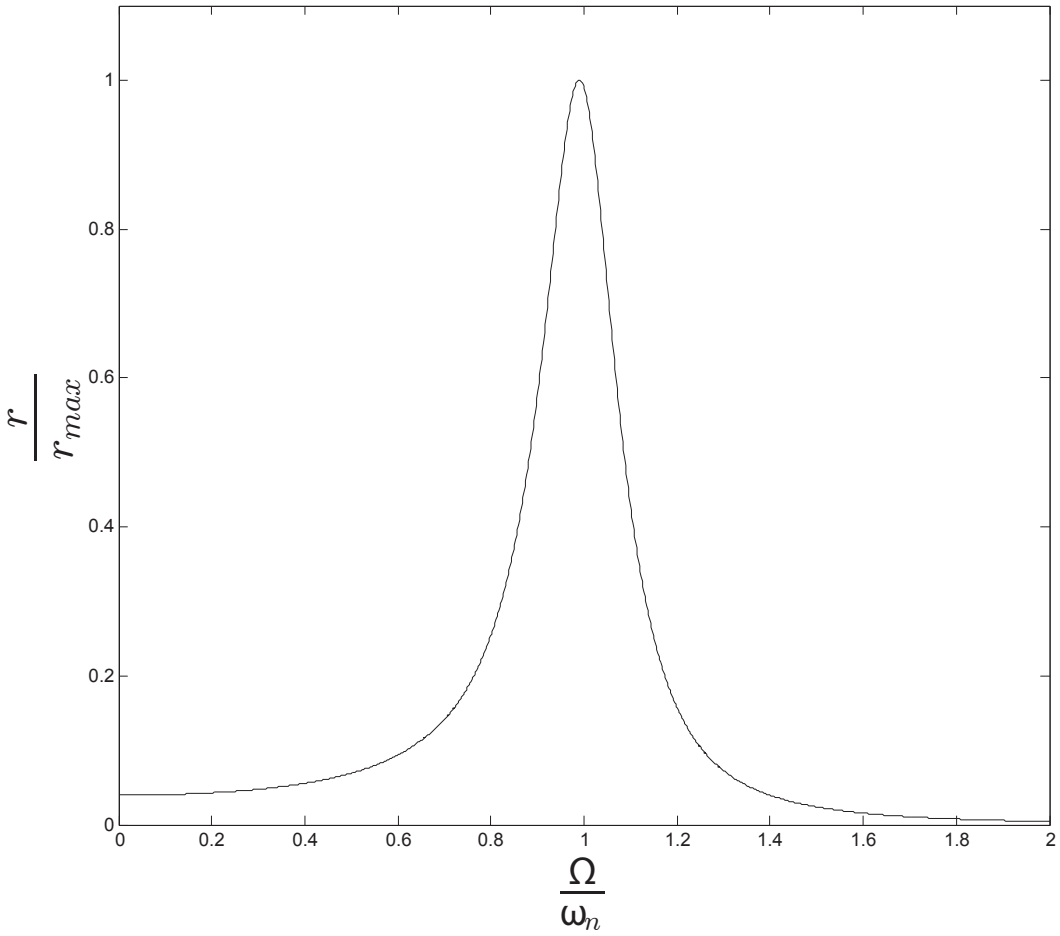

FIGURE 3.4: Frequency response of mechanical amplitude r for the coupled linear oscillator with a small coupling coefficient (0.1).

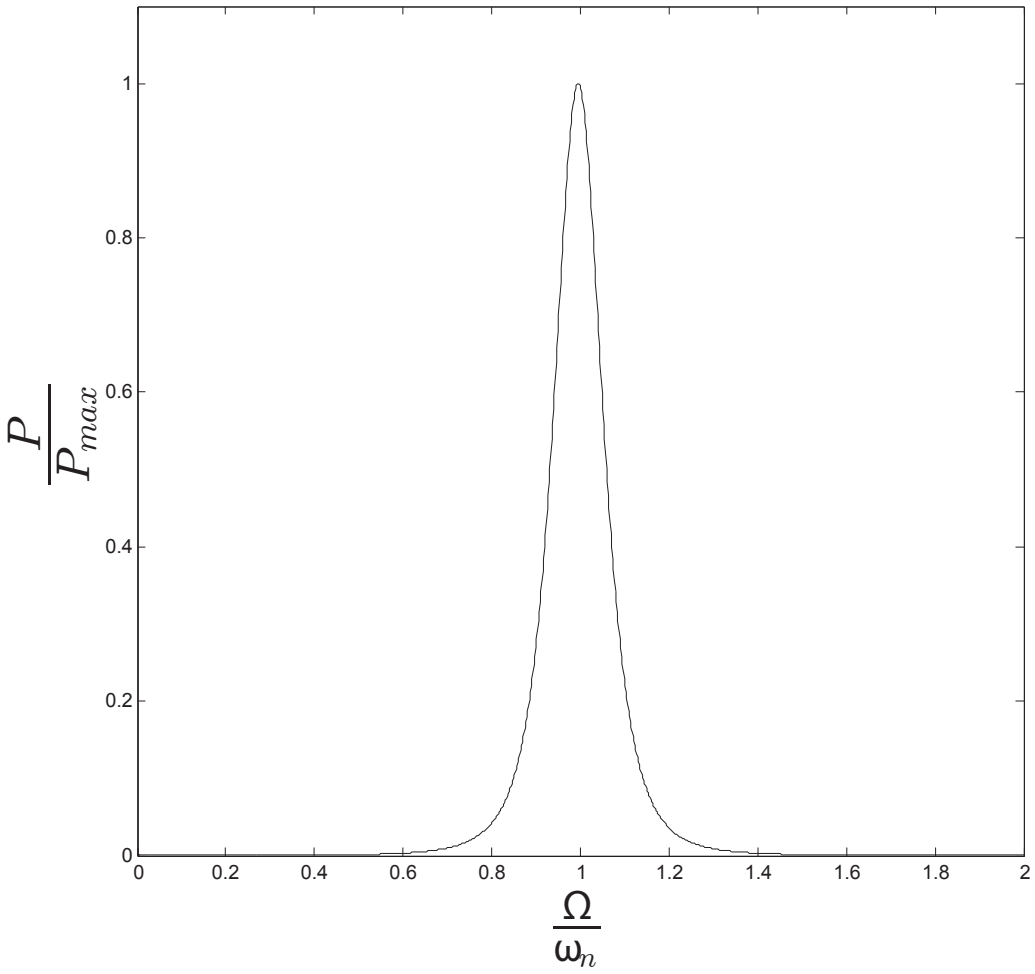

FIGURE 3.5: Frequency response of power for the coupled linear oscillator.

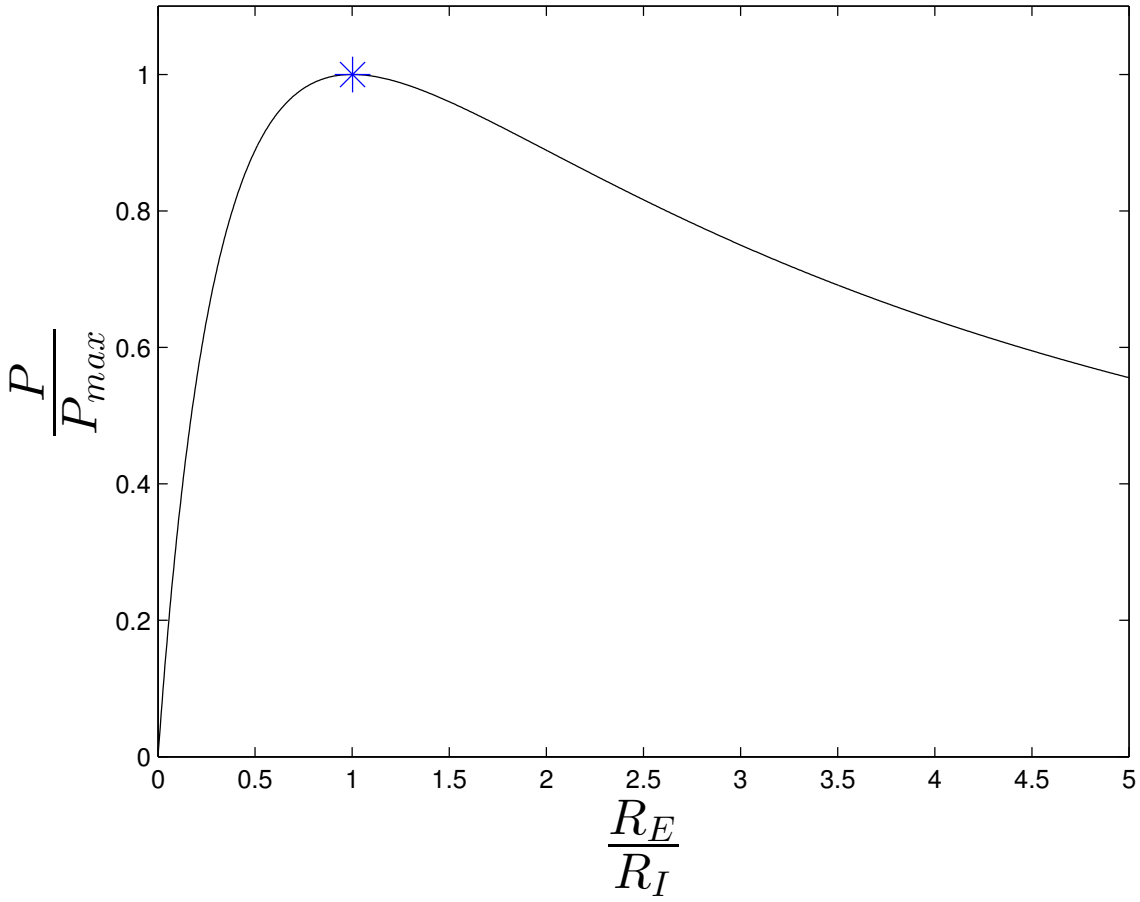

FIGURE 3.6: Response amplitude dependence on the variation of the resistive load.

3.3 Conclusions

Linear analyses of energy harvesting systems serve to simplify complex mechanisms and make them more manageable. However, this linearization often neglects important attributes that could greatly increase the system efficiency. For single-frequency systems, such as man-made devices, a linear model can be sufficient. For the ambient vibratory environments observed in this research, however, such a model in largely insufficient. This inefficiency is due to the fact that, since these ambient environments have multiple and varying frequencies, a single frequency model cannot fully capture the large spectrum of energy available. It is therefore important to study the nonlinearities inherent in such systems in order to have a more accurate and potentially more beneficial model of the harvester.

4

Wave Tanks

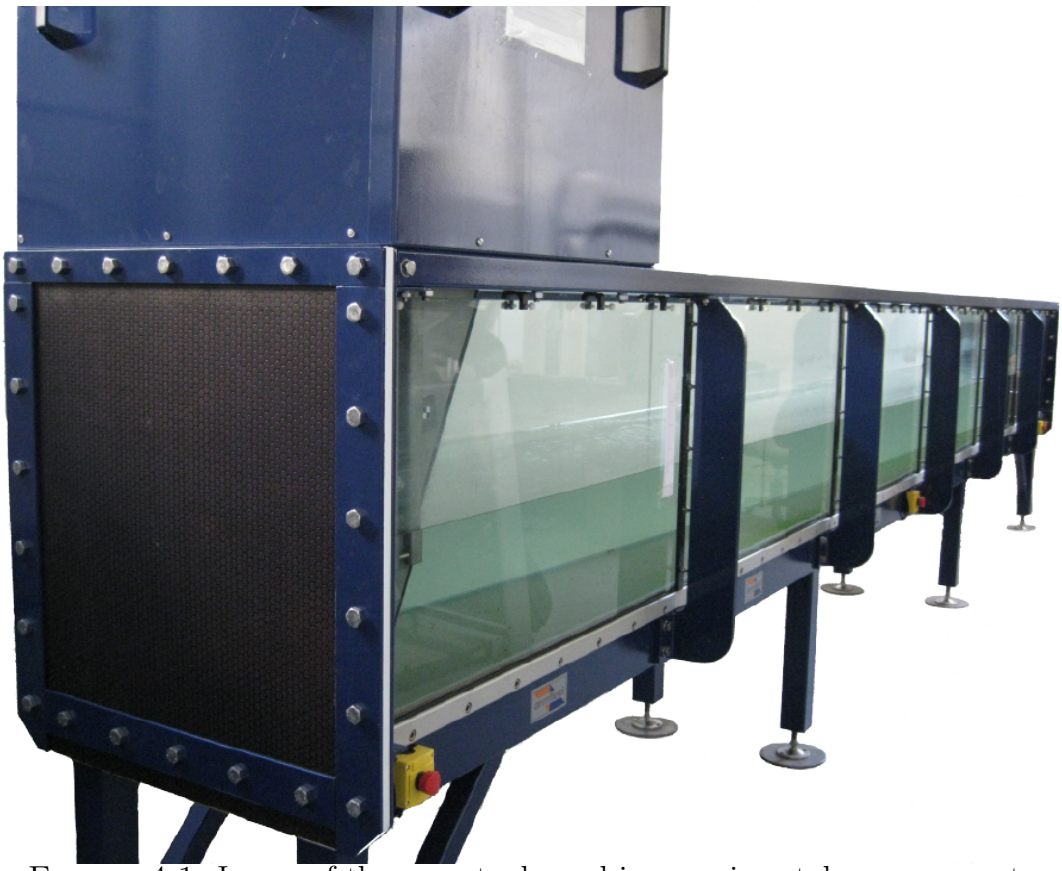

FIGURE 4.1: Image of the wave tank used in experimental measurements

Multiple methods have previously been used to describe fluid motion in a wave tank, including techniques of computational fluid dynamics (CFD) and utilization of fluid dynamics equations such as Navier-Stokes [49, 27, 9]. In implementations of analytical solutions for the fluid motion, the tank often has to be "idealized" due to the inherent complexity of the system. For example, assumptions are made about the reflectivity of the tank (i.e. non-reflective) and other boundary conditions.

There are many types of tanks used in engineering to emulate ocean or sinusoidal waves in an experimental environment. This ranges from large-scale devices used to simulate the effects of a tsunami, to small-scale devices such as the one utilized here for experimental data. Additionally, there are many different designs on this small scale. Each of these designs has their own properties and benefits, which will be covered in this section. Knowing the theory behind these wavemakers gives a wider understanding to the types of waves they create and how they can be modeled.

4.1 Single Flap Wavemakers

The single flap wavemaker is one of the most common types of wavemaker, which is mainly due to its simple setup. As shown in Fig. 4.2, the system consists of a flap that rotates between two positions at a desired frequency ω, which creates the traveling wave. According to Galvin [12], for shallow water applications, the water displaced per stroke of the flap should be equal to the crest volume of the traveling wave (shown in gray in Fig. 4.2). If S is the stroke of the flap at the SWL (still water level), then

$$\text{Unit volume displaced by flap} = \frac{1}{2}Sd, \tag{4.1}$$

where d is the distance from the SWL to the flap hinge. Galvin then solved for the unit volume of water in a wave crest with amplitude A and wave number $k = \frac{2\pi}{L}$,

showing that

$$\int_0^{\frac{L}{2}} A \sin kx dx = \frac{A}{k}\left(1 - \cos\frac{1}{2}kL\right) = \frac{2A}{k}, \tag{4.2}$$

where L is the wavelength of the traveling wave. Therefore, the two unit volumes can be equated to get the wave amplitude due to the flap parameters. This results in

$$A = \frac{1}{4}kdS \tag{4.3}$$

Knowing this, the velocity potential [38] for the traveling wave Φ can be written as

$$\Phi(x, z, t) = -\frac{Ag}{\omega}\frac{\cosh k(h+z)}{\cosh kh}\sin(\omega t - kx), \tag{4.4}$$

where h is the water depth.

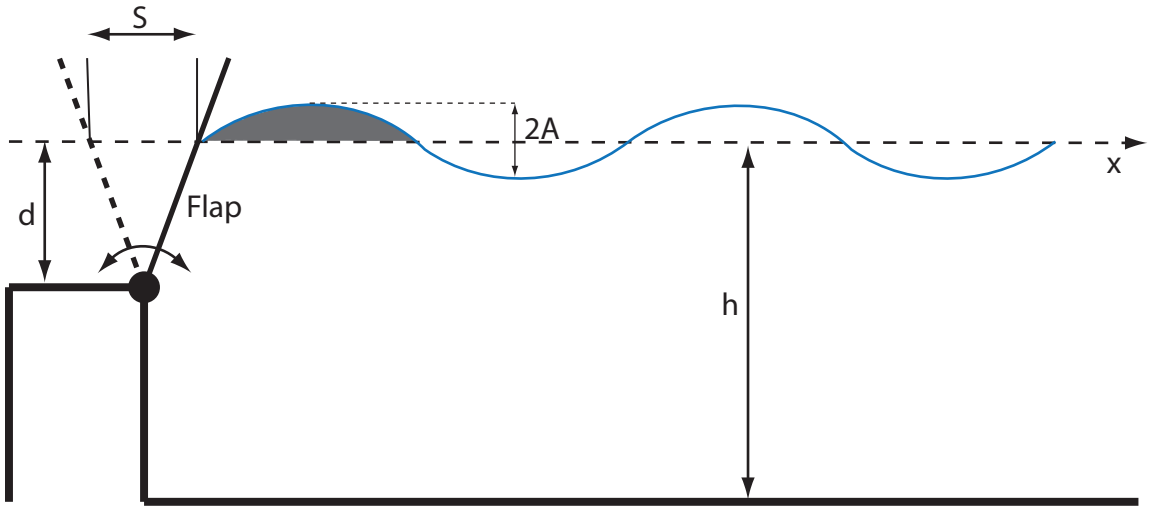

FIGURE 4.2: Diagram of a single flap wavemaker.

4.2 Double Flap Wavemakers

Kusumawinahyu [33] demonstrates the properties of double flap wavemakers. As shown in Fig. 4.3, this system consists of two flaps that can operate at different frequencies. In the cases where the flaps are moving together or one flap is moving while one is stationary, the single flap formulation is sufficient to describe the system. However, if the two flaps are both moving at different frequencies, the system must be described differently. By describing the separate stroke lengths (S_1, S_2), depths (d_1, d_2) and frequencies (ω_1, ω_2), it can be shown that

$$\Phi(x,z,t) = -\frac{A_1 g}{\omega_1}\frac{\cosh k_1(h+z)}{\cosh k_1 h}\sin(\omega_1 t - k_1 x) - \frac{A_2 g}{\omega_2}\frac{\cosh k_2(h+z)}{\cosh k_2 h}\sin(\omega_2 t - k_2 x), \quad (4.5)$$

where A_1 and A_2 can be found from the single flap theory. One of the benefits of this design is the fact that a traveling wave with multiple frequencies and amplitudes can be created.

4.3 Plunging Wavemakers

The third type of common wavemaker is the plunging wavemaker, shown in Fig. 4.4. This is also the type of wavemaker used for the experimental sections of the analysis for both the spherical and cylindrical buoys. Though this specific design is not covered in the Kusumawinahyu paper, it can be assumed that it acts much like the single flap setup; i.e. wave height is proportional to the amount of water displaced per stroke. The fluid dynamics throughout the tank with this particular wavemaker are derived again in the next section.

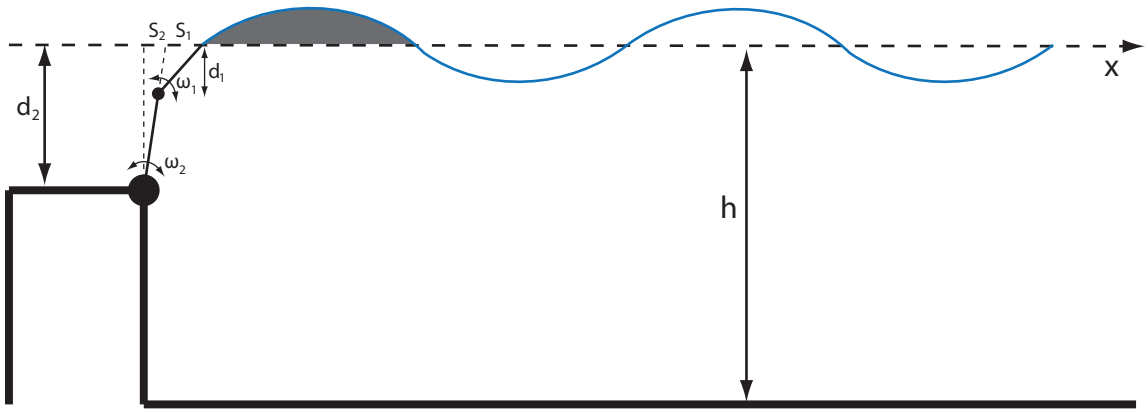

FIGURE 4.3: Diagram of a double flap wavemaker.

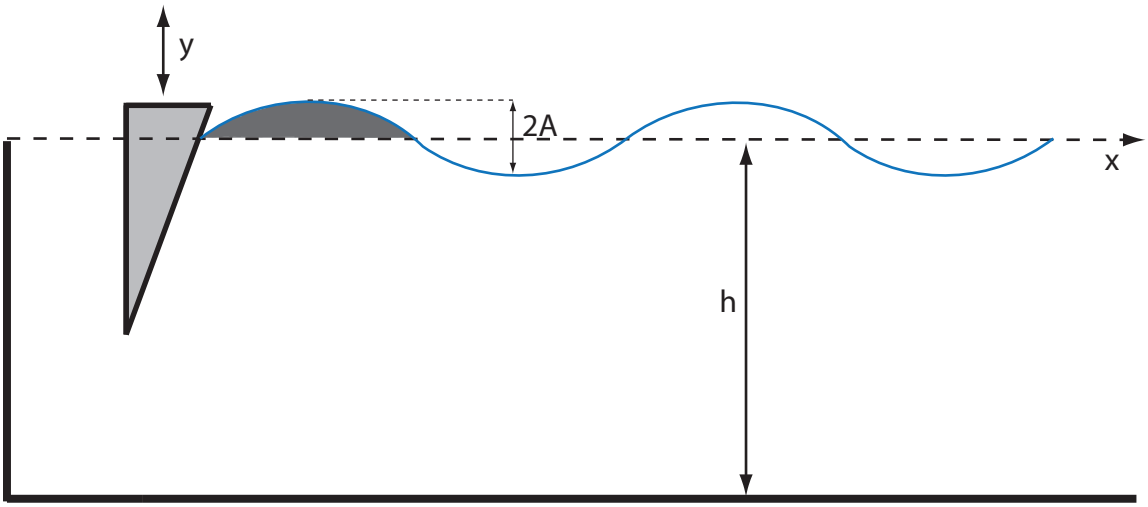

FIGURE 4.4: Diagram of a plunging wavemaker.

4.4 Modeling the Wave Tank

This section discusses how the wave tank was described mathematically, including important assumptions made in the process. The model of the finite depth wave tank is used, which is accurate for our system and reduces the complexity of the math. The analysis of the finite depth wave tank will result in the complete fluid dynamics in the tank, which is needed to describe the forces on the buoy.

4.4.1 Traveling Wave

A schematic of the experimental system is shown in Fig. 4.5. In order to determine the forces acting on the buoy, the fluid motion throughout the wave tank must be fully described. The progressive or traveling wave can be written as a sum of cosines

$$w(x,t) = \sum_{n}^{N} A_n \cos\left(n\Omega t - k_n x\right), \tag{4.6}$$

where A_n, Ω and k_n are the wave amplitude, frequency and number, respectively. For the first part of the analysis, only the first harmonic will be used. The wave

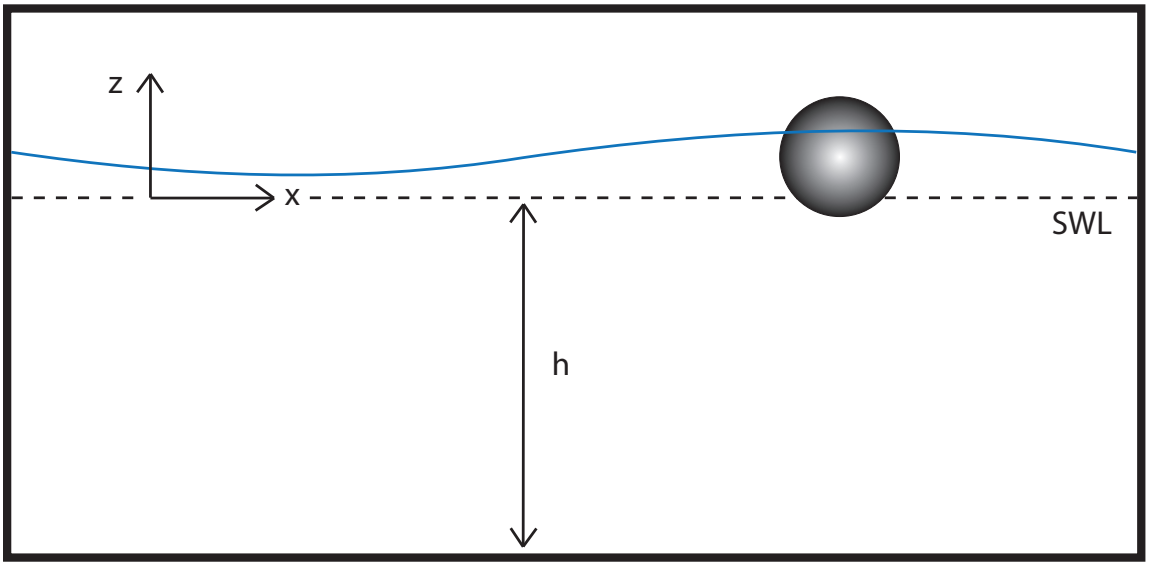

FIGURE 4.5: Diagram of a spherical buoy in a finite depth wave tank.

number k_n is found from the free surface condition [38] for the traveling wave

$$\Omega^2 - gk_n \tanh(k_n h) = 0, \tag{4.7}$$

where g is gravity. According to [38], the stream function ψ for a wave traveling in a channel with finite depth h can be written as

$$\psi(x,z,t) = -\frac{\Omega}{k}\frac{\sinh k(z+h)}{\sinh kh} w(x,t), \tag{4.8}$$

where z is measured from the SWL (still water line). With the stream function, the water velocity in both the horizontal and vertical directions can be found from

$$U = \frac{\partial \psi}{\partial z} \quad \text{and} \quad V = -\frac{\partial \psi}{\partial x}. \tag{4.9}$$

Therefore, the oscillating velocity of the water in the wave tank can be written as

$$U(x,z,t) = A\Omega \frac{\sinh k(z+h)}{\sinh kh} \sin(\Omega t - kx), \tag{4.10}$$

and

$$V(x,z,t) = A\Omega \frac{\sinh k(z+h)}{\sinh kh} \cos(\Omega t - kx), \tag{4.11}$$

where $U(x, z, t)$ is the horizontal fluid velocity and $V(x, z, t)$ is the vertical fluid velocity. Fig. 4.6 shows how $U(x, z, t)$ varies with the water depth. The fluid

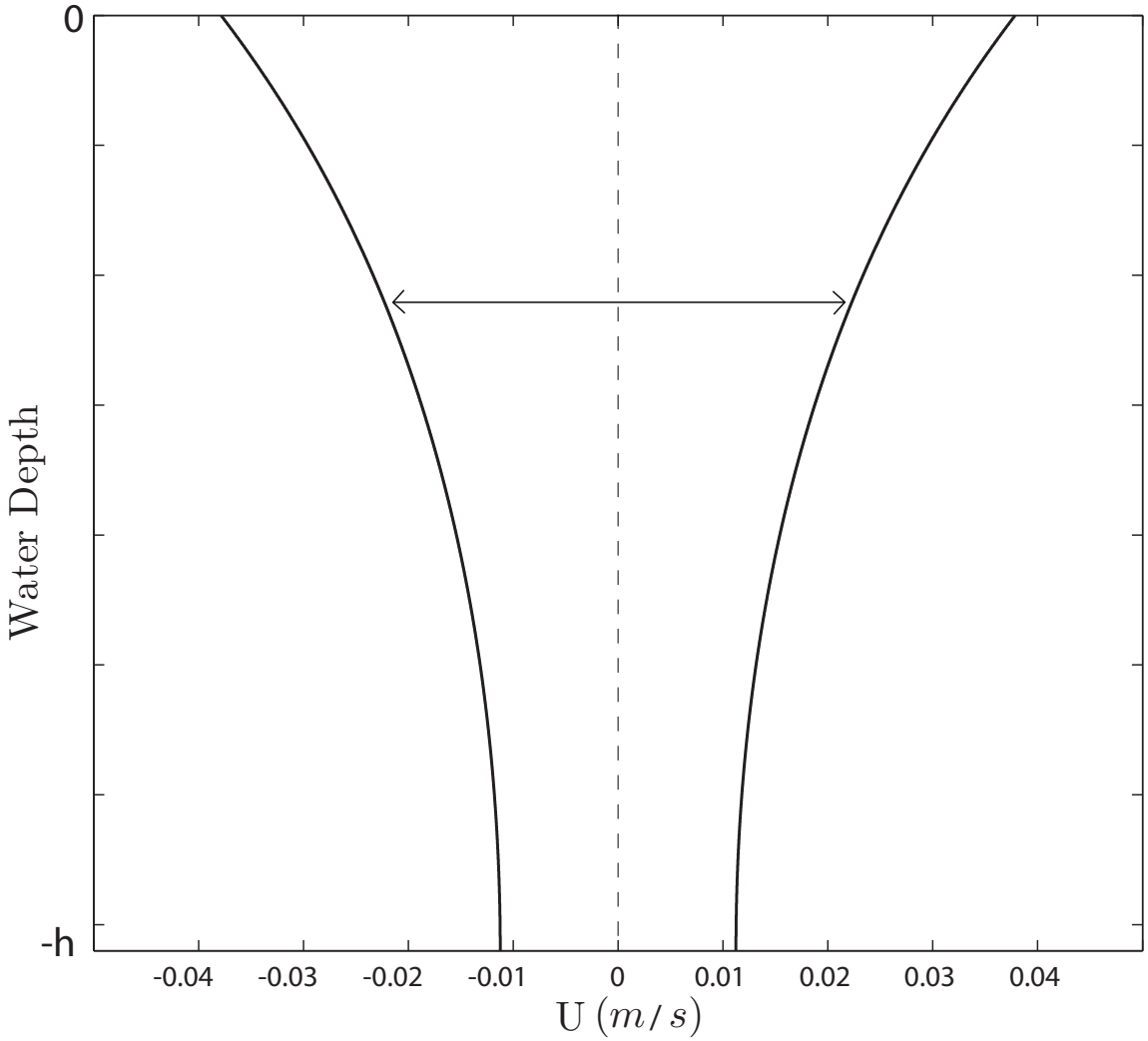

FIGURE 4.6: Oscillating horizontal fluid velocity $U(x, z, t)$ throughout finite depth wave tank using values from Table 5.1.

velocity oscillates between the two positions shown once every period. As expected, the fluid velocity is maximum at the water surface and minimum at bottom of the tank.

4.5 Wave Tank Harmonics

As opposed to a traveling wave with a single harmonic, the wave tank used for experimental measurements creates multiple harmonics. In order to accurately compare the experimental data with numerical simulation, the amplitude and phase of these harmonics must be found. The first attempt to do this involved placing a small buoy at a position (x_c) that is kept from moving in the horizontal direction by a thin piece of wire. This setup is show in Fig. 4.7. As this object floats on the surface of the water, its movement corresponds with that of the traveling wave.

Though this may give a somewhat accurate depiction of the traveling wave, even a buoy with an extremely small mass will still have inertial effects and therefore not move directly with the wave. This process was improved by utilizing something called "line-tracking," a snapshot of which is shown in Fig. 4.8. A line is drawn over the area of interest in the image processing software (in this case, the range over which the surface wave travels). The software measures the point along this line where the greatest contrast differential is located. By altering the image settings of the video, this point becomes easier to determine. In this way, the characteristics of the wave were determined directly without the use of a small buoy that can have an affect on the motion. Fig. 4.9 shows a comparison between experimental wave amplitude values and a numerical recreation using the first four harmonics.

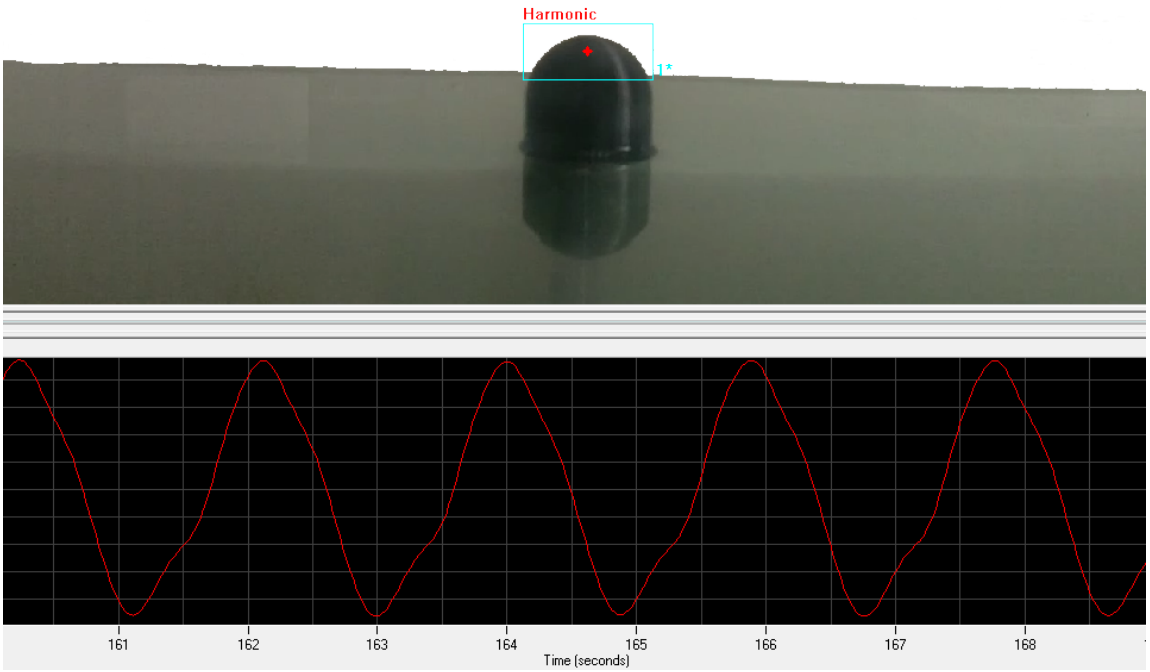

FIGURE 4.7: Snapshot of image processing software and small floating object used to determine wave harmonics.

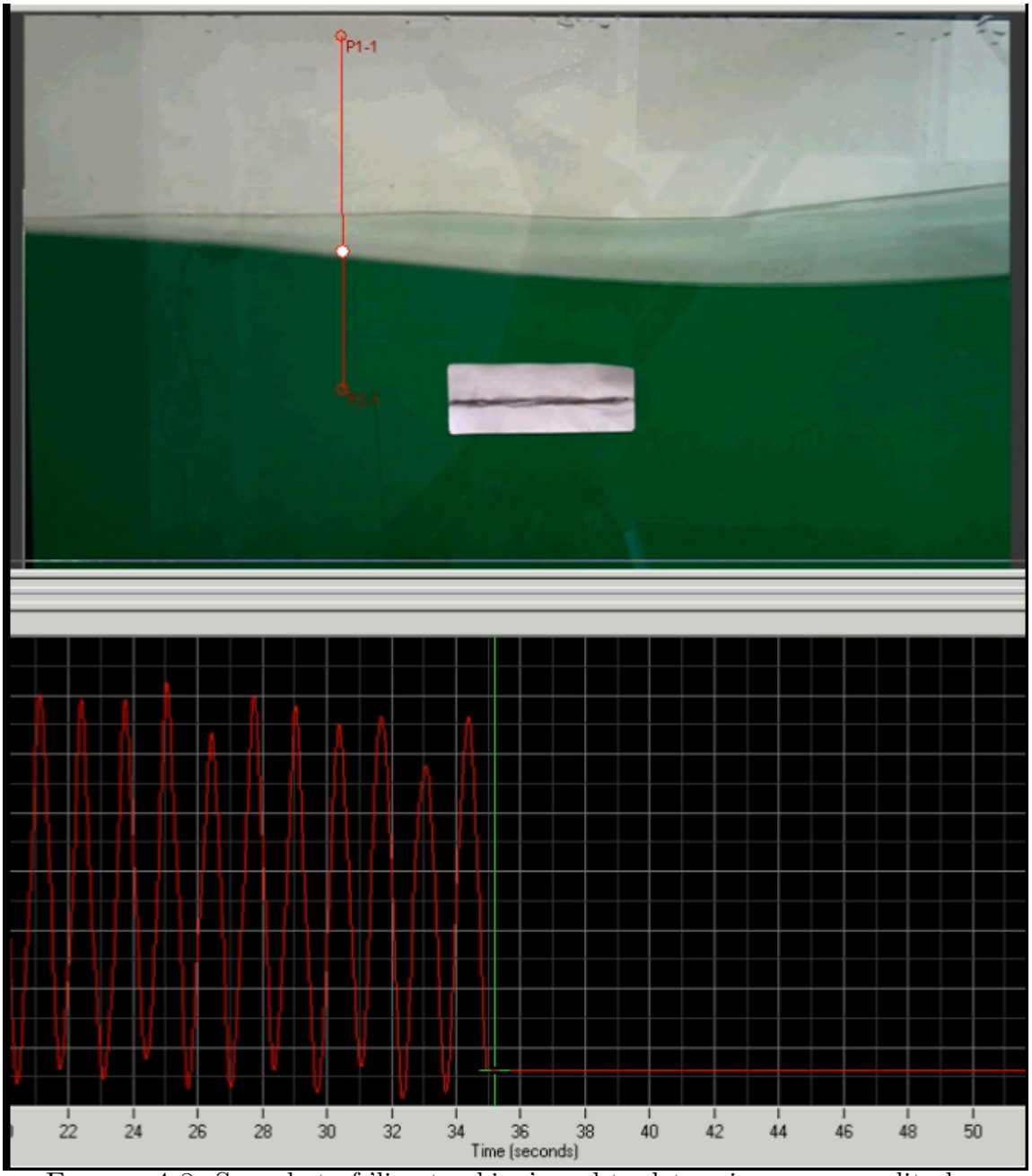

FIGURE 4.8: Snapshot of 'line tracking' used to determine wave amplitudes.

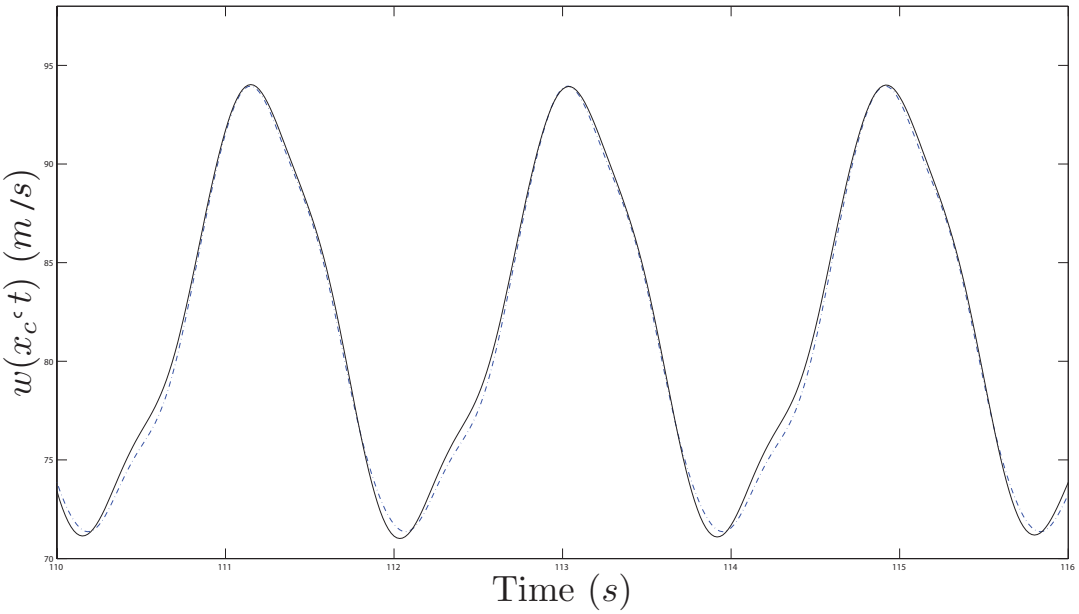

FIGURE 4.9: Wave form: experimental (dashed) vs numerical (solid).

4.6 Experimental Investigations

In order to better understand the spectrum of wave amplitudes available in the wave tank, videos of the oscillating water level were taken for a wide range of frequencies, as well as for different water depths. A couple of examples can be seen in Figs. 4.10 and 4.11. Though the water depth h only changes slightly between these two figures (from 0.43 to 0.45 m) there is a noticeable difference in the wave amplitude spectrum. Figure 4.11 shows a much more pronounced local peak at a tank setting of around 5. This can be explained using Fig. 4.12.

This figure shows how the wavelength of the traveling wave (λ) corresponds to the length of the wave tank. There is an intersection of λ and a value of one-sixteenth the tank length which occurs at a wave tank setting of 5. This value matches the peak seen in Fig. 4.11. It is a reasonable hypothesis, therefore, that in addition to the traveling wave created by the plunger, some amount of standing wave behavior is occurring at factors of the tank length. This could be due to the beach not completely dissipating every wave reflection. It should also be noted that Fig. 4.12 shows another intersection at one-eighth the tank length at a tank setting of 2.7. Though this value is too low to be seen in Fig. 4.11, it does correspond to the peak seen in Fig. 4.13 at a frequency of 3.5 Hz.

4.6.1 A Note on ProAnalyst

The image processing software utilized for experimental data collecting is performed by ProAnalyst. This program is efficient at at determining all types of two-dimensional motion, and can even be expanded to three dimensions. An example of how it can be used to find complex two-dimensional motion is shown in Fig. 4.14. This shows ProAnalyst tracking two points on a cylinder and a graph of the corresponding vertical motion. By tracking at least two points, it is also possible to determine the cylinder

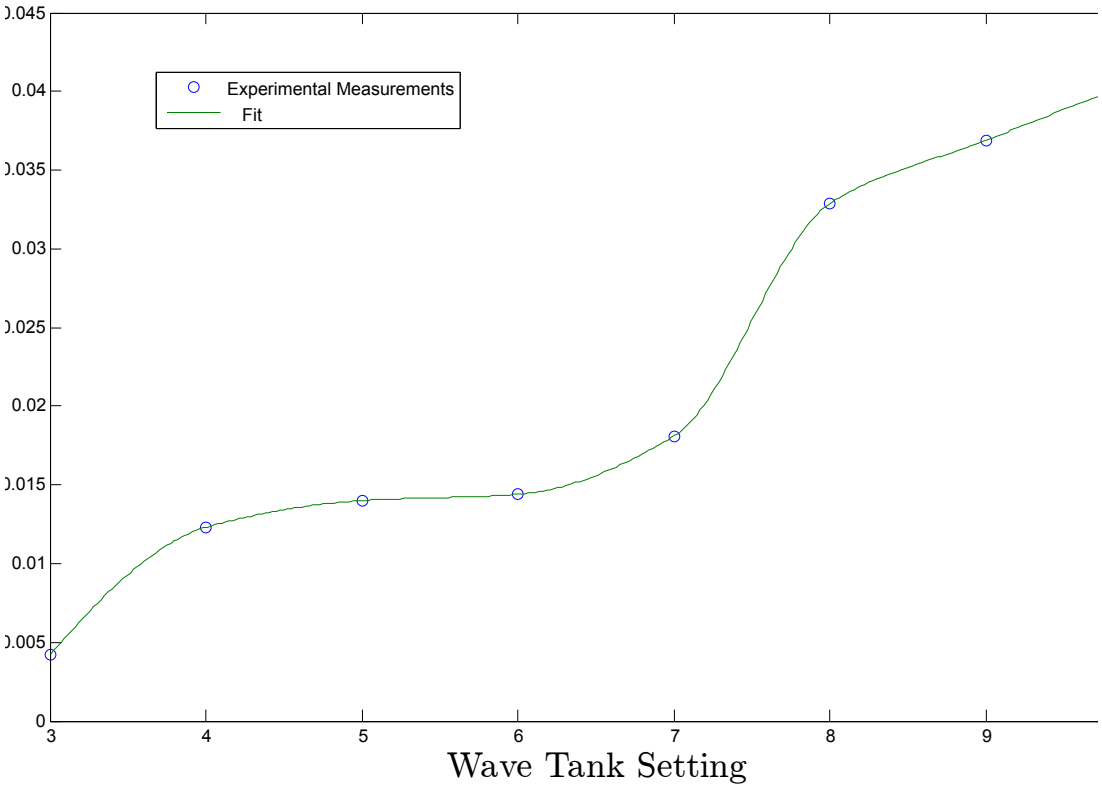

FIGURE 4.10: Experimentally determined oscillating wave amplitude for multiple frequencies, taken at a depth of 0.43 m.

tilt with respect to the horizontal or vertical axis. Velocities and accelerations of positions and tilt are also easily found.

The motivation for using ProAnalyst is the fact that it's not always feasible or desirable to use conventional methods of motion detection. For example, using a wired accelerometer to measure buoy motion in a wave tank is not an option, since it cannot become wet and any wire would likely change the buoy motion. It was originally planned to use wireless accelerometers, but with their considerable mass, they would also alter the motion of the buoy.

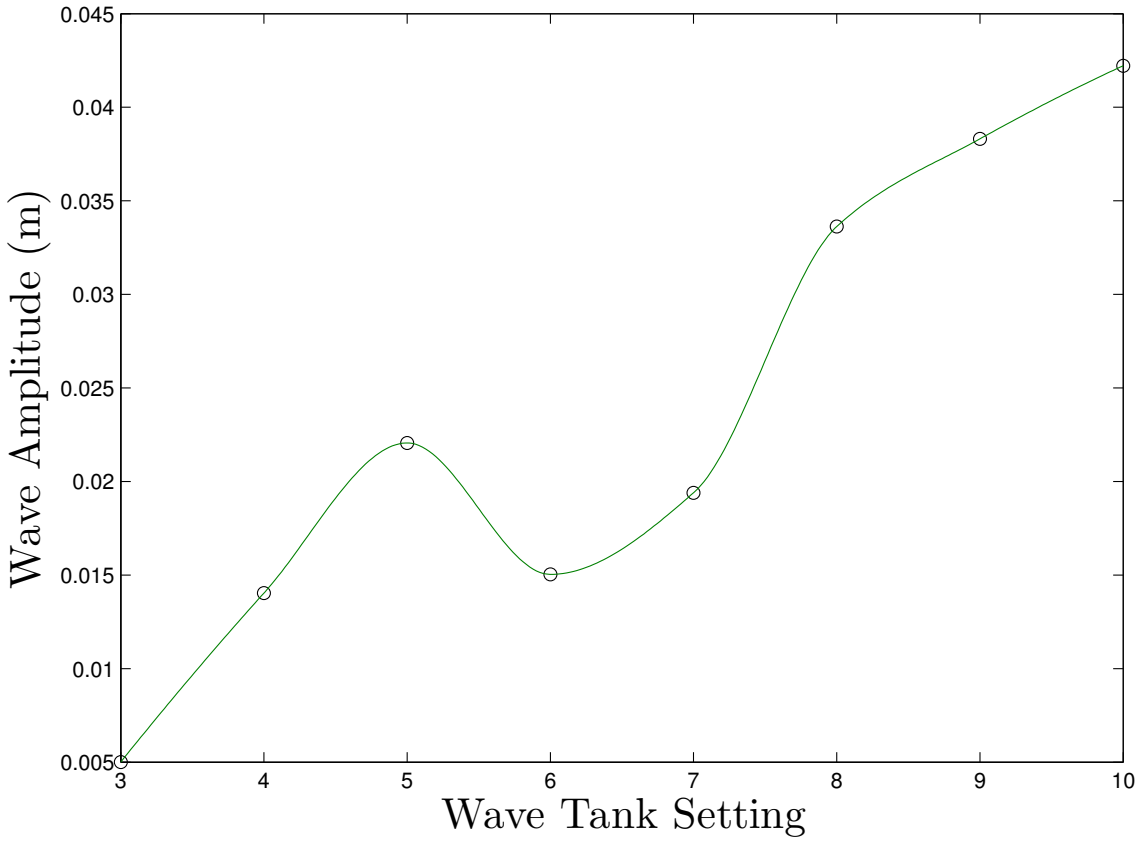

FIGURE 4.11: Experimentally determined oscillating wave amplitude for multiple frequencies, taken at a depth of 0.45 m.

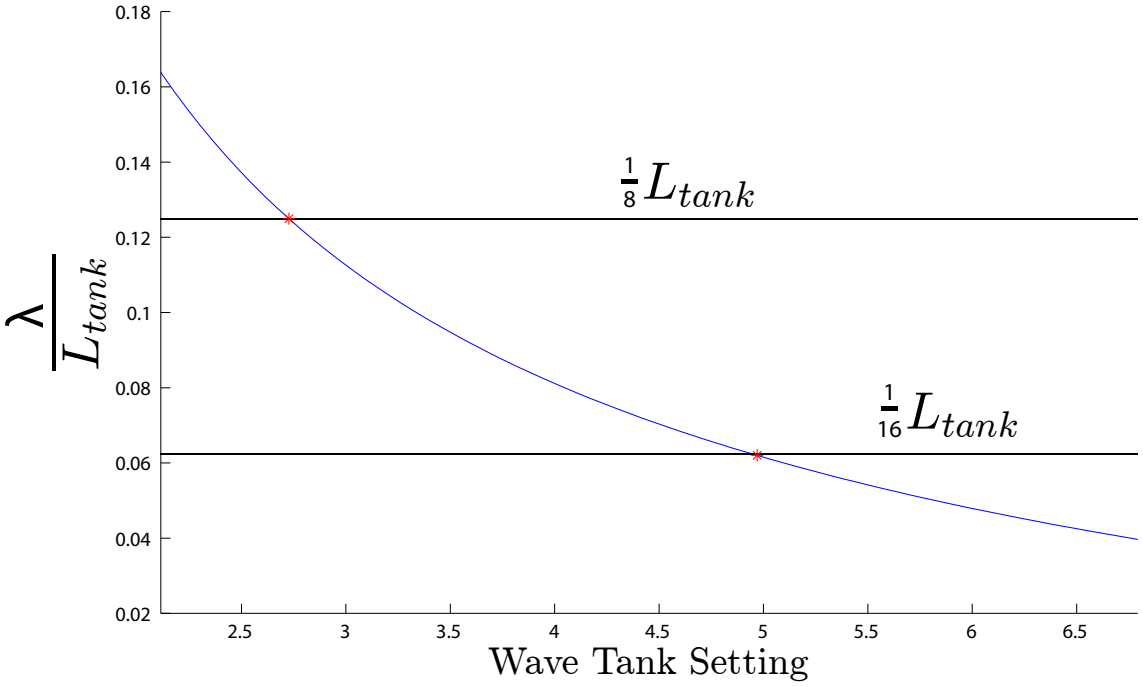

FIGURE 4.12: Correlation of wavelength of traveling wave λ to the length of the tank, shown for a depth of 0.45 m.

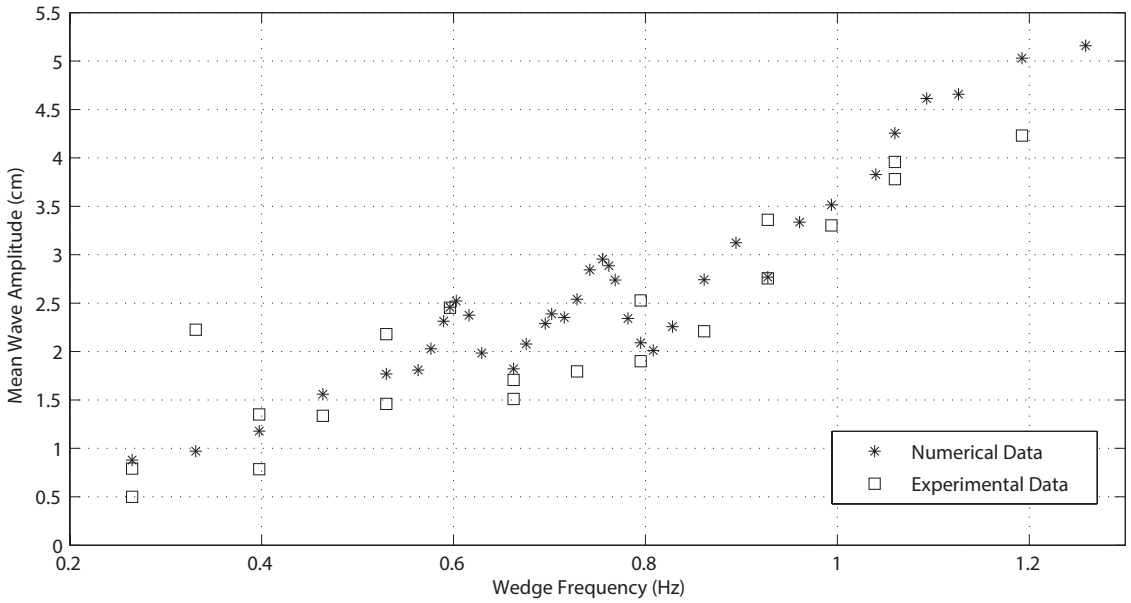

FIGURE 4.13: Courtesy of [C. Lee, J. Dolbow], comparison of experimental data to 2-D CFD analysis for a depth of 0.45 m. Peak shown at 0.6 Hz for both numerical and experimental data.

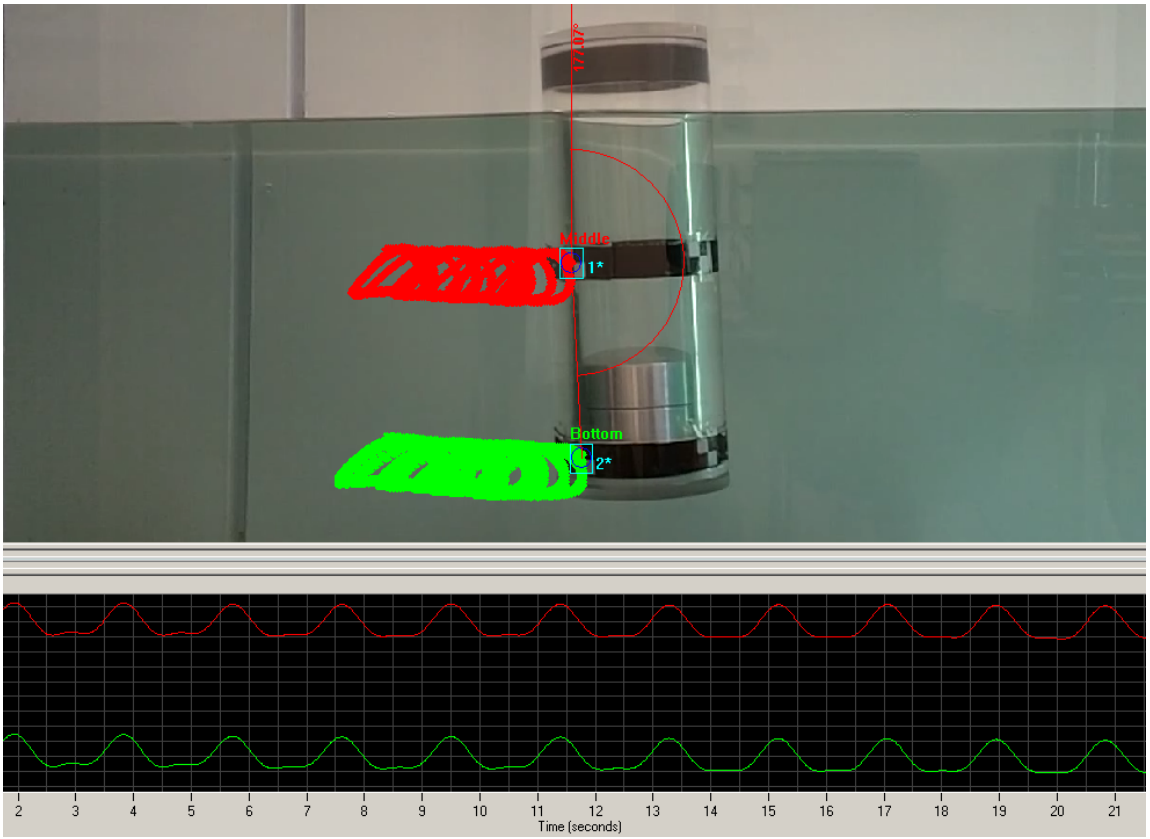

FIGURE 4.14: ProAnalyst used to track the vertical, horizontal and rotational motion of a cylinder in the wave tank.

4.7 Conclusions

Wave tanks are used to simulate ocean waves in a laboratory setting, and can serve as an input force for experimental trials of buoy motion. Analytical models for different wave tank designs were described in detail, and the fluid velocities and accelerations in these designs were derived. In order to accurately model the wave motion seen during experiments, multiple experimental runs were performed to determine wave amplitudes. This data was obtained by using the image processing software described. These amplitudes were then recreated numerically to be used as the excitation force in subsequent numerical simulations.

5

Nonlinear Dynamics of a Spherical Buoy

5.1 Introduction

An essential task in the design of ocean vessels is an understanding of their dynamic response to environmental loads – primarily consisting of loads from wind and ocean waves [70]. Some typical examples of ocean structures include oil rigs, floating platforms, moored vessels, and stand-alone buoys. Within the classification of buoys, the dynamic response of both tethered and untethered buoys are of prominent interest.

A thorough understanding of the dynamics of common geometric shapes in a wave environment is important to many highly disparate application areas [4]. For example, the external casing for ocean wave harvesters often takes the form of a cylinder or a sphere [10]; however, it is unclear which geometric shapes are most compatible or advantageous with an environment or energy harvesting strategy. Thus a clear understanding of the buoy dynamics is of fundamental importance given the fact that it serves as a precursor to a myriad of future investigations – such as studies of energy harvesters encapsulated within buoys of different geometric shapes.

Many investigations have been performed on the fluid-structure interactions of

spherical buoys [10, 36, 48]. However, for the majority of these analyses, the buoy was simply tethered [48], or tethered in order to constrain the motion, e.g. see reference [36]. Furthermore, many analyses [70] greatly simplify the parametric excitation terms that appear in the buoyancy force by linearizing the governing equations to obtain an equivalent spring constant and external forcing term; the outcome of this approach is a governing equation with the same form as the forced linear oscillator. While this approach may provide sufficient insight for certain parameter regimes, it ignores the inherent nonlinearity of the system and is insufficient to accurately describe the behavior observed for many buoy designs. In order to take full advantage of the surrounding wave environment, the nonlinearity of the buoy must be taken into account.

The present research theoretically and experimentally investigates the dynamic behavior of a spherical buoy. The derived governing equations are used to predict the motion of a spherical buoy and the assumptions applied are consistent with the features of the experimental system – a sphere floating within a wave flume. The resulting nonlinear governing equations are then used to predict the nonlinear equilibrium position and the linear natural frequency of the buoy about a submerged depth. Also, the nonlinear oscillations of the buoy, obtained via numerical simulation of the governing equations, are compared to experimental cases where synthetic-ocean waves were used to excite the buoy within the wave flume. Image processing techniques were then used to extract numerical data from videos of the buoy motions taken during the experimental trials. The inability of a simple linear model to fully capture the actual dynamic behavior of the buoy is then confirmed by experimental trials.

5.2 Morison's Equation

Morison's equation [16] has often been used to describe forces on static buoys or piles, as well as buoys moving in oscillatory flow [70]. The equation for hydrodynamic loading on a stationary object or pile in the general coordinate direction Y is

$$F_{Morison} = C_M \ddot{Y}_{fluid} \rho V_{sub} + \frac{1}{2} \rho C_D A_P \dot{Y}_{fluid} |\dot{Y}_{fluid}|, \tag{5.1}$$

where ρ is the density of the surrounding fluid, C_M and C_D are the inertial and drag coefficients, respectively, A_P is the projected area in the Y-direction and V_{sub} is the total submerged volume of the buoy. For the case of a buoy that is allowed to move freely in the oscillatory flow, however, the equation is expanded to

$$F_{Morison} = \left(C_M \ddot{Y}_{fluid} - C_A \ddot{Y}_{buoy} \right) \rho V_{sub} + \frac{1}{2} \rho C_D A_P \left(\dot{Y}_{fluid} - \dot{Y}_{buoy} \right) |\dot{Y}_{fluid} - \dot{Y}_{buoy}| \tag{5.2}$$

where C_A is the added mass coefficient, and $C_M = 1 + C_A$. C_A has a value of 0.5 for a sphere and 1 for a cylinder [44].

5.3 Problem Setup

This section provides an overview of the important dimensions and parameters of the buoy and how it interacts with the fluid in the wave tank. Using the model previously derived for the fluid dynamics, the buoy can be described in relation to the fluid.

5.3.1 Geometric Relationships

A full and accurate description of the forces acting on the buoy is required to predict the buoy's motion. To accomplish this, the location of the sphere with respect to

the waves and SWL must be known. Figure 5.1 shows a diagram of the important dimensional relationships for the buoy. In this figure, R is the radius of the sphere, L_1

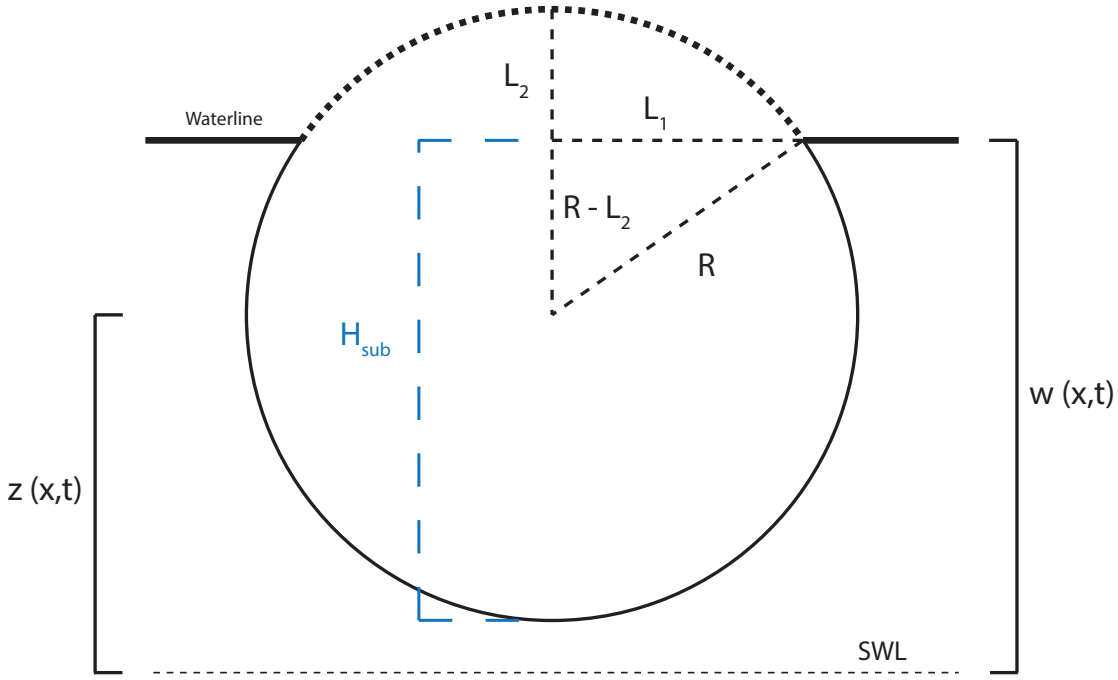

FIGURE 5.1: Dimensional relations for partially submerged buoy due to wave loading.

is the radius of the cap created by the wave line, L_2 is its height, and w (or $w(x,t)$) is the height of the wave with respect to the SWL. Here, an important and simplifying assumption has been made. In this figure, as well as in the analyses that follow, the wave height across the buoy was assumed to be constant, which decreases the model complexity and is consistent with models of point absorbers. This assumption is reasonable for many buoy designs, especially for a wave tank with large wavelengths such as the one used in the experimental section. L_1 and L_2 are now written in terms of the known parameters of the system. The two relationships are

$$(R - L_2)^2 + L_1^2 = R^2 \quad \text{and} \quad L_2 = R - |z - w|, \tag{5.3}$$

where the absolute value in the L_2 term accounts for z being either above or below the wave line. Now that the relations are known, the formula for the volume of a dome can be used to define the submerged volume of the sphere, V_{sub}. This term is written as

$$V_{sub} = \frac{\pi}{3}\left[(2R + z - w)\,(R - z + w)^2\right]. \tag{5.4}$$

5.3.2 Vertical Equation of Motion

Using Morison's equation in the vertical direction, the force on the buoy due to fluid motion can be written as

$$F_z(x, z, t) = \left(\rho C_M \dot{V} - \rho C_A \ddot{z}\right) V_{sub} + \frac{1}{2}\rho C_D A_z\,(V - \dot{z})\,|V - \dot{z}| + F_B - m_b g, \tag{5.5}$$

where m_b is the buoy mass, V or $V(x, z, t)$ is the fluid velocity in the vertical direction, and A_z is the projected area in the vertical direction, defined as

$$A_z = \begin{cases} \pi L_1^2 & \text{for} \quad -R < w - z < 0 \\ \pi R^2 & \text{for} \quad 0 < w - z < R \end{cases} \tag{5.6}$$

The last two terms in Eqn. 5.5 account for the static forces from buoyancy (F_B) and gravity, where

$$F_B = \rho g V_{sub}. \tag{5.7}$$

Using this equation for the force on the buoy, the equation of motion in the vertical direction becomes

$$(m_b + m_f)\ddot{z} + m_b g = \rho V_{sub}\left(g + C_M \dot{V}\right) + \frac{1}{2}\rho C_D A_z\,(V - \dot{z})\,|V - \dot{z}| \tag{5.8}$$

where m_f is the hydrodynamic mass, defined as

$$m_f = \rho C_A V_{sub}. \tag{5.9}$$

5.3.3 Horizontal Equation of Motion

Using Morison's Equation again, the force on the buoy in the horizontal direction can be written as

$$F_x(x,z,t) = \left(C_M\dot{U} - C_A\ddot{x}\right)\rho V_{sub} + \frac{1}{2}\rho C_D A_x(U-\dot{x})|U-\dot{x}|, \tag{5.10}$$

where U or $U(x,z,t)$ is the fluid velocity in the horizontal direction. The projected area in the x-direction A_x is estimated as

$$A_x = \frac{\pi R}{2}H_{sub}, \tag{5.11}$$

where H_{sub} is the submerged height, written as

$$H_{sub} = R + w - z. \tag{5.12}$$

Although this is a linearization of the the actual projected area, it does not cause noticeable changes in the results. Also, since the important nonlinearity exists in the formula for V_{sub}, this is an acceptable estimation. As before, the equation of motion in the horizontal direction becomes

$$(m_b + m_f)\,\ddot{x} - \frac{1}{2}\rho C_D A_x\,(U-\dot{x})\,|U-\dot{x}| = \rho V_{sub} C_M \dot{U}. \tag{5.13}$$

5.4 Static Analysis

This system is first observed statically in order to understand the qualitative effects of varying system parameters. Figure 5.2 shows how the buoyancy force changes with depth. This graph shows that the buoyancy force reaches its minimum and maximum at $+R$ and $-R$, respectively. At these points, the buoy is either out of the water ($+R$) or completely submerged ($-R$). This graph shows that if the buoyancy force is linearized about the center as is often done, the curvature at the ends is

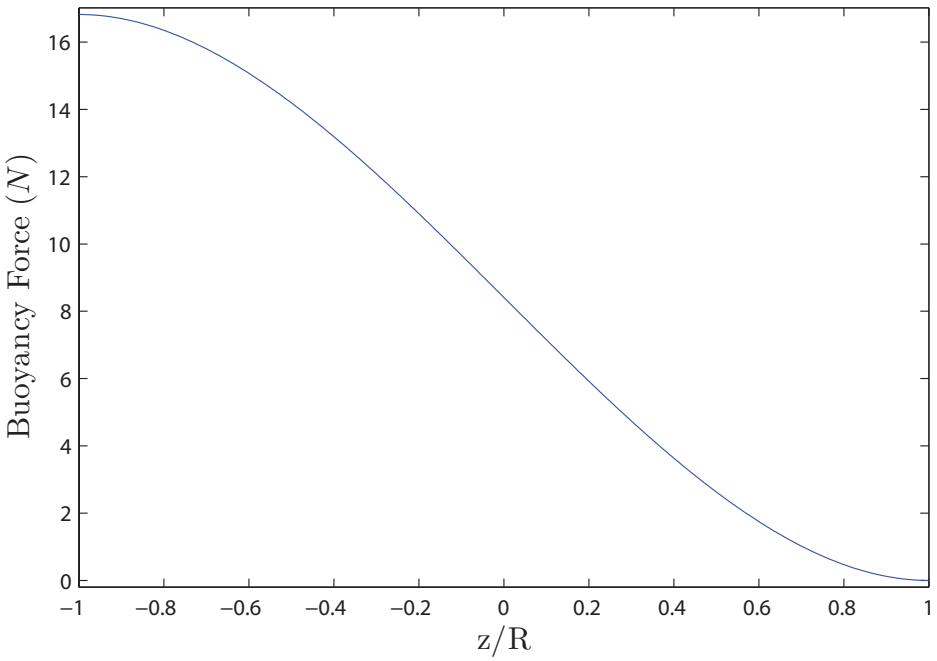

FIGURE 5.2: Buoyancy force vs dimensionless depth.

not accounted for. For a buoy that exhibits small oscillations and whose equilibrium position is zero, this formulation can be accurate. For any other setup, however, the linear model may not be sufficient.

The projected area is held constant for submerged objects, but in the case where the buoy is only partially submerged, A_P is the projected area defined in Eqn. 5.6. The area increases until the buoy becomes halfway submerged and is held constant from then on. Fig. 5.3 shows how it varies with vertical displacement.

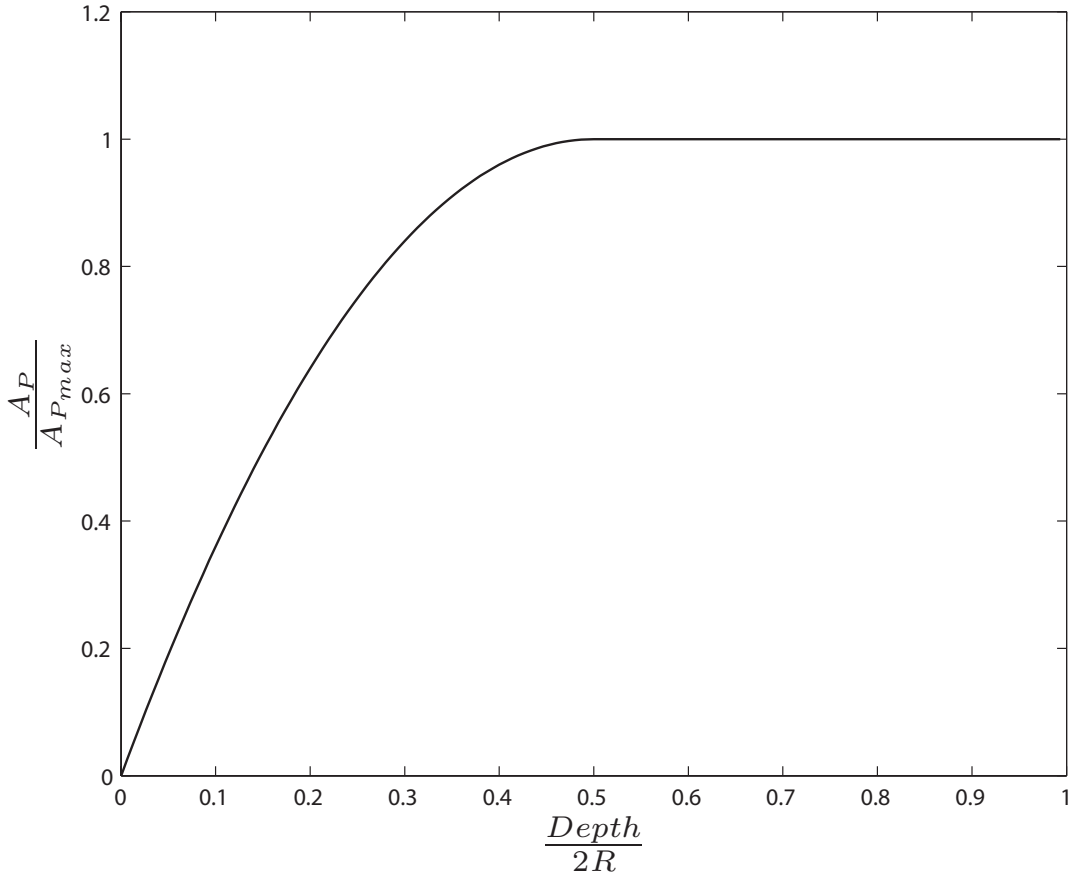

FIGURE 5.3: Projected area in the z-direction vs dimensionless depth.

5.5 Numerical Investigations of Dynamic Behavior

Using the equations of motion derived previously, the dynamic behavior of the system can be observed with numerical simulation. Studied first is a wave with a single harmonic. The time series response is shown in Fig. 5.4.

This figure shows the single harmonic sinusoidal response of the buoy in two directions. For the horizontal motion, however, the buoy also has a linear component due to the buoy continuously moving in the positive x-direction. Figure 5.5 helps to visualize this motion. Taken from the animation of the 2D numerical simulation for the buoy, this figure shows the buoy with large oscillation amplitudes in the vertical

direction, and much smaller oscillations in the horizontal direction. As it travels in the horizontal direction, minimum and maximum nodes can be seen, i.e. where the vertical oscillation is smallest and largest, respectively. These nodes occur at multiples of the wavelength of the forcing fluid λ, written as

$$\lambda = \frac{2\pi}{k}, \tag{5.14}$$

which are marked in the figure with dots in the vertical direction.

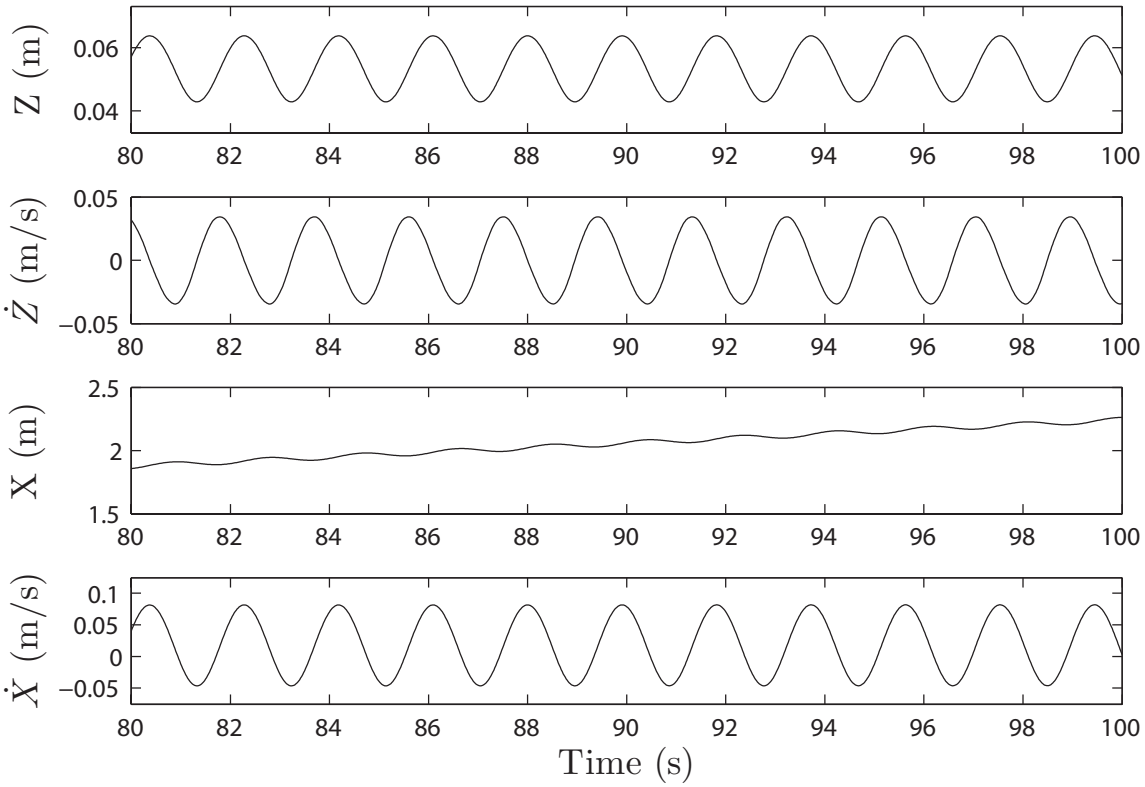

FIGURE 5.4: Time series for both horizontal and vertical positions and velocities with $m_b = 0.1$.

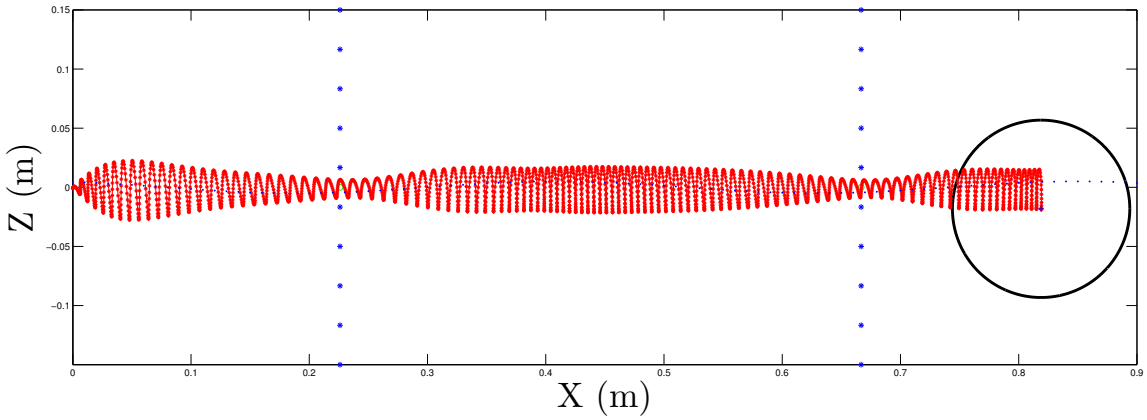

FIGURE 5.5: Animation snapshot of 2D numerical solution for the spherical buoy, with a forcing frequency of 1.05 times the natural frequency ($m_b = 0.9$ kg). It can be seen that the buoy experiences a minimum vertical oscillation amplitude at multiples of the wavelength of the forcing fluid.

It is interesting to observe how this motion and other buoy responses can be altered by changing its parameters. Figure 5.6 shows how the buoy oscillation amplitudes in both the z and x direction change with buoy mass. This figure shows that both the vertical motion and velocity increases with increased buoy mass, though the horizontal motion decreases. One would expect the motion in general to decrease with buoy mass due to the increased inertia of the buoy, which is true for the horizontal direction. In the vertical direction, however, the increased buoy mass increases the buoyancy force, which results in a larger response.

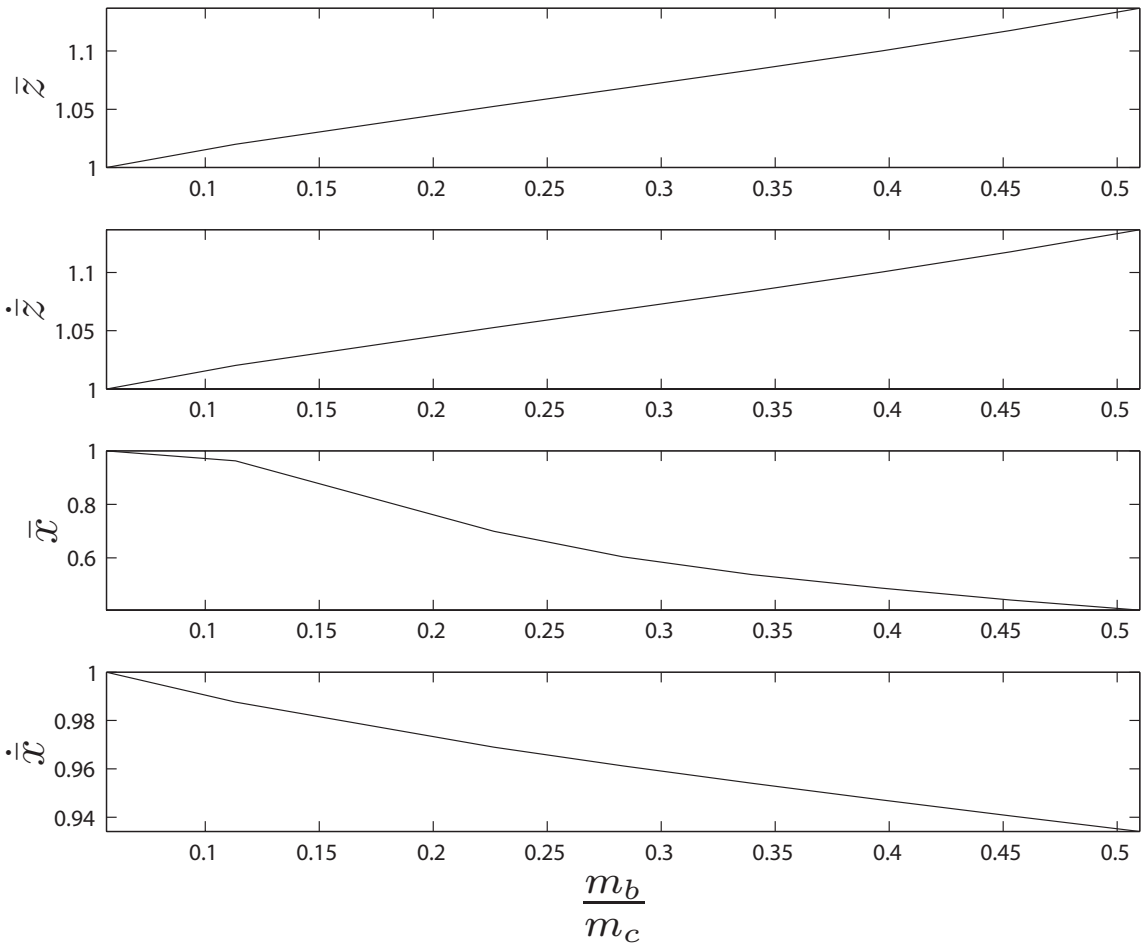

FIGURE 5.6: Amplitude ratios vs buoy mass ratio, where $\bar{x} = x$-motion amplitude normalized by first mass.

Observed next is the frequency content of the buoy response. For this particular set of tests, the single harmonic wave is changed to one with four harmonics and phase shifts. This type of wave more accurately resembles the waves created by the wave tank used in the experimental section. The process by which the wave amplitude and phase shifts are derived is described in greater detail in the next section.

For the first test, the buoy with $m_b = 0.1\ kg$ whose response was shown in Figure 5.4 is observed. The system parameters for this test and all those that follow are shown in Table 5.1. As seen in Fig. 5.7, this initial set of parameters results mainly in a first order harmonic response.

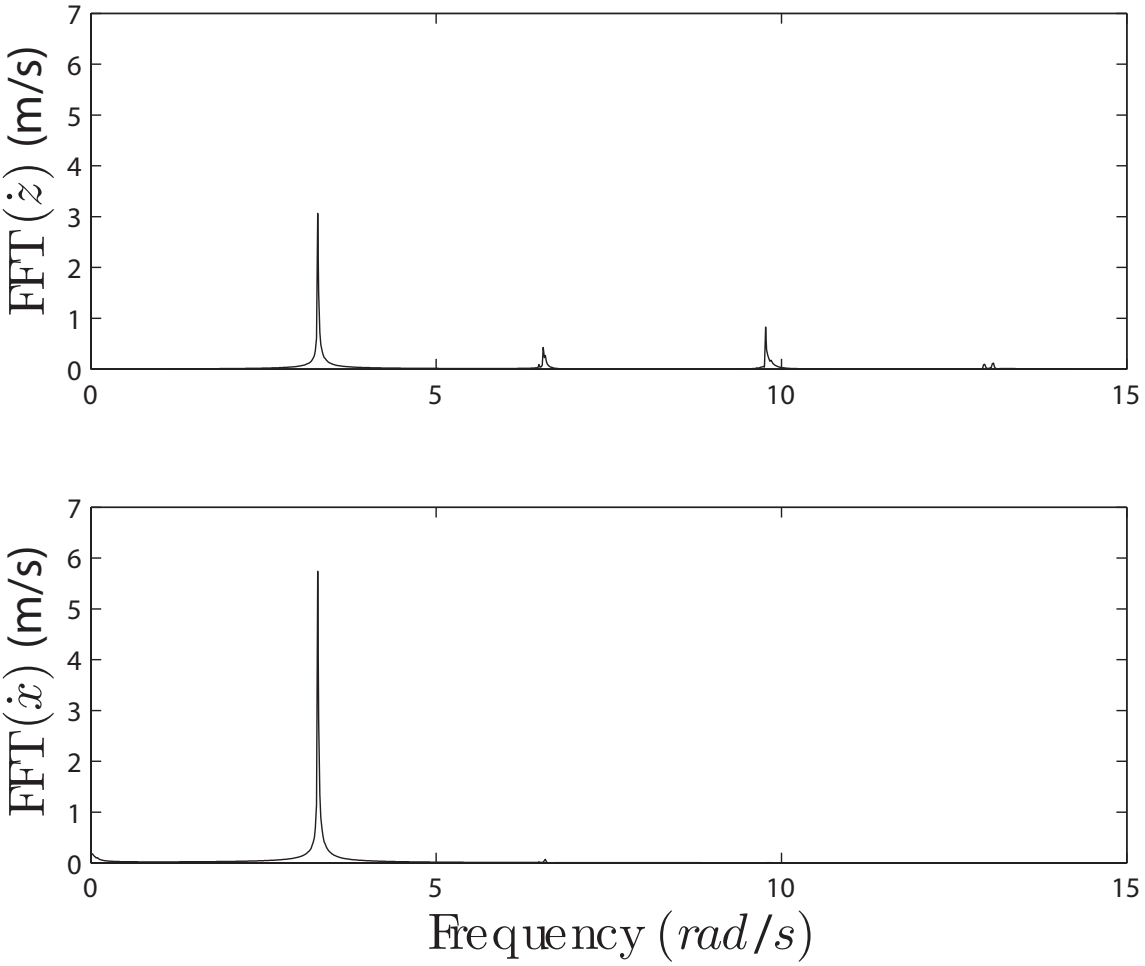

FIGURE 5.7: Velocity frequency spectrum for $m_b = 0.1\ kg$ (numerical).

If the buoy mass is changed to $\approx 0.62\ kg$, the fourth harmonic of the wave will match the natural frequency of the buoy found from Eqn. 5.50. The resulting response is shown in Fig. 5.8. As expected, the response becomes large at the fourth wave harmonic, even though the wave amplitude at this frequency is more than thirty times smaller than that of the main frequency.

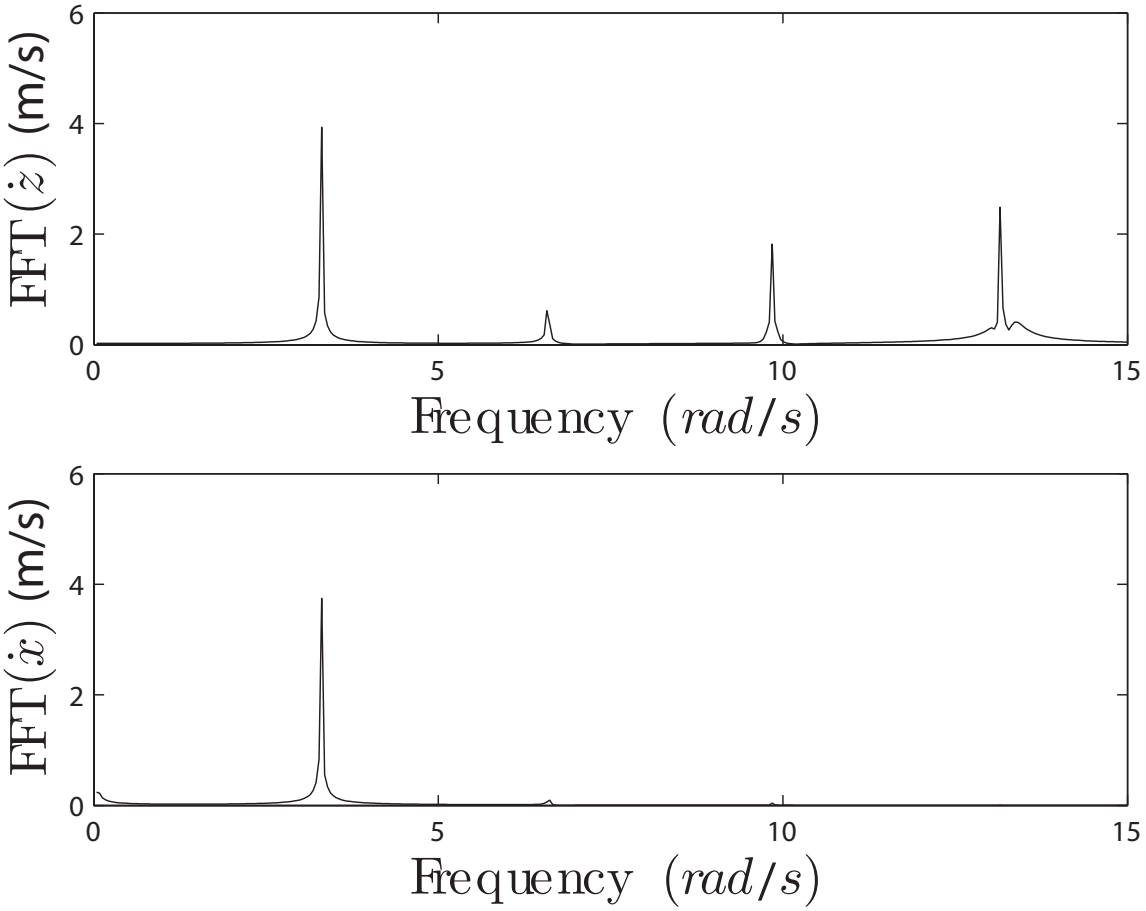

FIGURE 5.8: Velocity frequency spectrum for $m_b = 0.62\ kg$ (numerical).

Table 5.1: System parameters

Parameter	Symbol	Value	Units
Sphere Mass	m_b	0.1, 0.5, 0.62, 0.9	kg
Sphere Radius	R	7.5	cm
Fluid Density	ρ	998	kg/m^3
Drag Coefficient	C_D	0.3	$-$
Wave Amplitude	A_1	11	cm
Wave Frequency	ω	1.06π	rad/s

5.6 Analytical Model

This section describes the derivation of an analytical model for the spherical buoy. Many assumptions are made in order to decrease the complexity of the math, but all of these assumptions are shown to be reasonable for our specific setup. First, an analytical solution is found for vertical motion, followed by the derivation of a a coupled two-dimensional model.

5.6.1 1-D Vertical Solution

The most important term in the vertical equation of motion (Eqn. 5.8) is the submerged volume V_{sub}, which is a function of both the wave and the buoy position. After expanding, this volume can be written as

$$V_{sub} = \frac{\pi}{3}\left(2R^3 + 3R^2w - 3R^2z - w^3 + 3w^2z - 3wz^2 + z^3\right) \tag{5.15}$$

The projected area A_P can be approximated as a series of Legendre polynomials using Rodrigues' formula. This approximation takes the form of

$$A_P \approx \sum_{n=0}^{N} c_n P_n(y) \tag{5.16}$$

where $P_n(y)$ is the n^{th} Legendre polynomial and c_n is its corresponding constant. Rodrigues's formula is written as

$$P_n(y) = \frac{1}{2^n n!}\frac{d^n}{dy^n}[(y^2-1)^n] \tag{5.17}$$

Since it provides sufficient accuracy, a third order approximation ($N = 3$) is used. Solving this equation results in the following first four polynomials

$$P_0 = 1, \quad P_1 = y, \quad P_2 = \frac{1}{2}(3y^2-1), \quad P_3 = \frac{3}{2}(5y^3 - 3y) \tag{5.18}$$

It is important to notice that this process is only valid over the interval $[-1, 1]$, so an appropriate y must be found. The range of interest is from the buoy being completely out of the water to completely submerged. Therefore, if y is defined to be $(w-z)/R$, the correct range of -1 (buoy just above water line) to 1 (just below) is obtained. Utilizing the orthogonality properties of Legendre polynomials, the constants (c_n) can be written as

$$c_n = \frac{\int_{-1}^{1} A_P(y) P_n(y) y}{\int_{-1}^{1} P_n^2(y) dy} \tag{5.19}$$

The projected area, however, is a discrete function. It is defined as

$$A_P(y) = \begin{cases} \pi(R^2 - y^2) & -R \leq y < 0 \\ \pi R^2 & 0 < y \leq R \end{cases} \tag{5.20}$$

After splitting up the integral, the constants are found to be

$$c_0 = \frac{5}{6}\pi R^2, \quad c_1 = \frac{3}{8}\pi R^2, \quad c_2 = -\frac{1}{3}\pi R^2, \quad c_3 = \frac{7}{144}\pi R^2 \tag{5.21}$$

The Legendre approximation and the actual A_P can now be compared. Figure 5.9 shows the ratios of A_P and its approximation to the maximum projected area as it varies with a submerged depth ratio. This ratio is zero when the buoy is out of the water and one when it is fully submerged. The fluid acceleration $(\dot{V})$ contains the vertical motion $z(t)$ inside of a hyperbolic sine, and therefore must be estimated. By expanding $\dot{V}$ about $z(t)$ equals zero, this estimation is written as

$$\begin{aligned} \dot{V} \approx \frac{A\Omega^2 \cos(\Omega t)\, \mathrm{e}^{-kh}}{12 \sinh(kh)} [6(\mathrm{e}^{2kh} - 1) + 6k(1 + \mathrm{e}^{2kh}) z(t) ... \\ + 3k^2(\mathrm{e}^{2kh} - 1) z(t)^2 + k^3(1 + \mathrm{e}^{2kh}) z(t)^3] \end{aligned} \tag{5.22}$$

The motion of the buoy $(z(t))$ is assumed to take the form of

$$z(t) = A_1 \sin(\Omega t) + B_1 \cos(\Omega t) \tag{5.23}$$

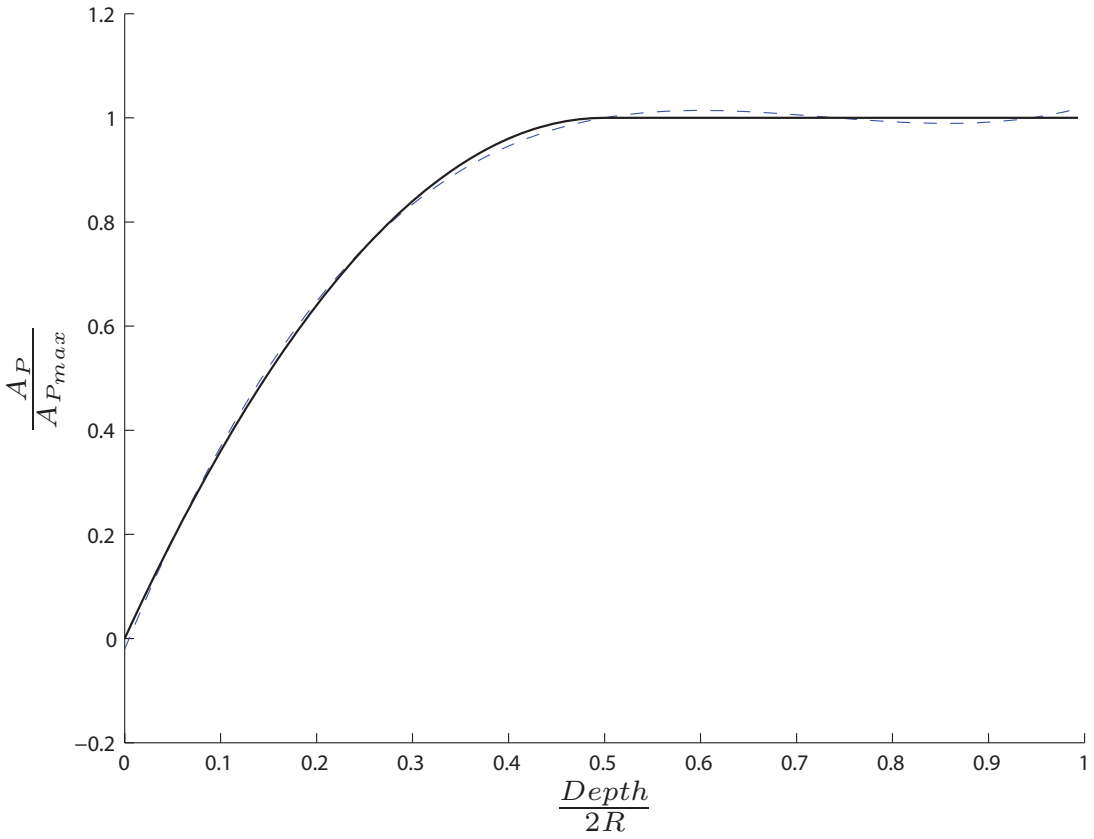

FIGURE 5.9: Projected area ratio vs submerged depth ratio: actual (solid) and Legendre approximation (dashed).

or, for algebraic simplification,

$$z(t) = \tilde{z} + r\cos(\Omega t + \phi) \tag{5.24}$$

where $r = \sqrt{A_1^2 + B_1^2}$ and ϕ is the phase shift. $\tilde{z}$ is included in the solution since the buoy will not always oscillate about zero. Not including this term causes a well known error when using harmonic balance for a system with a quadratic nonlinearity. For example, a quadratic nonlinearity for the simpler solution can be expanded, such as

$$(r\cos(\Omega t + \phi))^2 = \frac{1}{2}r^2(\cos 2(\Omega t + \phi) + 1) \tag{5.25}$$

This expansion only has a constant and a cosine of the second harmonic. Therefore,

it is completely left out of the first order solution. However, if the assumed solution form is changed to include $\tilde{z}$, this same nonlinearity becomes

$$(\tilde{z} + r\cos(\Omega t + \phi))^2 = \frac{1}{2}r^2\left(\cos 2(\Omega t + \phi) + 1 + 4\tilde{z}\cos(\Omega t + \phi) + 2\tilde{z}^2\right) \tag{5.26}$$

which, in addition to having the second harmonic as before, also contains a first harmonic term. This allows for the quadratic nonlinearity to be accounted for in the first order solution. Using this assumed form, the damping term can be written as a Fourier series. For the first harmonic, this will take the form

$$\text{Damping Term} = \frac{1}{2}\rho A_P C_D(a_n \cos\Omega t + b_n \sin\Omega t) \tag{5.27}$$

where a_n and b_n are defined as

$$a_n = \frac{1}{\pi}\int_0^{2\pi} \dot{z}|\dot{z}|\cos n(\theta - \phi)\mathrm{d}\theta \tag{5.28}$$

and

$$b_n = \frac{1}{\pi}\int_0^{2\pi} \dot{z}|\dot{z}|\sin n(\theta - \phi)\mathrm{d}\theta \tag{5.29}$$

where the variable θ is

$$\theta = \Omega t + \phi \tag{5.30}$$

Note that only the buoy velocity ($\dot{z}$) is used in the drag, as opposed to the relative velocity ($V - \dot{z}$) used in Morison's equation. This is done in order to simplify the equation. The assumption only causes a noticeable change near the natural frequency of a buoy subjected to large amplitude wave motion. This is because the relative velocity between the wave and buoy becomes more important as the oscillations become larger. Figure 5.11 shows that even though there is a small difference near the natural frequency, it is still only a seven percent difference at its highest.

To get rid of the absolute value, these integrals can be split up and solved, resulting in

$$a_n = \frac{1}{\pi}\int_0^{\pi} -\dot{z}^2 \cos n(\theta-\phi)\mathrm{d}\theta + \frac{1}{\pi}\int_{\pi}^{2\pi} \dot{z}^2 \cos n(\theta-\phi)\mathrm{d}\theta \tag{5.31}$$

and

$$b_n = \frac{1}{\pi}\int_0^{\pi} -\dot{z}^2 \sin n(\theta-\phi)\mathrm{d}\theta + \frac{1}{\pi}\int_{\pi}^{2\pi} \dot{z}^2 \sin n(\theta-\phi)\mathrm{d}\theta \tag{5.32}$$

Utilizing trigonometric identities, a_n and b_n become

$$a_n = -\frac{8r^2\Omega^2 \sin n(\pi-\phi)}{n^3\pi - 4n\pi} \sin\left(\frac{n\pi}{2}\right) \tag{5.33}$$

and

$$b_n = \frac{8r^2\Omega^2 \cos n(\pi-\phi)}{n^3\pi - 4n\pi} \sin\left(\frac{n\pi}{2}\right) \tag{5.34}$$

Knowing that n is always an integer results in the final forms of a_n and b_n

$$a_n = \frac{-8r^2\Omega^2}{\pi n(n^2-4)} \sin(n\phi) \tag{5.35}$$

and

$$b_n = \frac{-8r^2\Omega^2}{n\pi(n^2-4)} \cos(n\phi) \tag{5.36}$$

Now that the equation of motion is written entirely in the from of sin and cos to varying powers, the method of Harmonic Balance can be applied to find an analytical solution. For Harmonic Balance to work, the equation must be divided into terms that multiply $\sin\Omega t$, $\cos\Omega t$, $\sin\phi$ and $\cos\phi$. However, since the equation being studied has many higher order terms, a complex series approach is helpful in simplifying the math. Using this approach, the equation is grouped into terms that multiply $\sin\phi$ and $\cos\phi$ as before, but also real and imaginary terms. Note that for

this analysis, only the first order vertical oscillations are studied. This results in the following equations

$$\Re : \quad [J_1] \sin\phi + [J_2] \cos\phi = \Gamma \tag{5.37}$$

$$\Im : \quad [J_3] \sin\phi - [J_4] \cos\phi = 0 \tag{5.38}$$

where

$$J_2 = J_3 = (C_5)r^5 + (C_3)r^3 + (C_1)r, \tag{5.39}$$

$$J_1 = J_4 = (S_4)r^4 + (S_2)r^2, \tag{5.40}$$

and

$$\Gamma = (G_6)r^6 + (G_4)r^4 + (G_2)r^2 + G_0, \tag{5.41}$$

and the C, S and G variables are long functions of A and Ω. By squaring these equations, the ϕ terms disappear and the equation simplifies to

$$J_1^2 + J_2^2 = \Gamma^2 \tag{5.42}$$

which is a polynomial function in r. By finding the roots of this equation, the response amplitude due to a varying input frequency can be predicted. In order to get an accurate comparison of the analytical solution to numerical data, the damped natural frequency ω_d must be known. This can be written as

$$\omega_d = \omega_n \sqrt{1 - \zeta^2} \tag{5.43}$$

where ω_n is the natural frequency obtained analytically in Eqn. 5.50 and ζ is calculated using the data from the previous test where the natural frequency was found experimentally. By comparing the amplitude of oscillation for each period, the log decrement can be written as

$$\delta = \frac{1}{n} \ln \frac{z_0}{z_n} \tag{5.44}$$

where n is the number of periods and z_n is the amplitude n periods away from the initial displacement z_0. After calculating the log decrement, the damping ratio (found to be 0.1 for the buoy) is

$$\zeta = \frac{1}{\sqrt{1 + (\frac{2\pi}{\delta})^2}} \tag{5.45}$$

As shown in Fig. 5.10, the frequency response contains a dip just before the natural frequency. The comparison between the analytical solution and numerical simulation can be seen in Fig. 5.11.

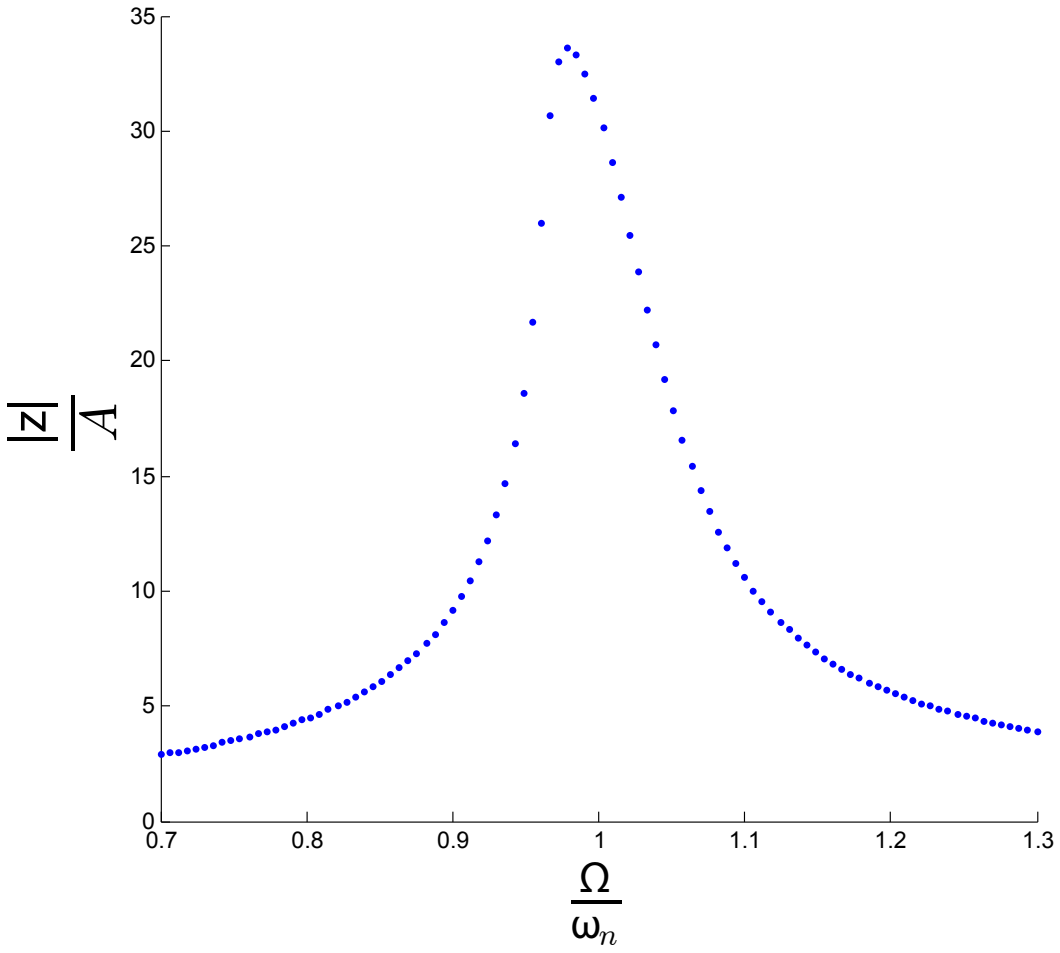

FIGURE 5.10: Response amplitude ratio vs input forcing frequency ratio for $m_b = 0.75\ kg$: analytical (blue dots).

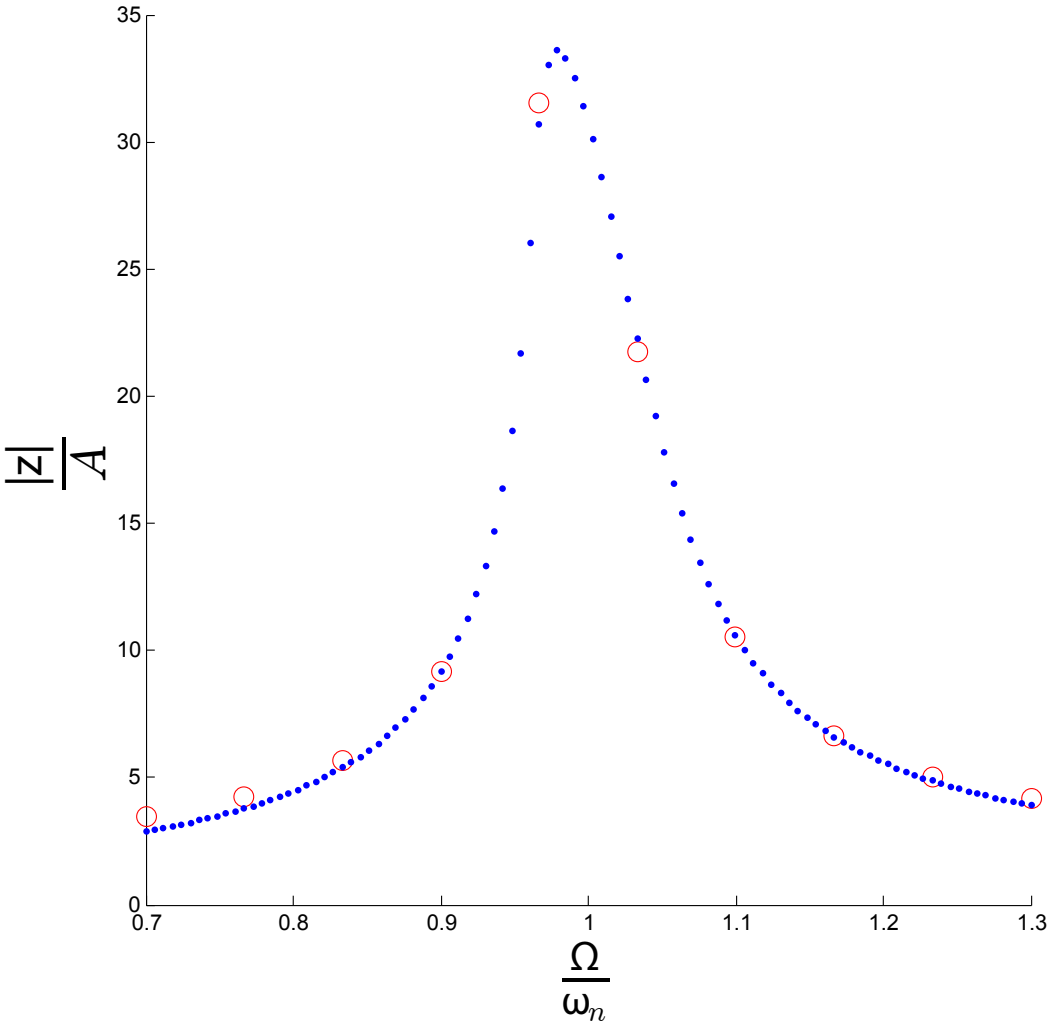

FIGURE 5.11: Response amplitude ratio vs input forcing frequency ratio for $m_b = 0.5\ kg$: analytical (blue dots) and numerical simulation (red circles).

5.7 Numerical Continuation and Simulation

To confirm the results already obtained, collocation can used for the spherical buoy. As mentioned in the first chapter, numerical continuation is a method where equilibrium values can easily be found. Collocation is simply an extension of this principle, solving for equilibrium values of harmonic responses. Instead of finding only one particular value, collocation finds a periodic orbit in the system, which gives the amplitude of the response. By performing this method for multiple forcing frequencies, a comparable frequency response graph can be created. The resulting data is shown in Fig. 5.12. Now, this result can be compared to the previous numerical and analytical results, which can be seen in Fig. 5.13.

These figures show the high accuracy of the methods when compared with each other. It is therefore reasonable to assume that any of these methods would be sufficient to determine the motion of the buoy. For the rest of this chapter, as well as the additional research, numerical simulation will be the primary method employed.

5.7.1 2-D Analysis

Since the numerical model was shown to be highly accurate for the 1-D case, the 2-D case can simply be studied numerically and have equally accurate results.

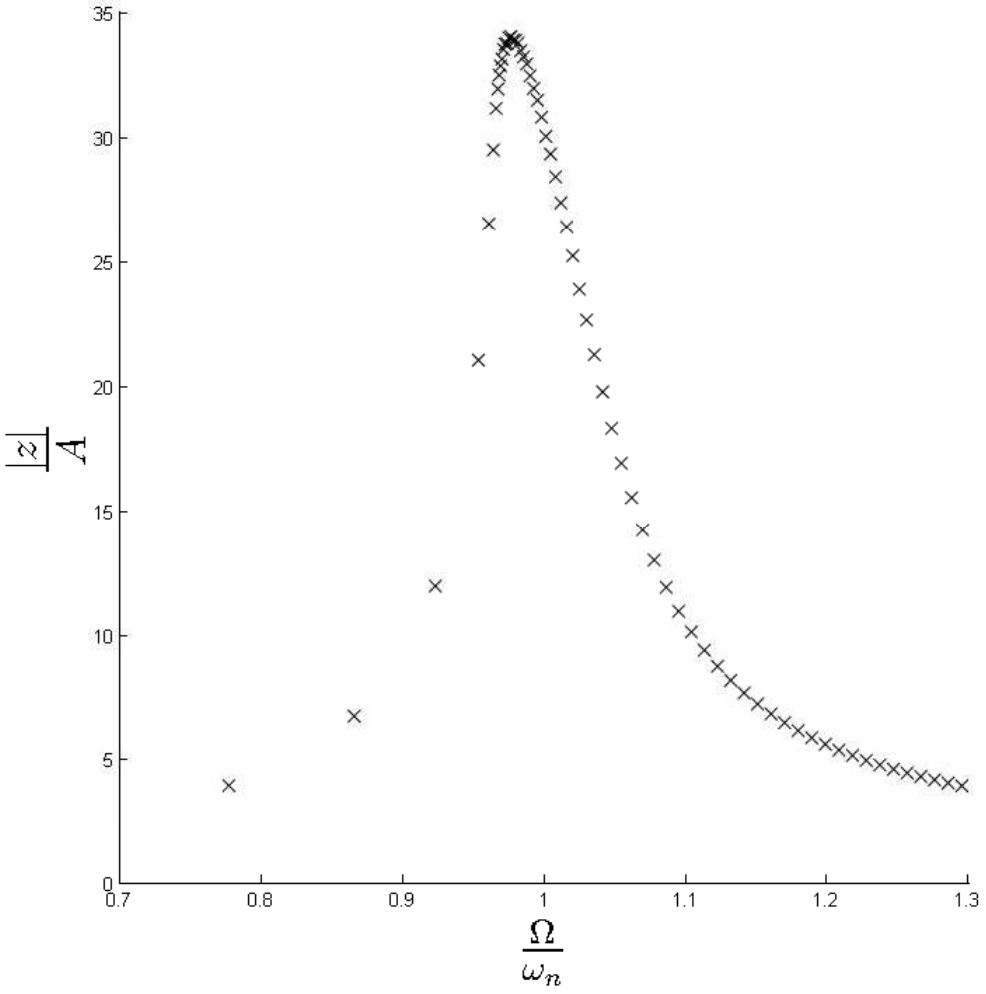

FIGURE 5.12: Frequency response curve found using numerical continuation ($m_b = 0.5$ kg, $A = 0.003$ m)

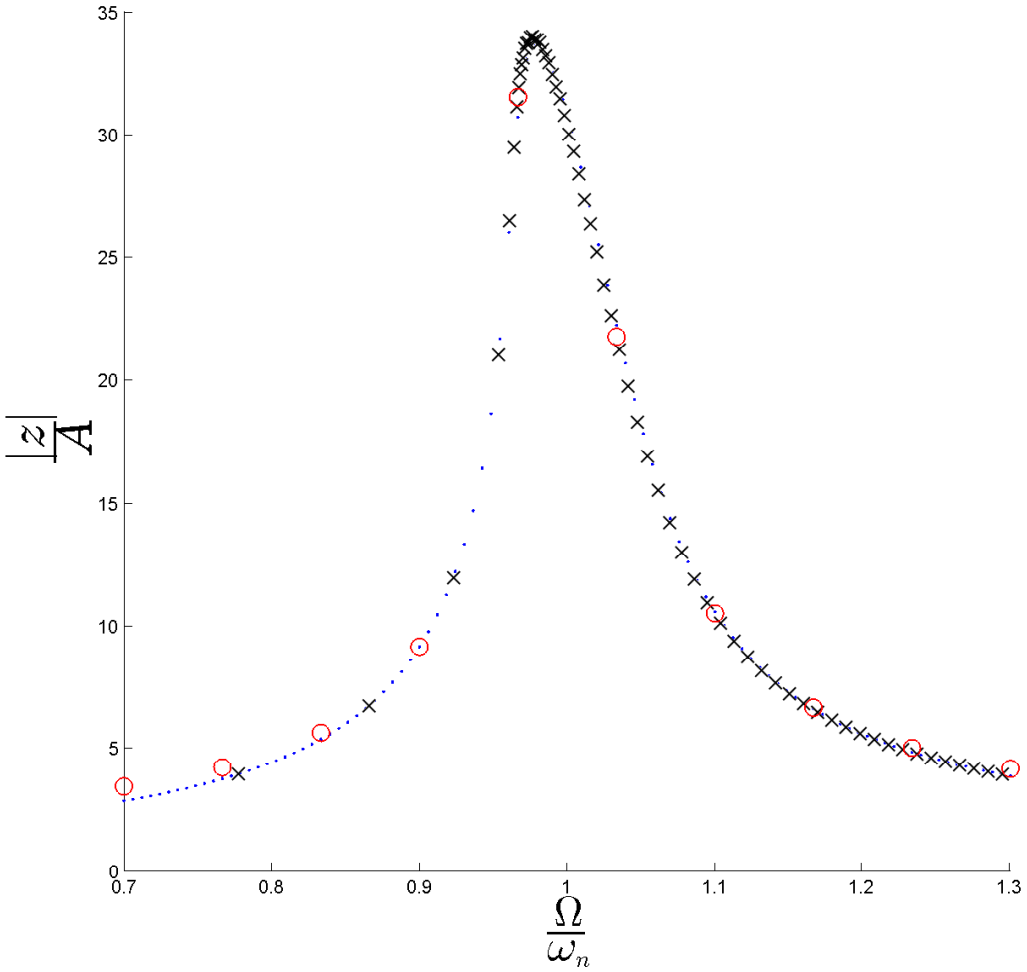

FIGURE 5.13: Frequency response curve comparison for numerical (red squares), analytical (blue dots), and continuation (black x's) ($m_b = 0.5$ kg, $A = 0.003$ m)

5.8 Experimental Comparisons

In order to determine the validity of the numerical simulation as well as the assumptions it makes, the numerical output was compared to experimentally obtained data. First, the exact form of the traveling wave created in the wave tank was determined using image processing software. This same software was then used to track the movement of the buoy due to wave loading. The experimental data obtained by the software was then compared to numerical simulation. Additionally, multiple masses were realized by inserting granular material into the buoy, and experiments were repeated for the new masses.

5.8.1 Experimental Procedure

To track the buoy in the wave tank, image processing software was used, as shown in Fig. 5.14. By adding a distinctive marker to the buoy, this single point can

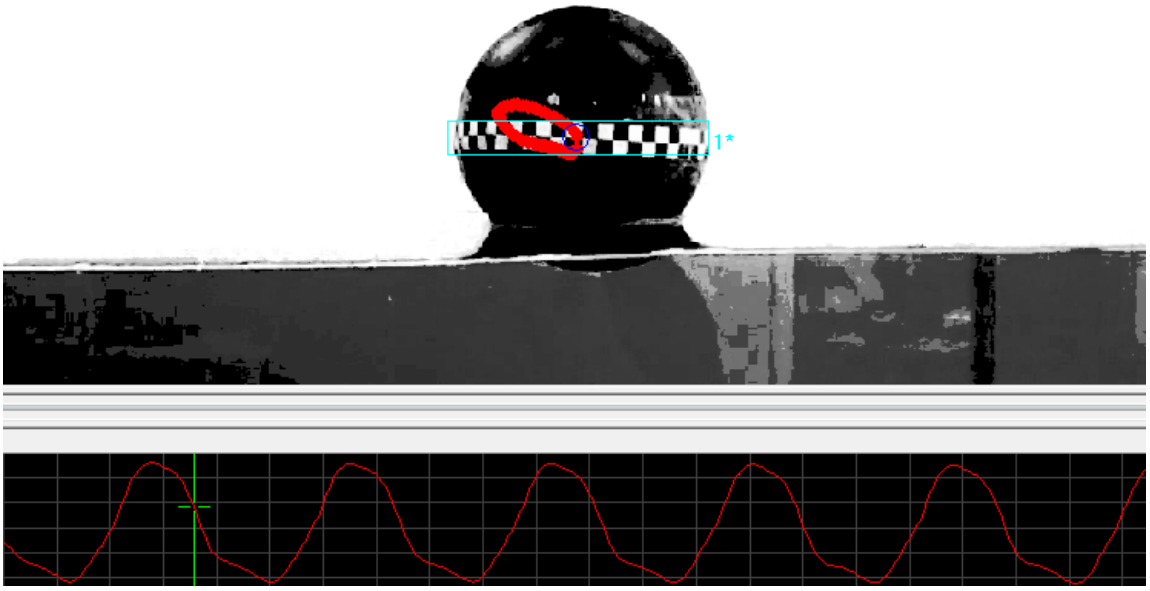

FIGURE 5.14: Snapshot of image processing software used to track buoy, including vertical position output graph.

be observed by the software. Tracking this point gives the horizontal and vertical

positions and velocities of the buoy and allows for comparison to the theoretical model.

5.8.2 Experimental Comparison to Theory

First, the natural frequency found from Eqn. 5.50 can be compared to experimental values. To do this, the buoy was given an initial displacement in still water and allowed to oscillate. A snapshot of this process is shown in Fig. 5.15.

Figures 5.16-5.17 show that the responses found experimentally match well with the simulation. The differences shown in these figures are partially due to slight discrepancies in the reconstructed Fourier series, which did not match identically with the motion found experimentally. Despite this fact, the amplitudes and phases of the multiple harmonic response remain fairly accurate. The fourth harmonic found in the dynamic behavior section is confirmed experimentally in Fig. 5.18, which shows the frequency response for both numerical simulation and experimentally obtained data taken over a comparable time period. Such a response could not be predicted by a linear model, which demonstrates one example of incorporating nonlinearity to accurately describe the buoys motion.

5.8.3 Linear Natural Frequency About Nonlinear Equilibrium

To determine where interesting behavior may occur, it is beneficial to find the natural frequency of the buoy. This term can be estimated as

$$\omega^2 = \frac{\frac{\partial F_B}{\partial z}\big|_{z=\tilde{z}}}{m_b + m_f(\tilde{z})} \tag{5.46}$$

where the hydrodynamic mass is now a function of the buoys equilibrium position. Using Eqn. 5.5, the buoyancy force can be written as

$$F_B = \frac{\rho g \pi}{3}\left[(2R - (z-w))\left(R + (z-w)\right)^2\right] \tag{5.47}$$

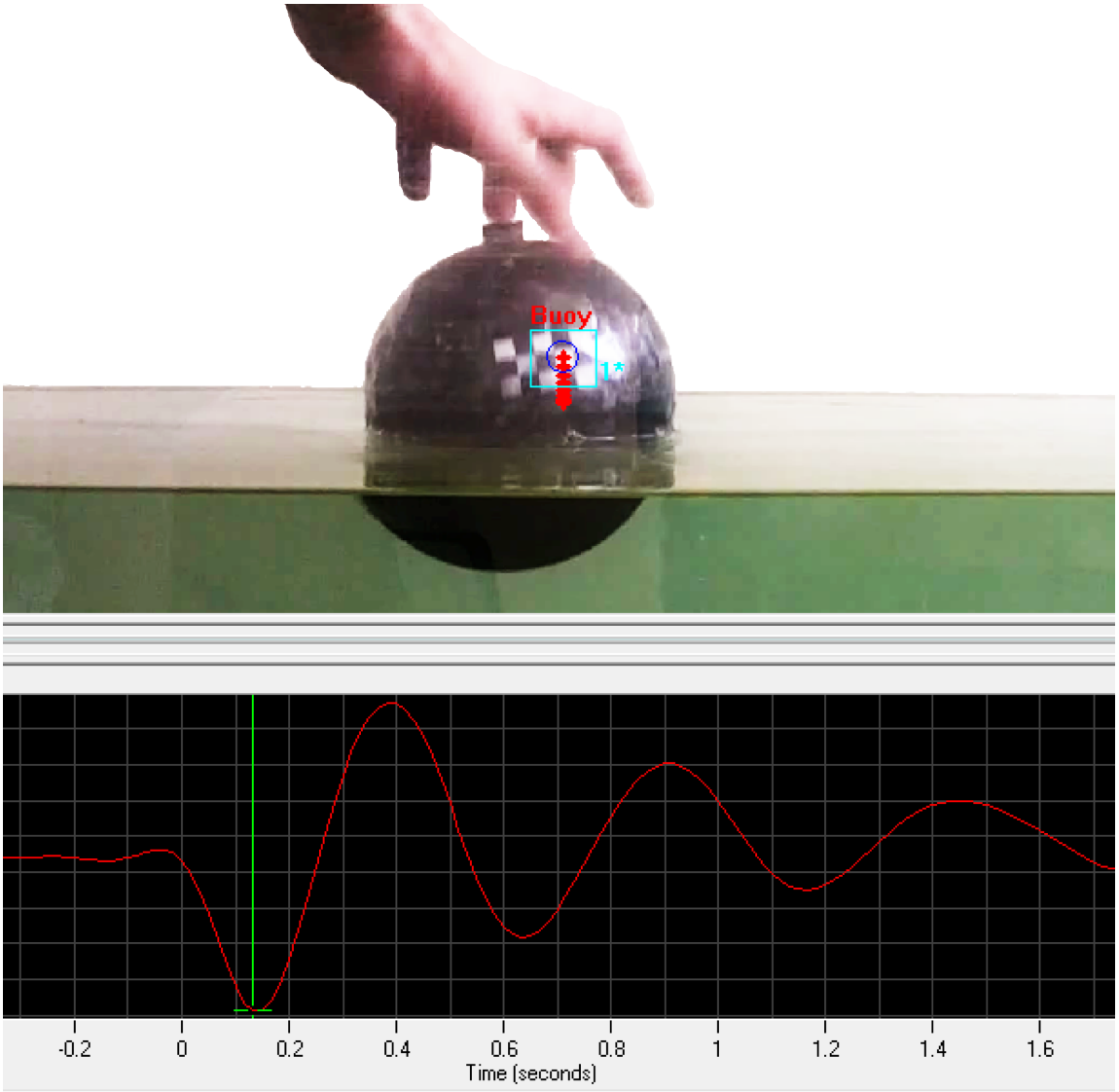

FIGURE 5.15: Snapshot of image processing software used to determine the experimental natural frequency of the buoy.

After taking the derivative and simplifying, this term becomes

$$\frac{\partial F_B}{\partial z}|_{z=\tilde{z}} = \rho g \pi (R^2 - \tilde{z}^2) \tag{5.48}$$

Since this is a static analysis, w is zero. The equation for hydrodynamic mass can be simplified to

$$m_f = \frac{\rho \pi}{6}(2R^3 - 3R^2\tilde{z} + \tilde{z}^3) \tag{5.49}$$

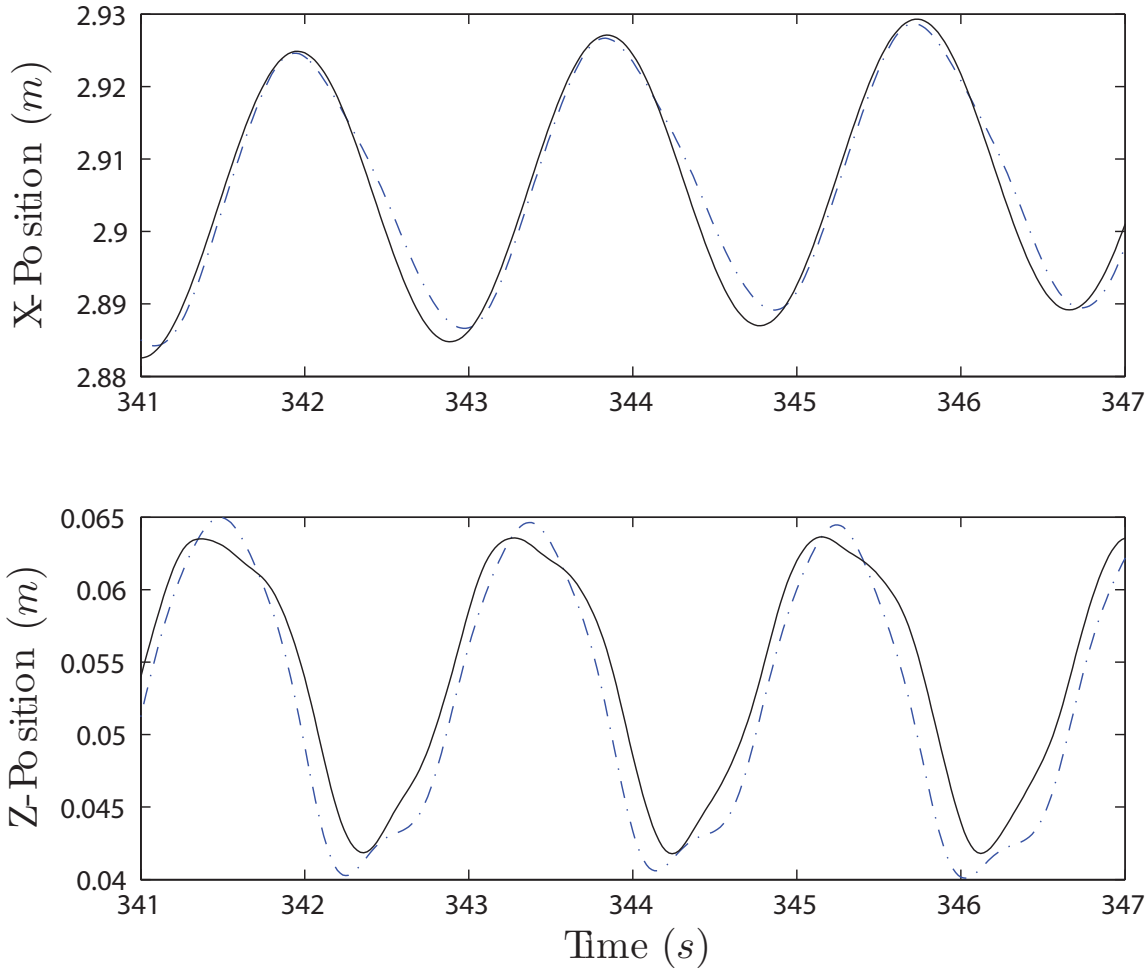

FIGURE 5.16: Horizontal and vertical position comparison: experimental (dashed) vs numerical (solid) for $m_b = 0.1\ kg$.

After combining all of these factors, the natural frequency of the buoy is

$$\omega^2 = \frac{\rho g \pi (R^2 - \tilde{z}^2)}{m_b + \frac{\rho\pi}{6}(2R^3 - 3R^2\tilde{z} + \tilde{z}^3)} \tag{5.50}$$

In this instance, the equilibrium position ($\tilde{z}$) is a function of the buoy mass. This term is easily found by equating the static forces, i.e. setting the buoyancy force equal to the force caused by gravity and solving for $\tilde{z}$, as shown below

$$F_B(\tilde{z}) = \frac{\rho g \pi}{3}\left[(2R - \tilde{z})\,(R + \tilde{z})^2\right] = mg \tag{5.51}$$

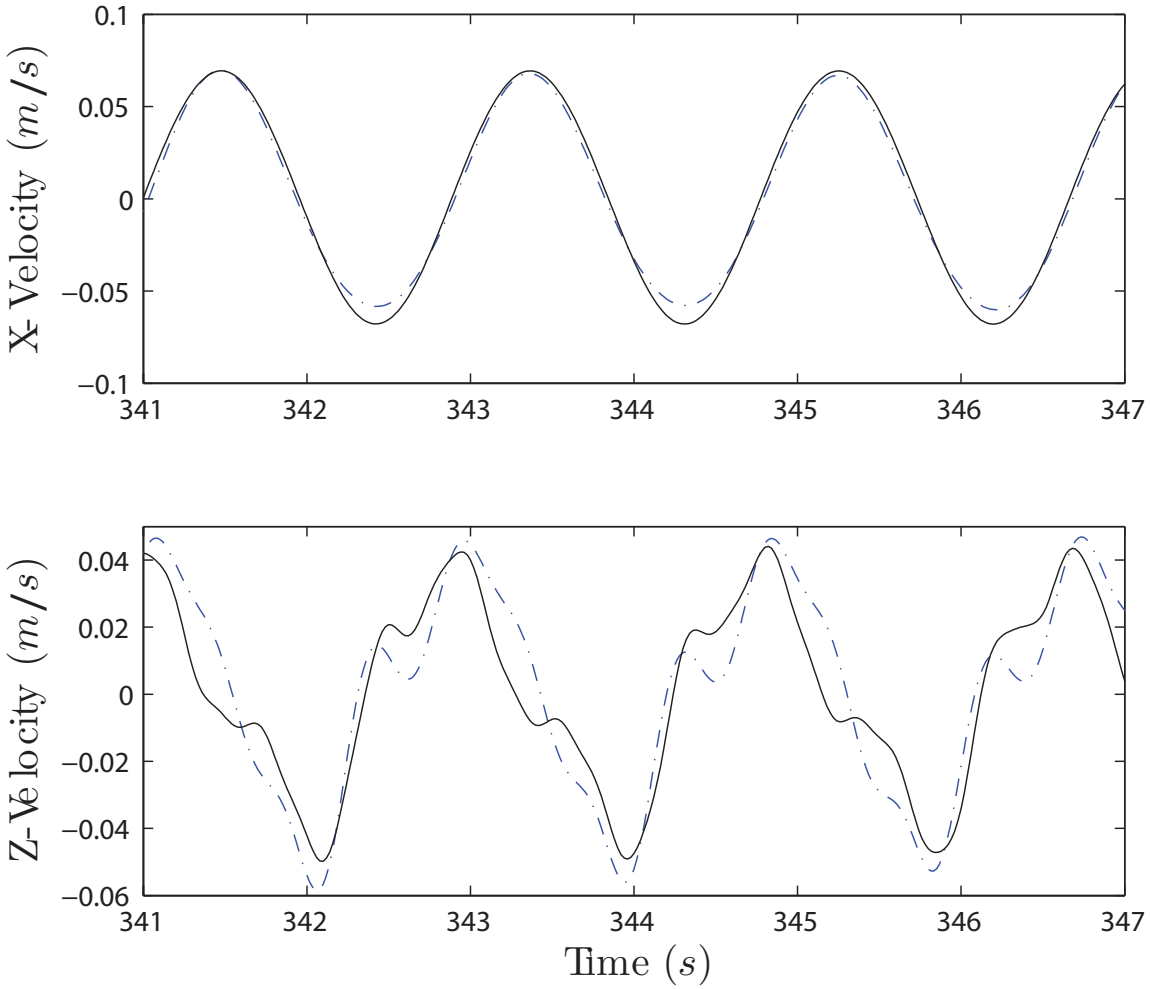

FIGURE 5.17: Horizontal and vertical velocity comparison: experimental (dashed) vs numerical (solid) for $m_b = 0.1\ kg$.

There is now a direct relation between the system parameters and its natural frequency. In order to see sub/superharmonic responses, this natural frequency can be made close to the wave frequency. Mass will be the only variable parameter because it is the easiest to change. How the natural frequency varies with buoy mass is shown below. The simulation matches the analytical curve within six percent for all masses. This formulation was also tested experimentally. The buoy was given an initial displacement in still water and the vertical motion was measured using the motion tracking software. The frequencies found for different masses match within

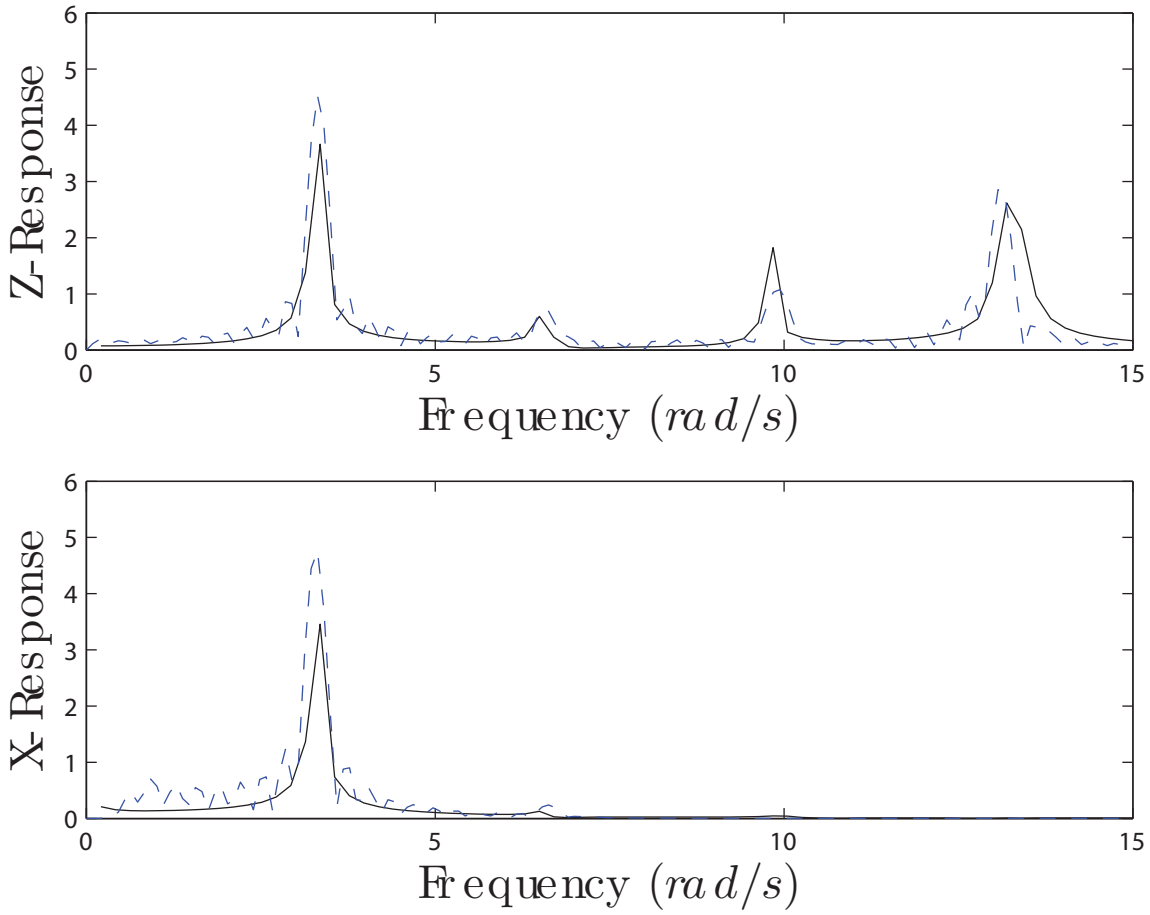

FIGURE 5.18: Velocity frequency response comparison over a short time period for $m_b = 0.62\ kg$: experimental (dashed) vs numerical (solid).

eight percent, as shown in Fig. 5.20.

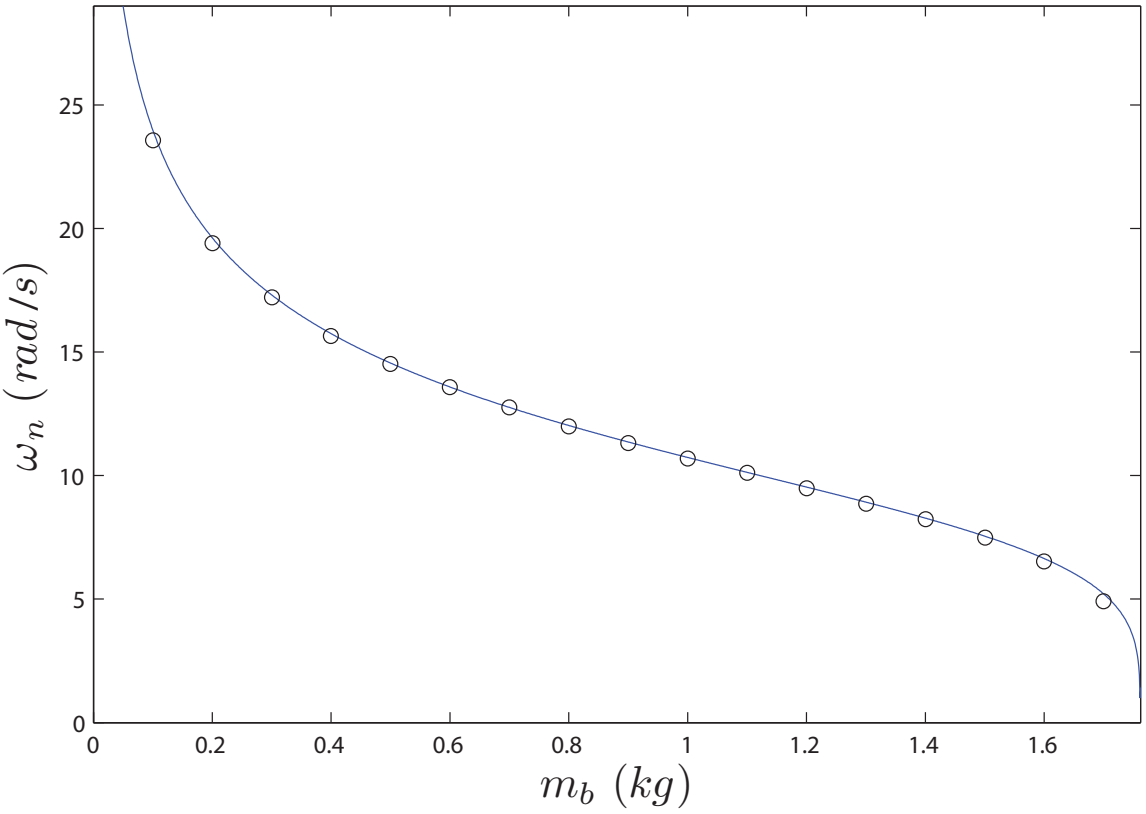

FIGURE 5.19: ω_n vs buoy mass: comparisons of the predicted natural frequency from Eqn. 5.50 (solid) and numerical simulation (circle).

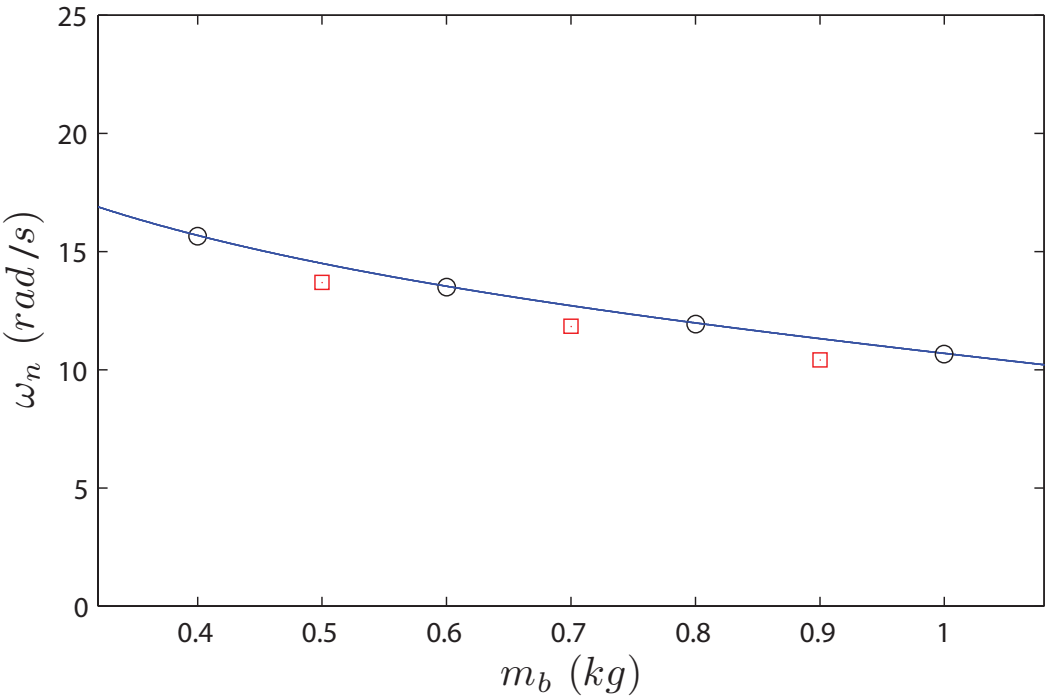

FIGURE 5.20: ω_n vs buoy mass: comparisons of the predicted natural frequency from Eqn. 5.50 (solid), numerical simulation (circle) and experimental (square).

5.9 Linear Model

To illustrate the importance of the nonlinear model, it is compared to a linear one. Both formulations will assume only 1-D vertical motion.

5.9.1 Linear Model Assumptions

Multiple changes are required to both the linear and nonlinear equations in order to accurately compare the two. First, the damping term is now written as

$$\text{Damping Term} = 2\zeta\omega_n\dot{z}. \tag{5.52}$$

This type of damping is appropriate for the linear case, but will also used in the nonlinear formulation. This is done in order to place emphasis on the nonlinearity of the V_{sub} and m_f terms. Other changes are made in the linear case, including

$$\dot{V}(x,0,t) = -A\Omega^2\cos(\Omega t), \tag{5.53}$$

$$V_{sub} = \frac{2}{3}\pi R^2(H_{sub}), \tag{5.54}$$

and

$$m_f = \frac{2}{3}\rho\pi R^3, \tag{5.55}$$

For these to be accurate for the linear case, the buoy must oscillate about its center (i.e. $\tilde{z} = 0$). Therefore, the buoy mass is set to 0.88 kg for both formulations.

5.9.2 Comparison to Nonlinear Model

The first wave forcing frequency is lowered to 0.9π rad/s, which corresponds to one-fourth of the buoys natural frequency. Using the same wave amplitudes at the second through fourth harmonics, the two responses are compared in Fig. 5.21 and Table 5.2. The deficiency of the linear formulation in accurately predicting responses at the natural frequency can now be seen. The nonlinear formulation correctly predicts

the large response at the natural frequency, while the linear formulation yields a significantly lower response.

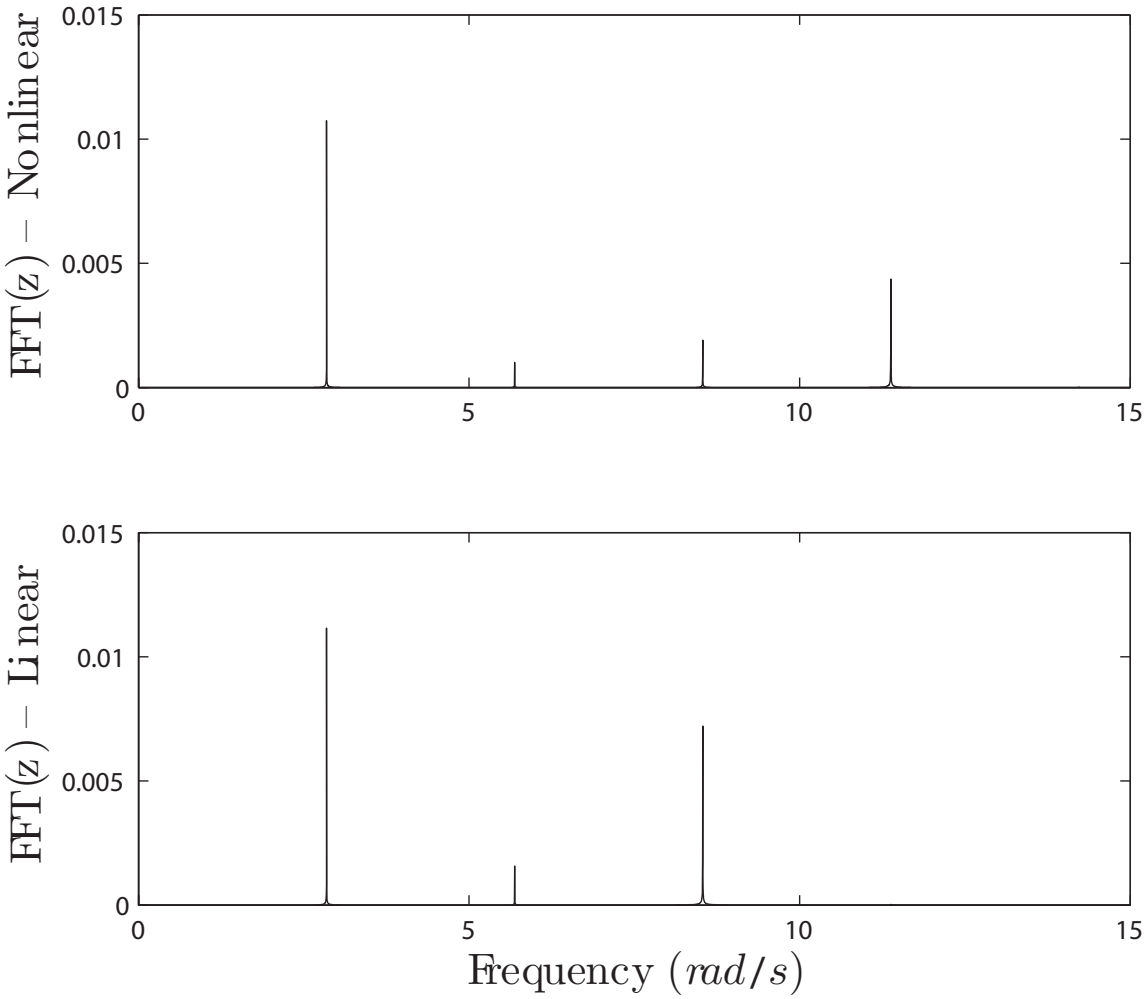

FIGURE 5.21: Frequency response comparison for linear vs nonlinear cases: $m_b = 0.88\ kg$.

Table 5.2: Linear vs. Nonlinear Response for $m_b = 0.88\ kg$

Frequency	$A_n\ (mm)$	Nonlinear $\frac{z_n}{A_n}$	Linear $\frac{z_n}{A_n}$
Ω	11	1	1
2Ω	0.8	1.3	2
3Ω	0.9	2.1	8.1
$4\Omega\ (\omega_n)$	0.08	52.4	0.4

5.10 Conclusions

In ocean energy harvesting, not only is it important to fully understand the dynamics of the harvester itself, but also the mechanism by which the wave energy is transferred to the harvester. By doing a full nonlinear analysis of the spherical buoy, areas of potential efficiency increase were shown through the inherent nonlinearities of the buoy. The buoy was studied by using numerical simulation, deriving an analytical solution, and employing numerical continuation. This data was shown to be accurate and was then confirmed experimentally by tracking the sphere in the wave tank using image processing software. A linear model was also derived, and was shown to fail at predicting large displacements at frequencies other than the forcing frequency.

6

Nonlinear Dynamics of a Cylindrical Buoy

6.1 Introduction

Many studies have been conducted on a cylindrical buoy shape for both floating [19] and submerged [73] designs. As with the spherical buoy, most of these studies stipulate that the cylinder is tethered in some fashion [54]. In addition, many studies have been performed on cylinders that are directly attached to the ocean floor, in which case only the reaction forces are observed. Again in this chapter, a buoy setup is observed that is free to move in both the horizontal and vertical directions. In addition, the cylindrical buoy is now also free to rotate in the 2-D plane. Only this planar motion is considered since it was sufficient to describe the majority of the motion observed in experimental trials in the wave tank.

The cylindrical buoy exhibits significantly more complicated motion than its spherical counterpart. Being allowed to rotate in 2-D space has a large effect on the overall response. This also means that, as opposed to the spherical buoy, changing the position of the added mass along the vertical direction has a significant effect on the buoys behavior. Studies have also been performed and generalized for cylin-

drical buoys with an arbitrary cross section [76]. For our purposes, a buoy with a circular cross section is the only shape studied.

6.2 Problem Setup

This section sets up a mathematical description of the cylindrical buoy. It gives a general design that allows for changing the buoy mass, as well as the buoys center of gravity. The geometry of the cylinder is described in detail, including how it is affected by the passing waves.

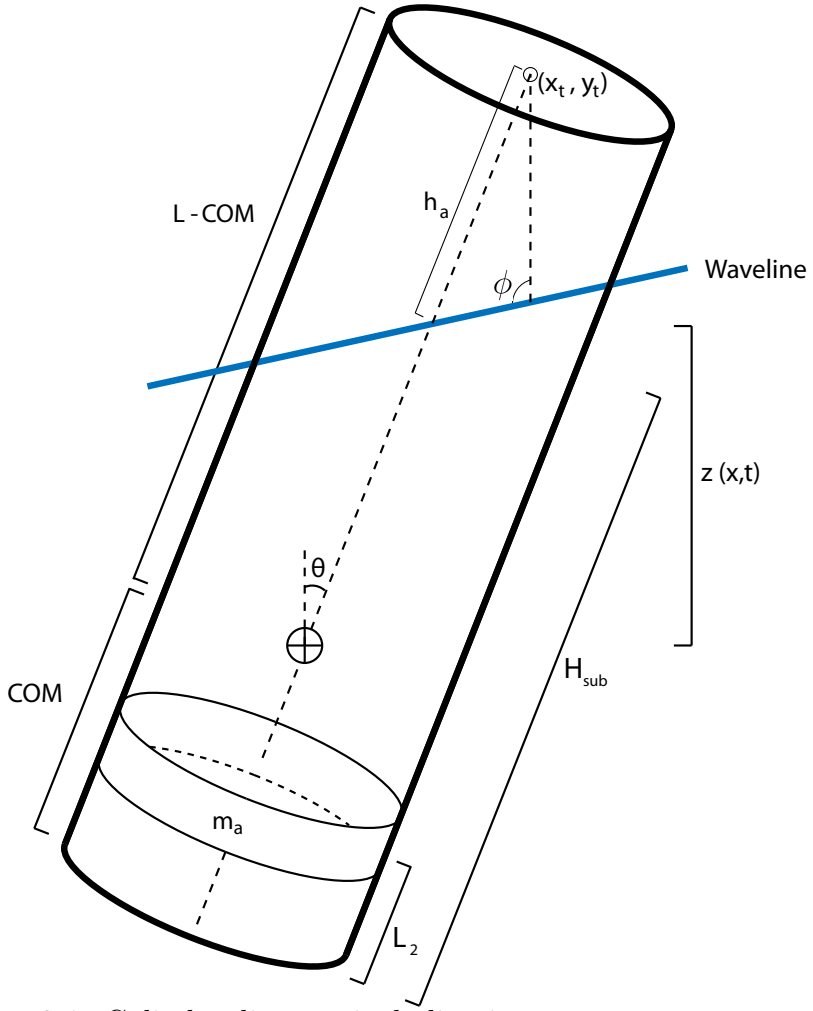

FIGURE 6.1: Cylinder diagram including important system parameters.

6.2.1 Geometric Relationships

As with the spherical buoy, the submerged volume V_{sub} is the most important term for the cylindrical buoy. The main assumption made in this section, similar to previously, is that the waveline is straight across the buoy, though its angle is allowed to change. First, the distance from the bottom of the cylinder to the added mass is defined as L_2 and the distance to the overall center of mass as C. To find the submerged height H_{sub}, the length of the buoy above the water h_a is subtracted from the total buoy length L. Using the parameter definitions shown in Fig. 6.1, h_a becomes

$$h_a = \frac{y_t - w(x_t, t)}{\sin(\pi - \phi - \theta)} \sin\phi, \tag{6.1}$$

given

$$x_t = x_0 + (L - C)\sin\theta, \tag{6.2}$$

$$y_t = z + (L - C)\cos\theta, \tag{6.3}$$

$$\phi = \frac{d}{dx}(w(x,t))|_{x_t} + \frac{\pi}{2}, \tag{6.4}$$

where (x_t, y_t) are the coordinates of the top of the cylinder, θ is the buoy tilt, and ϕ is a function of the wave angle. Then, the submerged height is simply

$$H_{sub} = L - h_a. \tag{6.5}$$

6.2.2 Vertical Equation of Motion

As done in the previous chapter, the motion in the vertical direction is easily described by using Morison's equation.

$$(m_t + m_f)\ddot{z} + m_t g = \rho V_{sub}\left(g + C_M\dot{V}\right) + \frac{1}{2}\rho A_Z C_D\,(V - \dot{z})\,|V - \dot{z}| \tag{6.6}$$

where m_t is the total mass, as in

$$m_t = m_c + m_a, \tag{6.7}$$

where m_c is the mass of the actual cylinder without the added mass m_a. V_{sub} is written as

$$V_{sub} = \pi \frac{D^2}{4} H_{sub}, \tag{6.8}$$

where H_{sub} is taken from Eq. 6.5.

6.2.3 Horizontal Direction

The horizontal equation of motion for the cylinder is written as

$$(m_t + m_f)\ddot{x} = \rho V_{sub} C_M \dot{U} + \frac{1}{2}\rho A_x C_D \left(U - \dot{x}\right)\left|U - \dot{x}\right|. \tag{6.9}$$

As in the spherical buoy chapter, U is the horizontal water velocity and is a function of t, x, and z. This spatial dependence was neglected in the previous chapter since the fluid velocity changes only slightly along the curved surface of a small spherical buoy. For the cylindrical buoy, however, this change in fluid parameters must be accounted for. Therefore, for the total force in the horizontal direction, the forces found from Morison's equation that have spatial dependence are integrated and averaged across the relevant surface. This is, as in the previous chapter, still ignored for the vertical forces, since the diameter of the cylinder is much less than its length.

6.2.4 Simple Rotation

In order to describe the buoyancy force as the cylinder rotates, modeling the center of mass of the displaced fluid is required. Utilizing [55] this center of mass can be described by

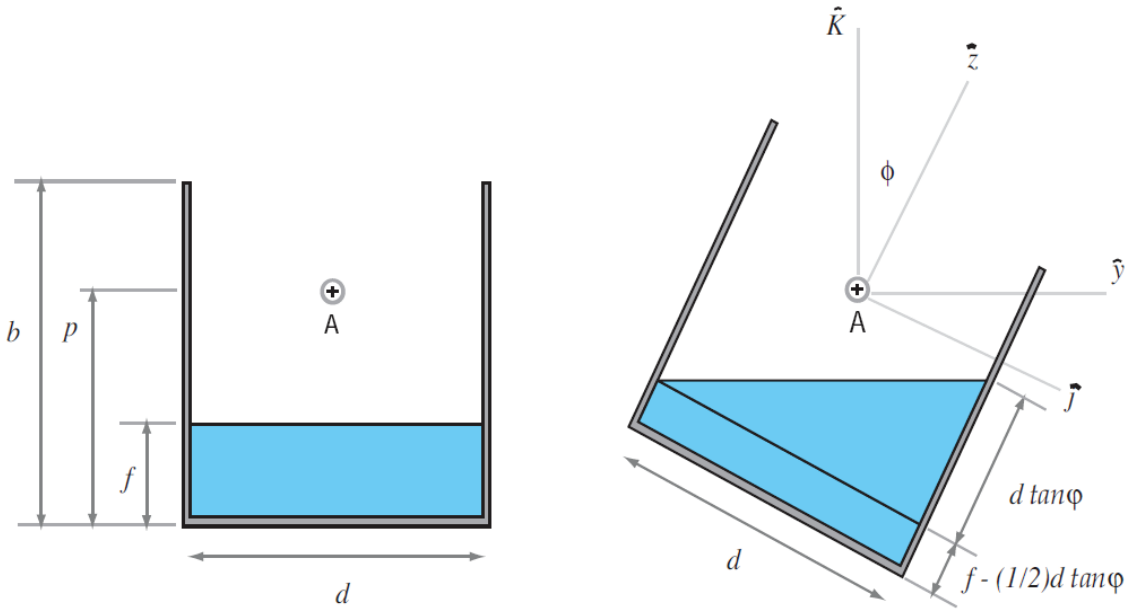

FIGURE 6.2: Taken from [55], this figure shows the parameters of a fluid filled container system used to calculate the center of fluid mass around the cylindrical buoy.

$$\bar{y} = \frac{D^2 \tan\theta}{16f} \tag{6.10}$$

$$\bar{z} = \frac{f}{2} - p + \frac{(D\tan\theta)^2}{32f} = -\frac{f}{2} + \frac{(D\tan\theta)^2}{32f} \tag{6.11}$$

This is because $f = p$ in this specific case. Knowing these values, the moment equation for the cylinder becomes

$$I_T\ddot{\theta} + F_B\left(\cos\theta\bar{y} + \bar{z}\sin\theta\right) - \frac{1}{2}\rho(H_{sub}D)C_D\dot{\theta}|\dot{\theta}|\bar{z} = 0, \tag{6.12}$$

where I_T is the total inertia of the buoy. This term can be solved for by initially describing the inertia of the cylinder itself,

$$\int_{-\frac{L}{2}}^{\frac{L}{2}}\int_{0}^{2\pi}\int_{r_1}^{r_2}\rho_c\left((r\sin(\theta)^2 + z\right)r \quad dr\,d\theta\,dz, \tag{6.13}$$

where r_1 and r_2 are the inside and outside radii of the thin-walled cylinder, respectively, and ρ_c is the mass density of the buoy, written as

$$\rho_c = \frac{m_c}{\pi(r_2^2 - r_1^2)L} \tag{6.14}$$

Solving this equation, we get that the inertia of the cylinder itself is

$$I_c = \frac{1}{12}m_c L^2 + \frac{1}{4}m_c\left(r_1^2 + r_2^2\right). \tag{6.15}$$

To account for the added mass, the parallel axis theorem is used, which gives a total inertia of

$$I_T = \frac{1}{12}m_c L^2 + \frac{1}{4}m_c\left(r_1^2 + r_2^2\right) - m_a\left(\frac{L}{2} - C\right)^2. \tag{6.16}$$

6.3 Static Analysis

This section analyzes how the cylindrical buoy reacts in still water. The buoy is given a small initial displacement to create oscillatory motion, which is then studied. This section also observes how changing buoy parameters affect qualities such as the natural frequency.

6.3.1 Linear Natural Frequency About Nonlinear Equilibrium

As shown in the previous chapter, the linear natural frequency can be estimated as

$$\omega^2 = \frac{\frac{\partial F_B}{\partial z}\big|_{z=\tilde{z}}}{m_b + m_f(\tilde{z})}. \tag{6.17}$$

For the cylindrical buoy, the buoyancy force is written as

$$F_B = \rho g V_{sub} = \rho g \frac{\pi D^2}{4} H_{sub} \tag{6.18}$$

where H_{sub} is simply

$$H_{sub} = \frac{L}{2} - z \tag{6.19}$$

since $w = 0$ in the static case. As before, m_f is proportional to the displace mass, except the ratio is now $1:1$ (since C_A for a cylinder is 1). Therefore, the hydrodynamic mass becomes

$$m_f = \rho V_{sub} = \rho \frac{\pi D^2}{4} \left(\frac{L}{2} - \tilde{z} \right). \tag{6.20}$$

The equilibrium position ($\tilde{z}$) is again found by balancing the buoyancy and gravity forces

$$m_t g = \rho g V_{sub}, \tag{6.21}$$

which results in

$$\tilde{z} = \frac{L}{2} - \frac{4m_t}{\rho \pi D^2} \tag{6.22}$$

Putting all of these terms together, the natural frequency simplifies to

$$\omega_n = \sqrt{\frac{\rho g \pi D^2}{8m_t}}. \tag{6.23}$$

Figure 6.3 shows how this natural frequency changes with buoy mass, as well as a comparison of this analytical natural frequency to that found with numerical simulation.

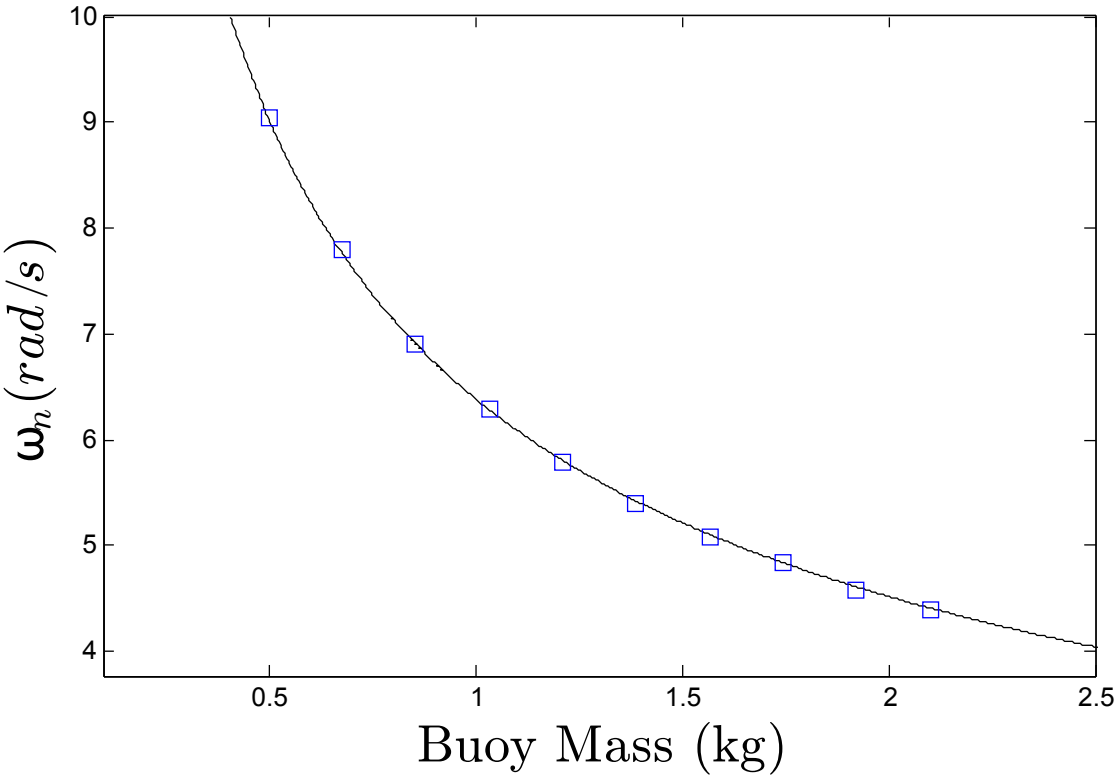

FIGURE 6.3: This figure shows how the natural frequency of the cylindrical buoy changes with increasing buoy mass. The analytical solution is also compared to the solution found through numerical simulation (analytical:solid black line, numerical: blue boxes)

Changing Parameters

It is beneficial to observe how the system changes when varying different parameters. Figure 6.4 shows how changing the cylinder diameter D affects the natural frequency curve. From this figure, it is clear that an increasing mass decreases the natural frequency, while an increasing diameter increases the natural frequency. This is as expected, since Eqn. 6.23 shows that ω_n decreases proportional to $\frac{1}{\sqrt{m_t}}$ and increases proportional to D. This is also somewhat intuitive: natural frequency is generally inversely proportional to mass, while increasing the buoy diameter increases the buoyancy force (and therefore natural frequency) since the buoyancy force is proportional to D^2. Figure 6.5 shows this trend from a different view, with ω_n increasing

with D. This linear trend confirms the linear dependence of the natural frequency to D in Eqn. 6.23, as mentioned previously.

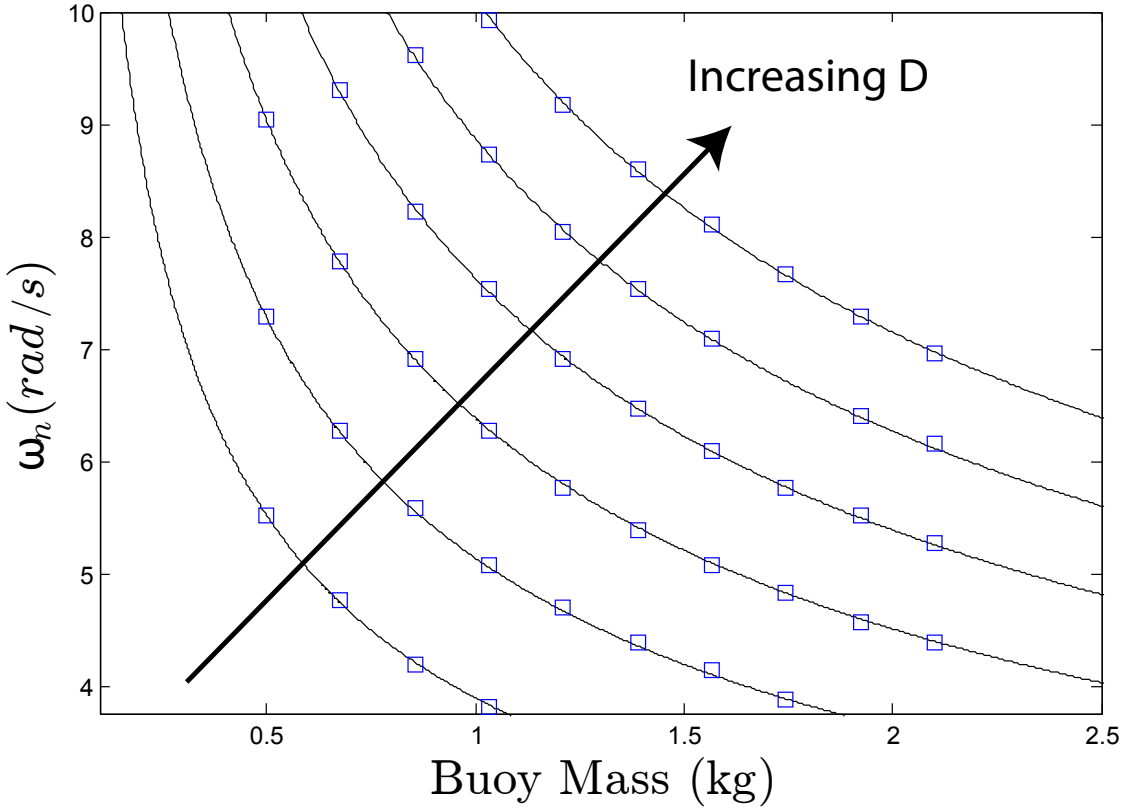

FIGURE 6.4: Natural frequency dependence on total buoy mass (m_t) and trend observed by increasing the cylinder diameter (D)

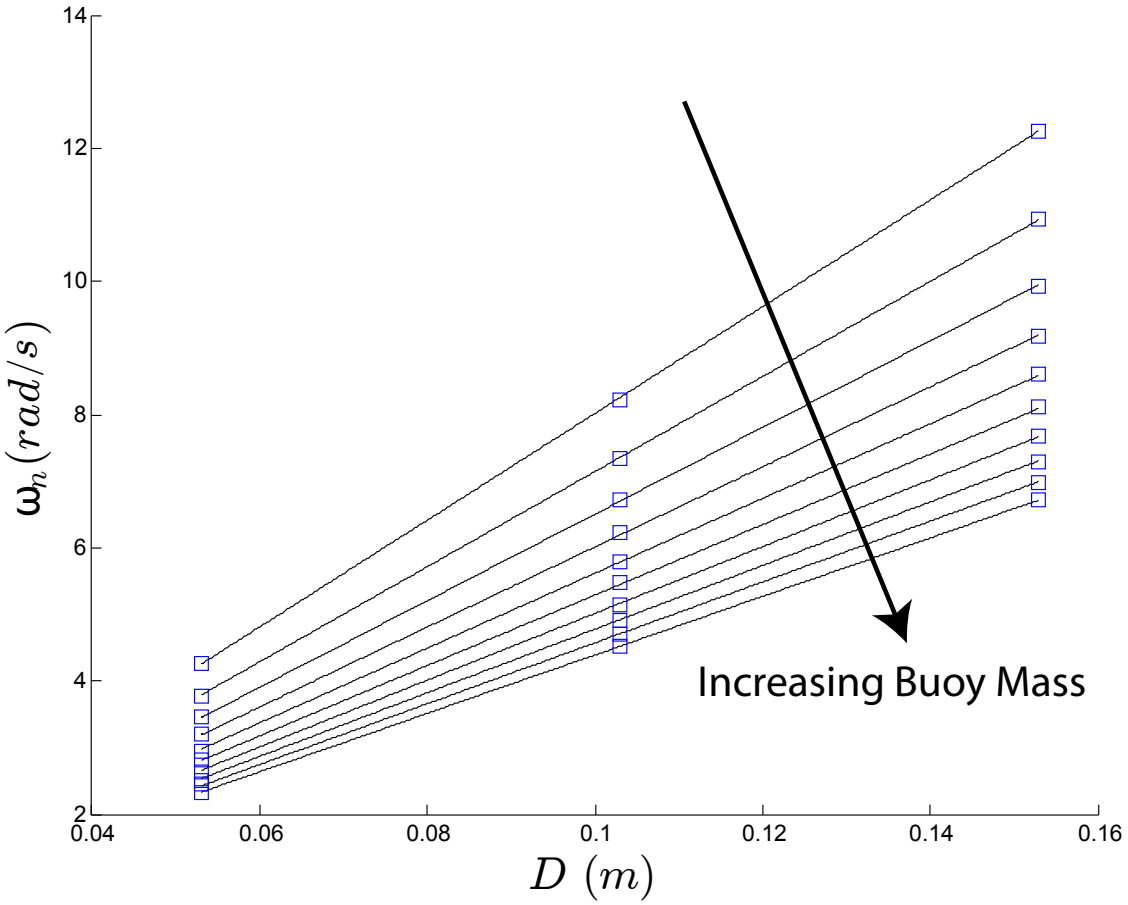

FIGURE 6.5: Natural frequency dependence on the cylinder diameter (D) and trend observed by increasing the total buoy mass (m_t)

6.4 Numerical Modeling of Dynamic Behavior

Now that the equations of motion for the cylindrical buoy have been derived, this motion can be simulated numerically. As shown in Fig. 6.6, the buoy oscillates in the vertical, horizontal, and angular directions while also traveling in the positive horizontal direction. This particular simulation had a forcing frequency of $0.4\omega_n$. If we increase the forcing frequency to $0.6\omega_n$ and $0.8\omega_n$, for example, we get the results in Figs. 6.7 and 6.8, respectively.

Figure 6.9 shows the frequency spectrum for the vertical component of the 2-D motion. Figure 6.10 shows the spectrum for the vertical, horizontal, and angular

cylinder motion. It can be seen in these three figures that as the forcing frequency increases, the vertical and horizontal amplitudes also increase, as expected, while the angular motion has a different shape.

It should be noted that, since the horizontal motion includes both an oscillating and drift component, these two motions were solved for separately. Fig. 6.10 shows only the oscillating component, which has a significantly smaller amplitude than its vertical counterpart. These values were found by detrending the horizontal motion data (i.e. taking out the linear trend) and then finding the oscillation amplitudes. To find the drift amplitudes, the slope of the linear trend is calculated. This can be seen in Fig. 6.11. The drift motion spectrum has an almost identical shape to that of the vertical motion, though with different amplitudes. It can also be seen that for the majority of the frequency spectrum shown, the drift amplitude is significantly larger than the oscillation amplitude.

6.4.1 Numerical Continuation

As with the spherical buoy, numerical continuation (more specifically collocation) is implemented for comparisons to the 1-D vertical solution found with numerical simulation. Figure 6.4.1 shows the frequency response for the solution from continuation. As previously mentioned for the spherical buoy, however, numerical simulation will be used to obtain further information about the 2D motion. Since these two methods were shown to correlate well, either is sufficient to gather relevant data.

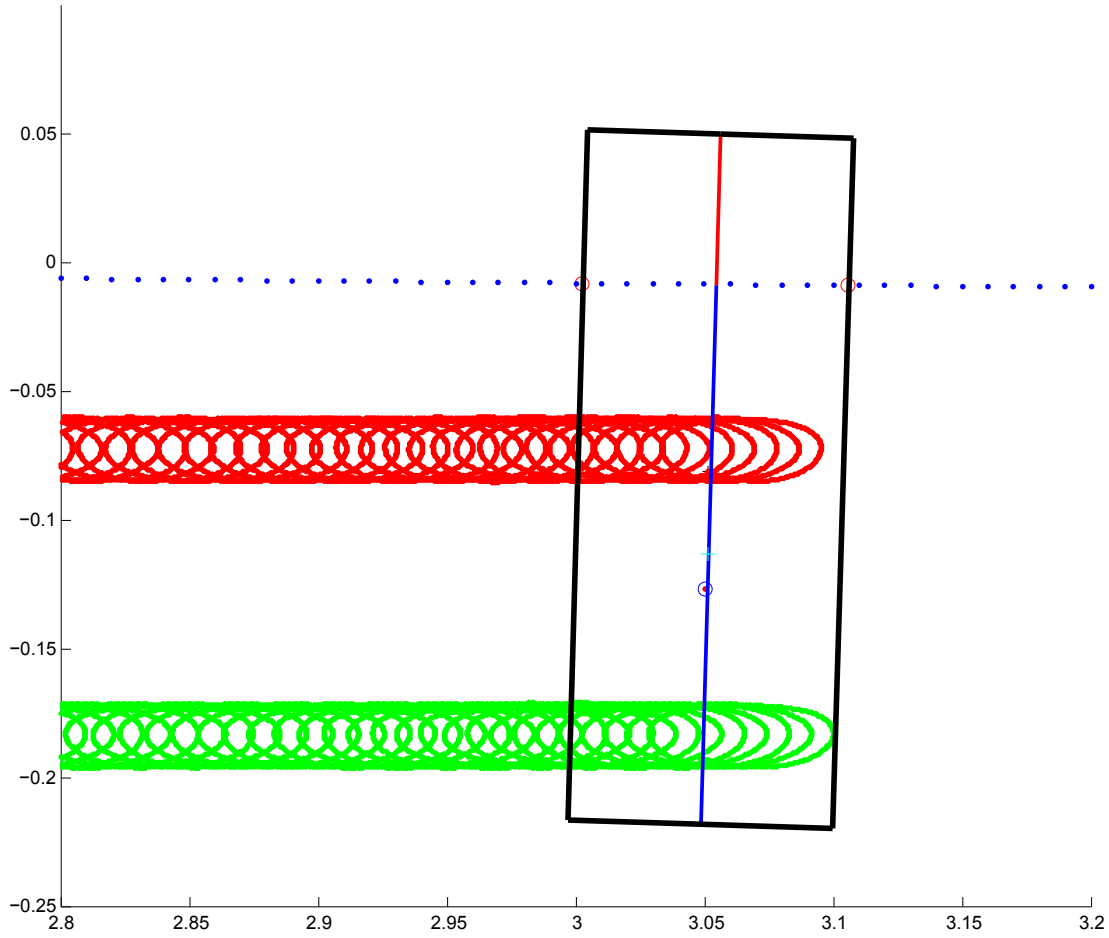

FIGURE 6.6: Numerical simulation of 2D motion of the cylindrical buoy. The buoy exhibits vertical, horizontal, and angular harmonic oscillations, while the horizontal direction also has a traveling component. This motion is for a forcing frequency of $0.4\omega_n$.

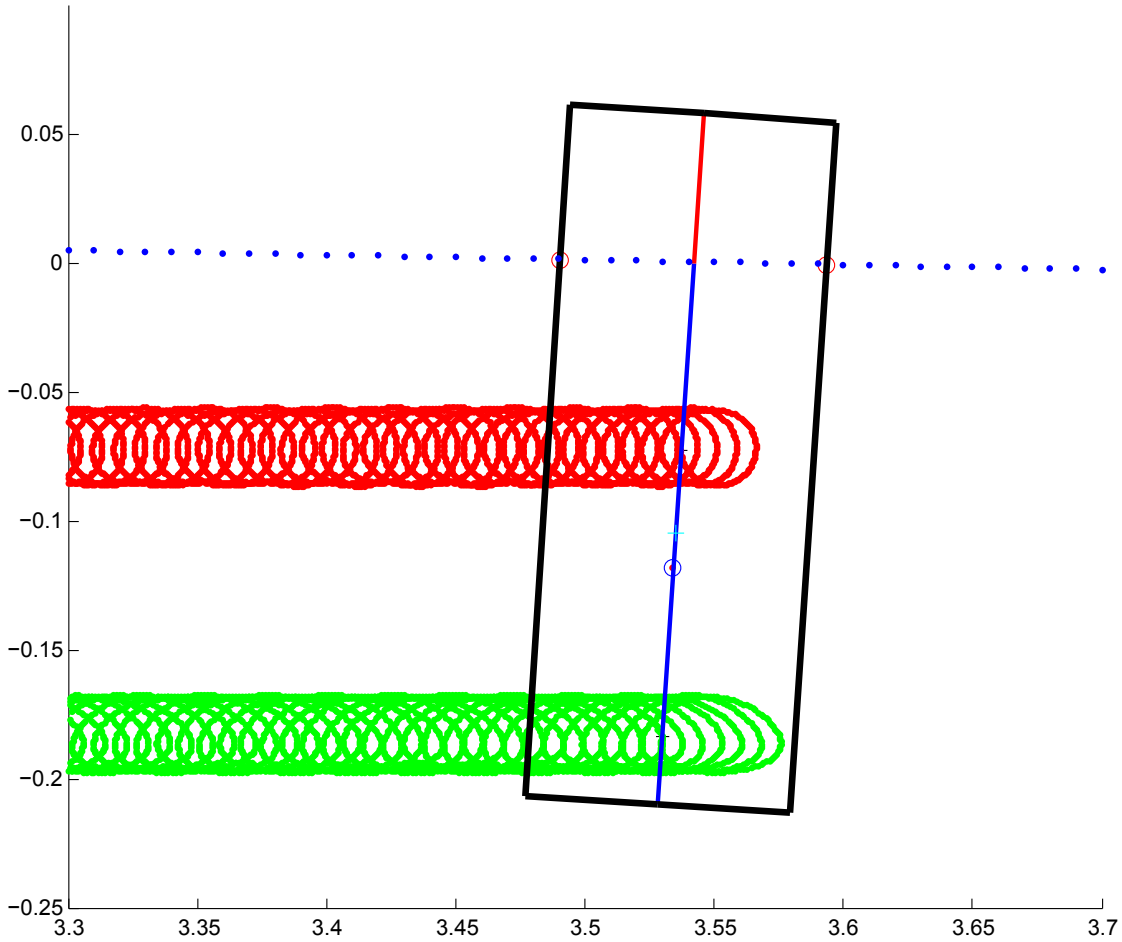

FIGURE 6.7: Numerical simulation of 2D motion of the cylindrical buoy. This motion is for a forcing frequency of $0.6\omega_n$.

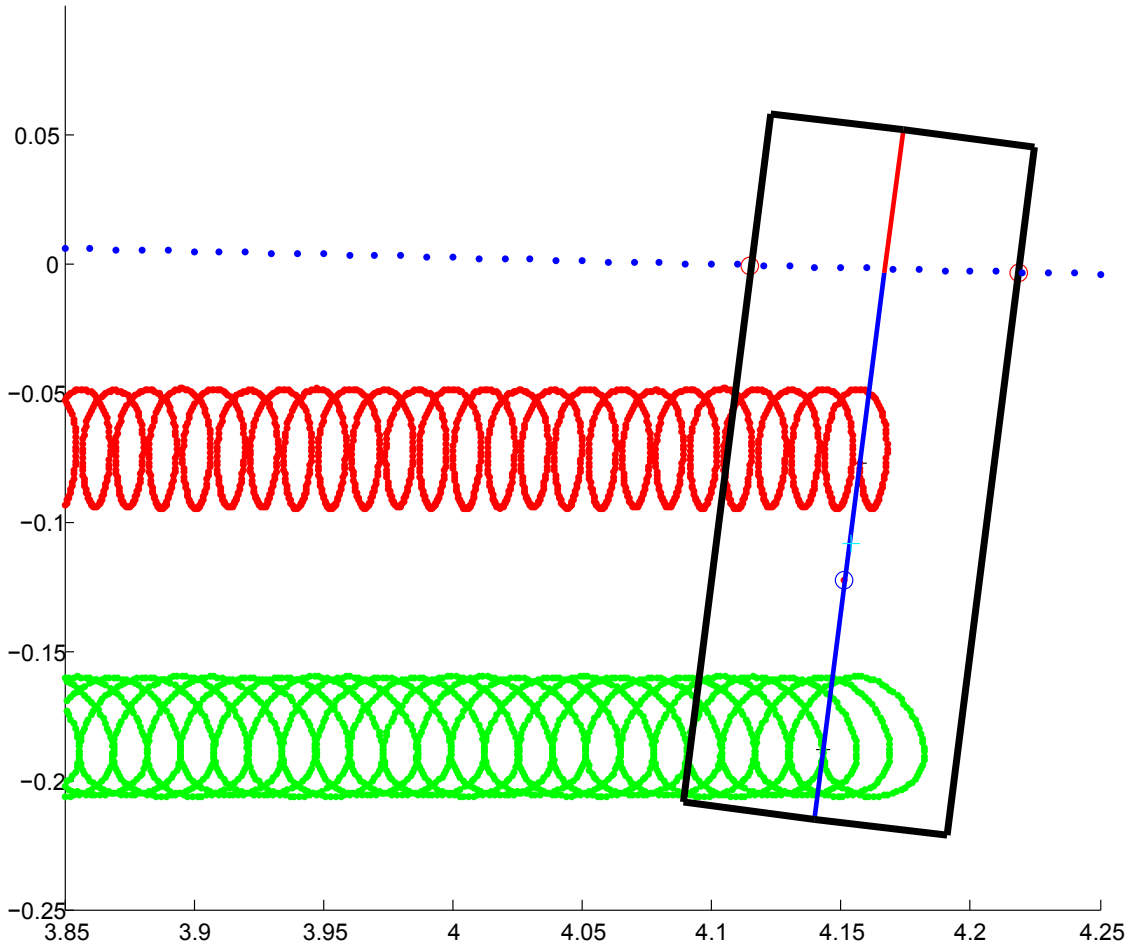

FIGURE 6.8: Numerical simulation of 2D motion of the cylindrical buoy. This motion is for a forcing frequency of $0.8\omega_n$.

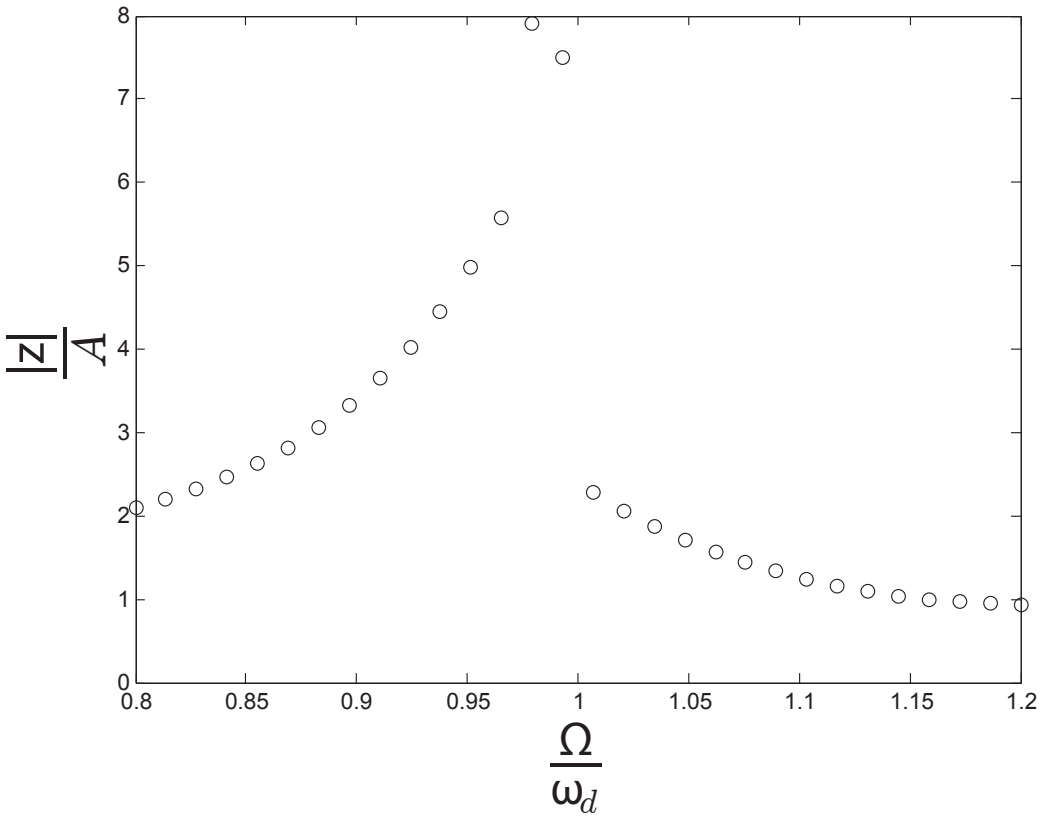

FIGURE 6.9: Frequency response of the cylindrical buoy during 2D motion, only vertical oscillation amplitude ratio shown.

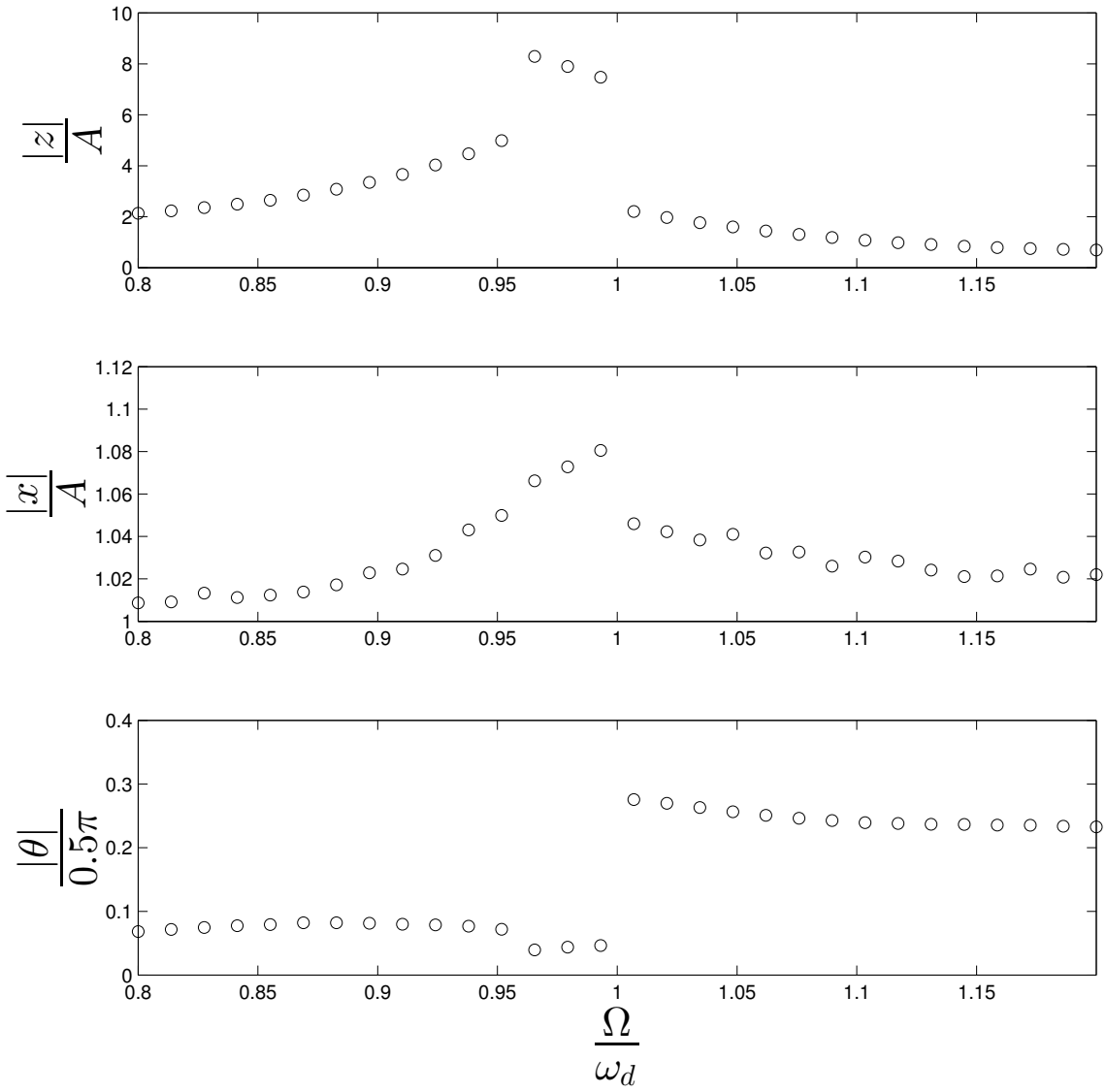

FIGURE 6.10: Frequency response of the cylindrical buoy during 2D motion, with vertical, horizontal and angular amplitude ratios shown

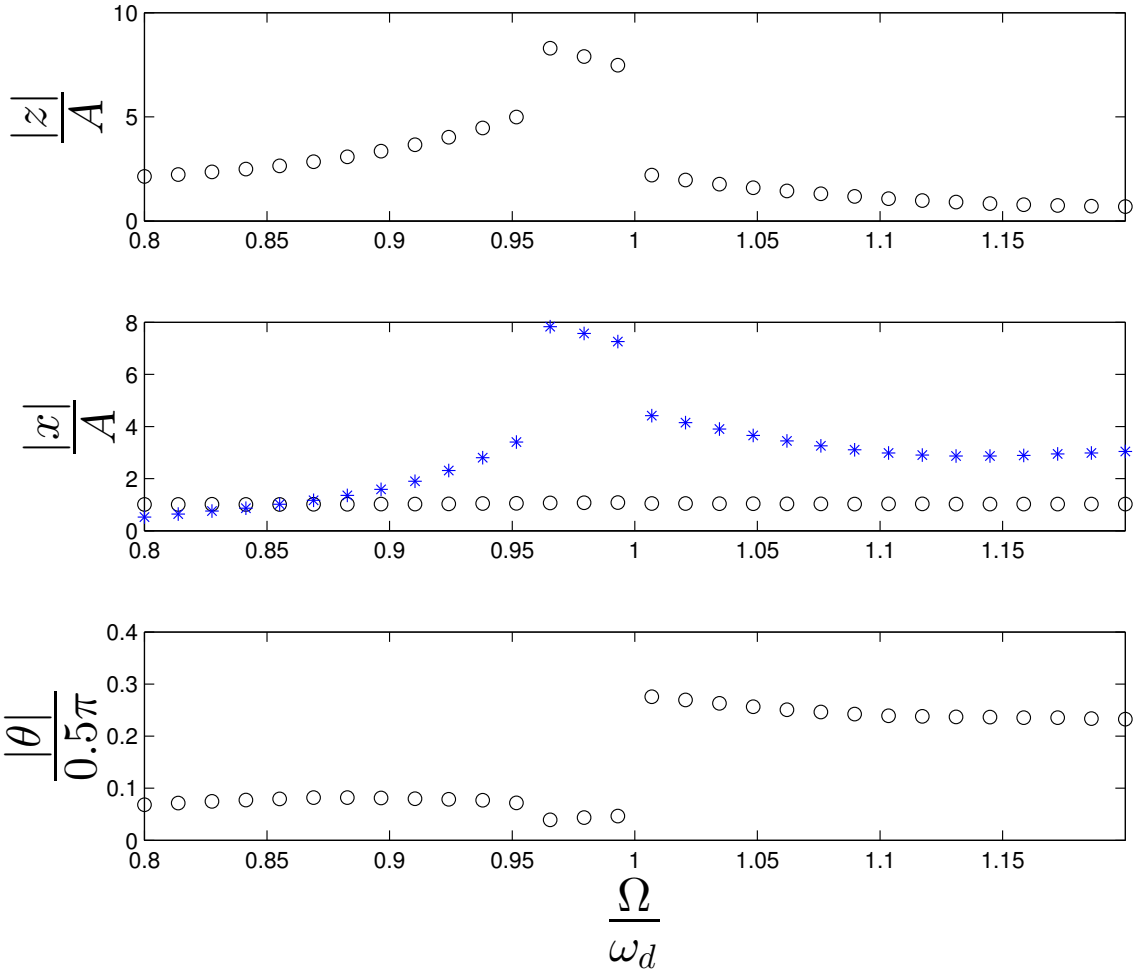

FIGURE 6.11: Frequency response of the cylindrical buoy during 2D motion, with vertical, horizontal and angular amplitude ratios shown, now including linear trend (i.e. drift, blue star)

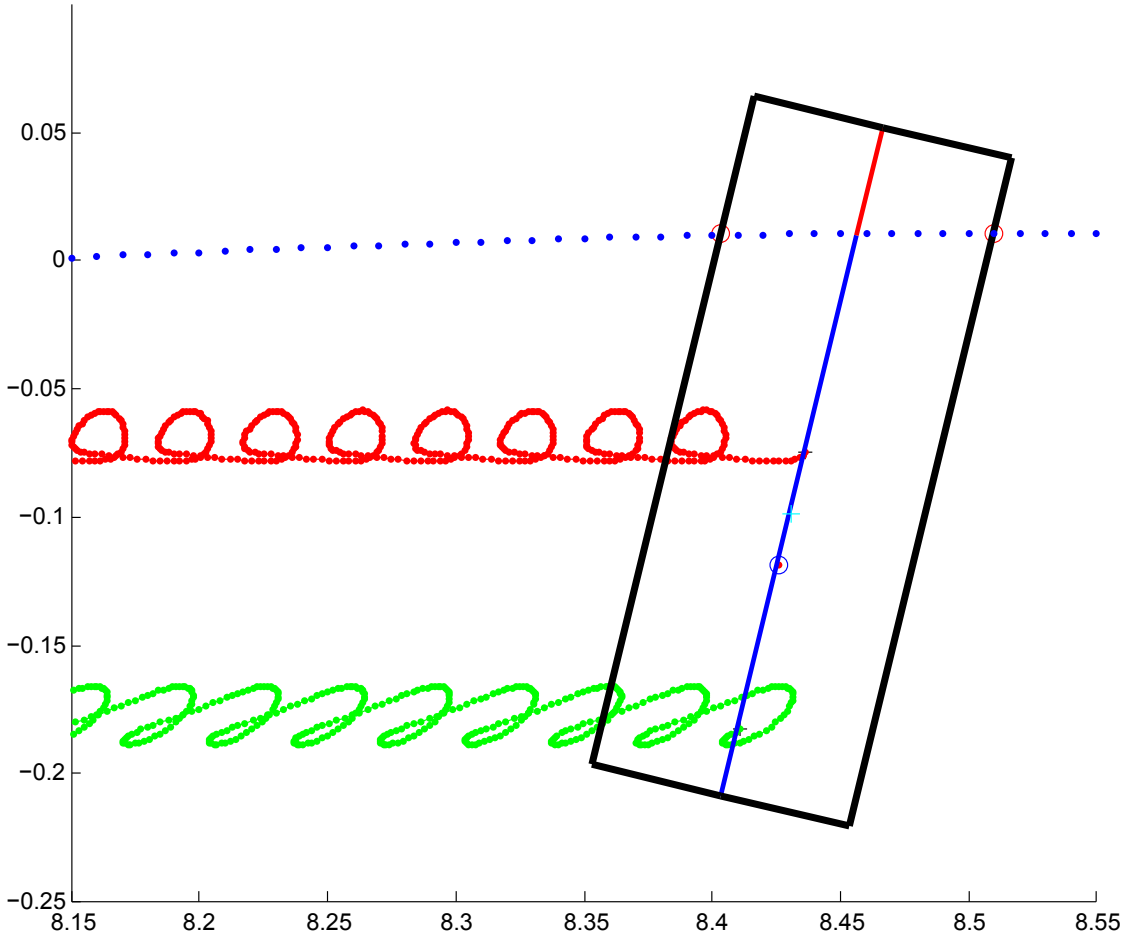

FIGURE 6.12: Numerical simulation of 2D motion of the cylindrical buoy. This motion is for a forcing frequency of $1.2\omega_n$., showing large increase in horizontal oscillation amplitude.

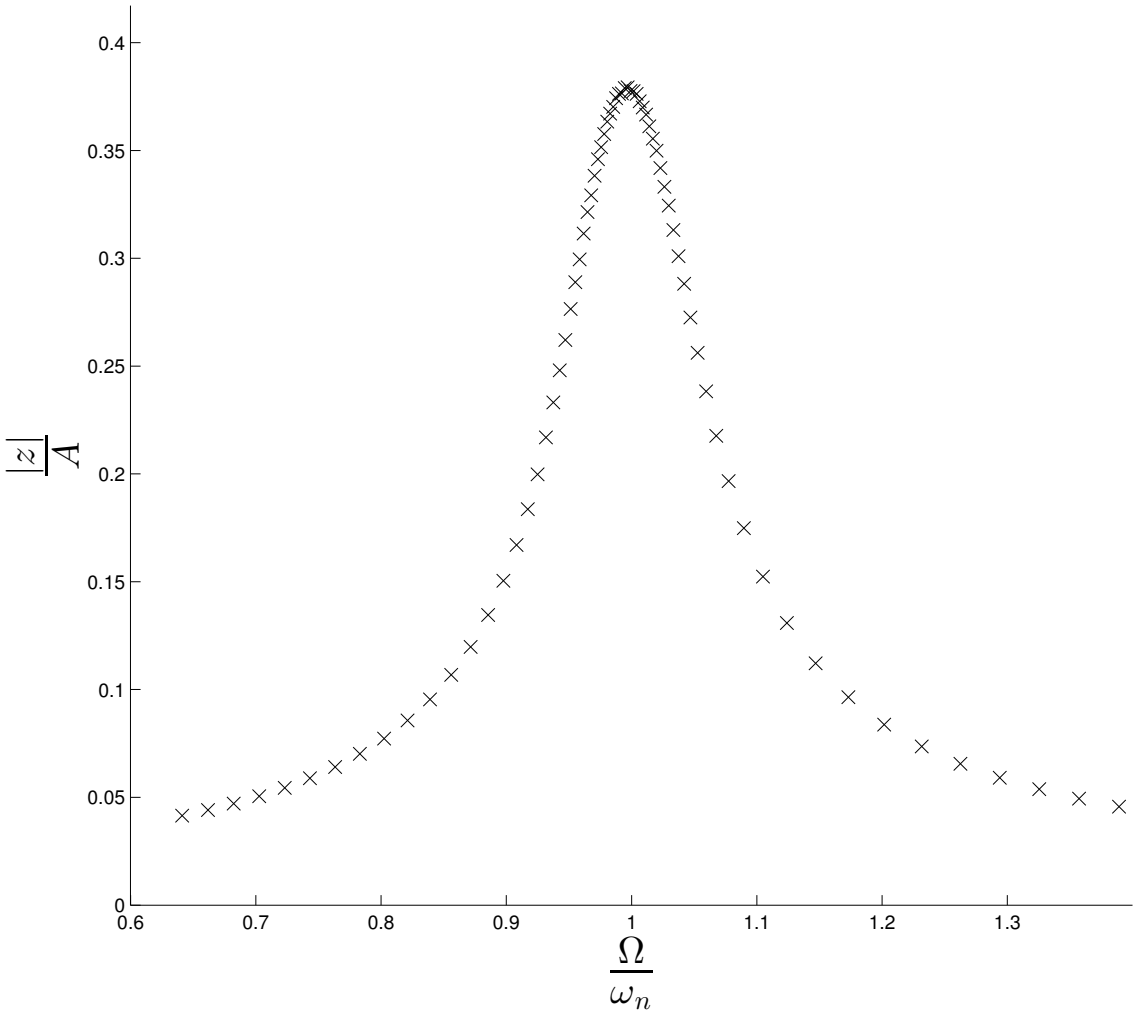

FIGURE 6.13: Frequency response graph for the cylindrical buoy using numerical continuation for the 1-D vertical scenario.

6.5 Analytical Model

6.5.1 1-D Vertical Solution

The analytical model for the cylindrical buoy is almost identical to that of the spherical buoy, with a few minor changes. First, there is a different projected area in the vertical direction (A_z). Since only the vertical motion is considered, this is simply the constant

$$A_z = \pi R^2. \tag{6.24}$$

Additionally, there is a different formula for the submerged volume V_{sub}, which was already derived in Eqn. 6.8. Every other element of the analytical formulation is the same as in Ch. 5.

Figure 6.5.1 shows the frequency response of the analytical solution found for the cylinder. This frequency response graph shows no hardening or softening characteristics, which is different from the sphere. This is simply because of the fact that they buoyancy force for the cylinder is linear with the vertical displacement, as opposed to the sphere which has a z^3 relationship.

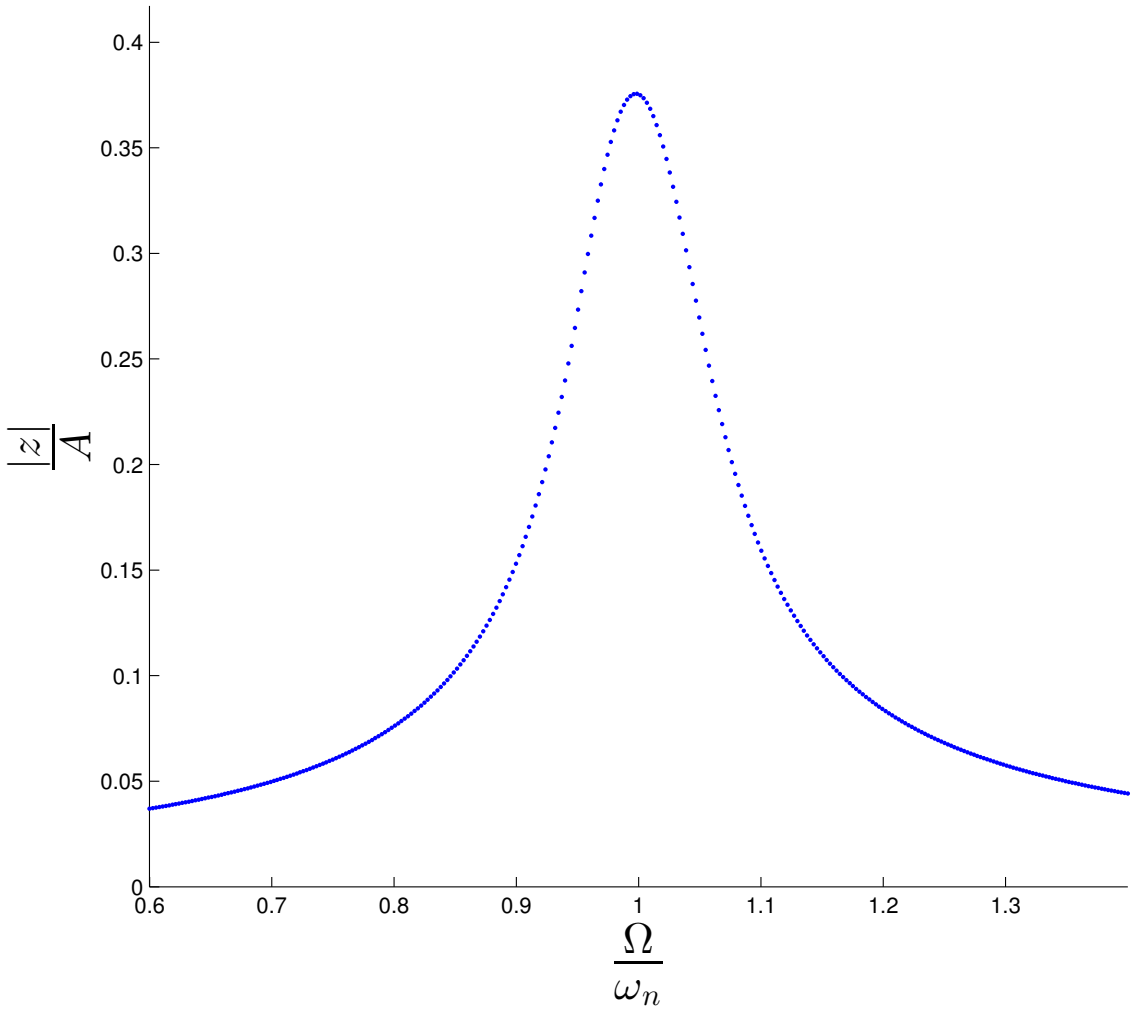

FIGURE 6.14: Frequency response graph for the cylindrical buoy using the analytical formulation for the 1-D vertical scenario.

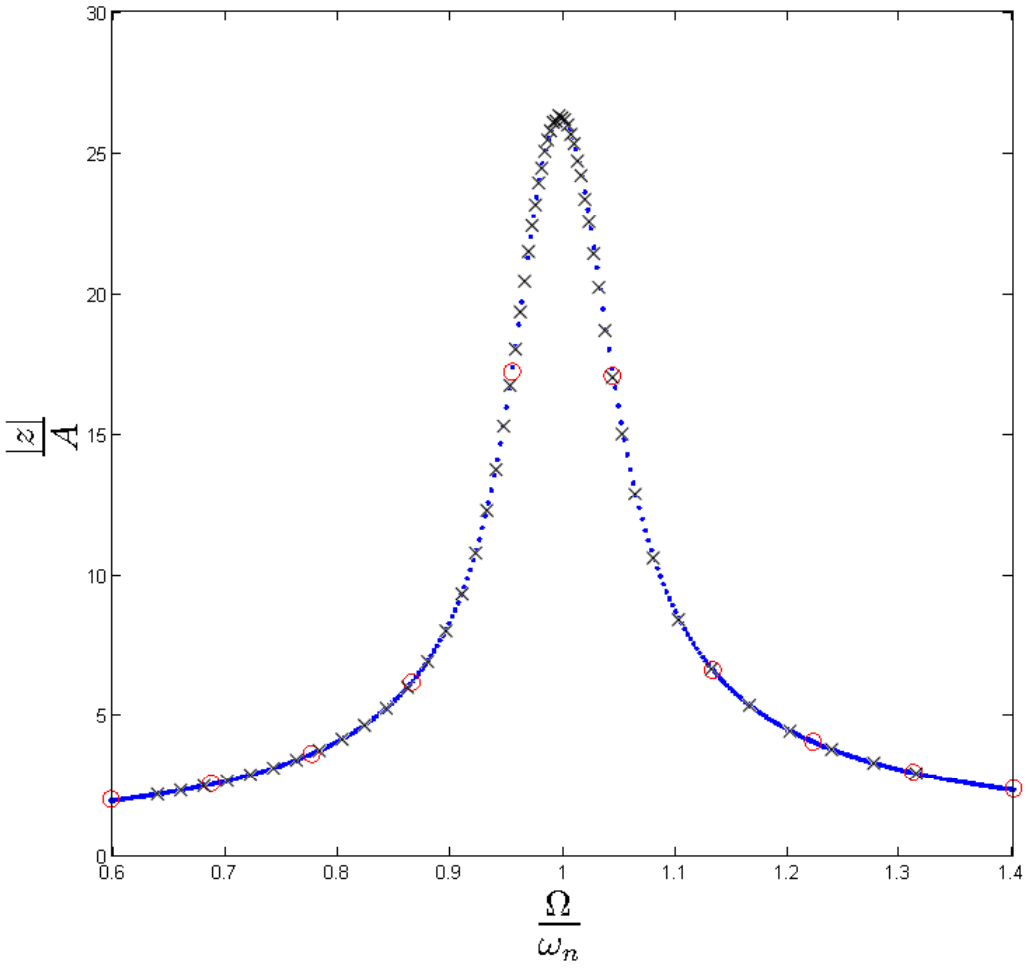

FIGURE 6.15: Frequency response comparison for numerical (red squares), analytical (blue dots), and continuation (black x's)

6.6 Conclusions

As with the spherical buoy, a full nonlinear analysis of the cylindrical buoy is vital to create an efficient ocean energy harvesting system. A static analysis was performed and a derivation of the buoys natural frequency was shown to be accurate for both numerical and analytical formulations. It was also shown how this natural frequency changes with altering parameters such as the buoy mass and diameter. The cylindrical buoy was then studied through numerical simulations and an analytical solution was derived. In the planar motion, it was shown that significant drift can occur in the horizontal direction for multiple forcing frequencies. Finally, solutions were compared for numerical simulation, the analytical solution, and numerical continuation and shown to be accurate.

7

Harvesting Energy from Athletics for an Intelligent Measurement Device

7.1 Introduction

Energy harvesting from human motion has been an area of interest for many years, and for many different purposes [45, 52, 56]. Mateu has studied the application of human energy harvesting to power microsensors using many different excitation sources, including simple vibration and temperature variation [42, 40]. Mateu also describes a piezoelectric system designed to be inserted into a shoe [41]. Beeby describes a relatively simple design that takes up very little space (volume of 0.15 cm^3) and uses low ambient vibration levels to harvest energy [5]. Such a design comes very close to the needs described in this chapter. The motivation for this particular study focuses on the athlete. Utilizing the large amount of energy an athlete expends can result in many benefits, as shown in the next few sections.

Many products have been marketed towards athletes for use in a typical workout scenario. In general, the main purpose of these products is to help power a timing or monitoring device (such as a watch that gives workout time and heart rate). However,

they are rarely solely powered by the energy harvesting devices, still relying on a battery to function. For the specific purpose shown in the next section, the desire is to create a device that is powered entirely by human motion.

Athletes who do running events such as a 5K or triathlons are given the option of receiving an official time from the race organizers. This is almost always accomplished by a simple timing chip. The two general forms these take are a circular, battery-powered chip (which often requires a strap to attach to the body) or a rectangular RFID chip that can be looped through shoelaces, both of which are shown in Fig. 7.1. These devices simply send out a signal when they interact with a magnetic field, which is created by mats located at the beginning and end of the race, as shown in Fig. 7.2. In this scenario, the only information given by the timing chips is overall race time. In addition, the mats can be very expensive and the chips require battery replacement relatively often. One of the goals of this study is to create a device that not only is powered entirely by the athlete, but that gives far more information than total race time.

There are currently devices that use GPS to track the displacement and speed of the athlete. They are, however, very expensive, dependent on satellite signal quality, and require battery power. They will therefore most likely never be used on a wide scale in any race. The last goal of this study is for the device to be able to give the same information to the athlete in a much more user-friendly, less expensive form using a simple energy harvesting design.

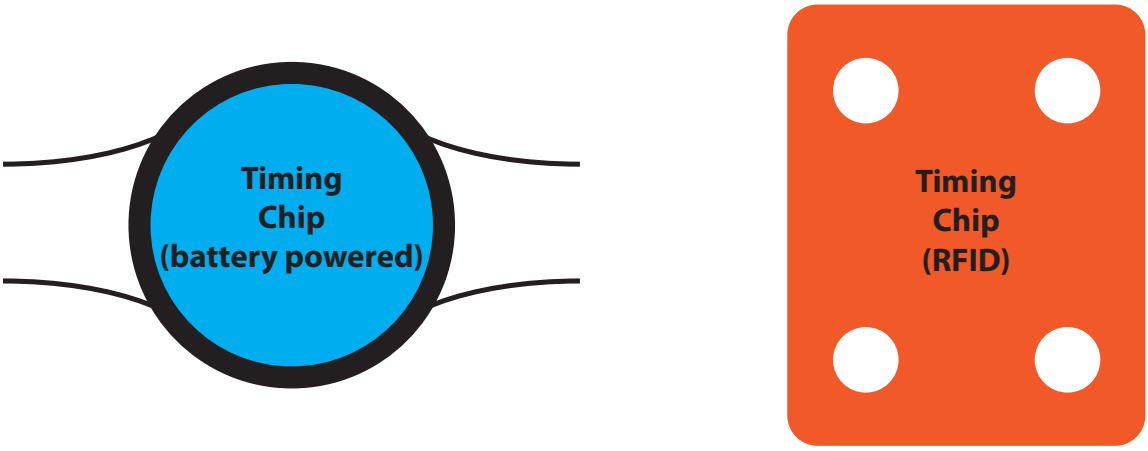

FIGURE 7.1: Two most common examples of timing chips. Includes a battery-powered and RFID chip.

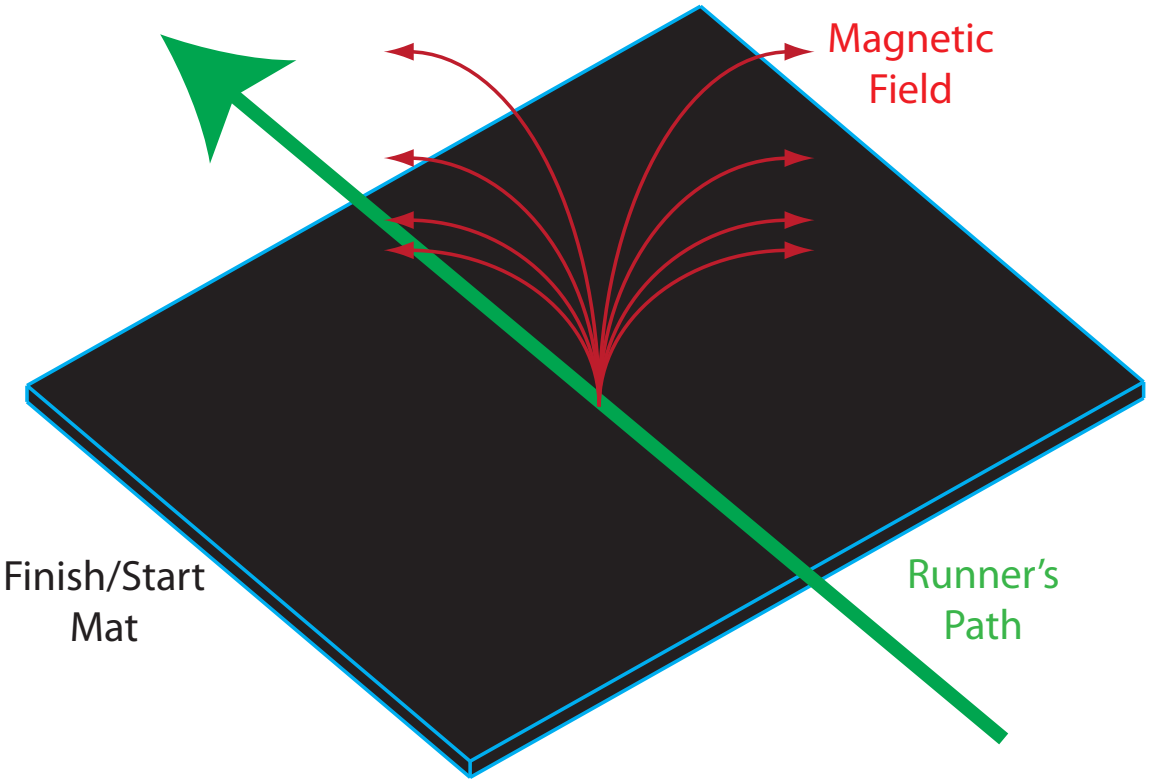

FIGURE 7.2: Running mat that is commonly used in running events. The magnetic field created by the mat interacts with the timing chip in order to register an athlete's start and finish time.

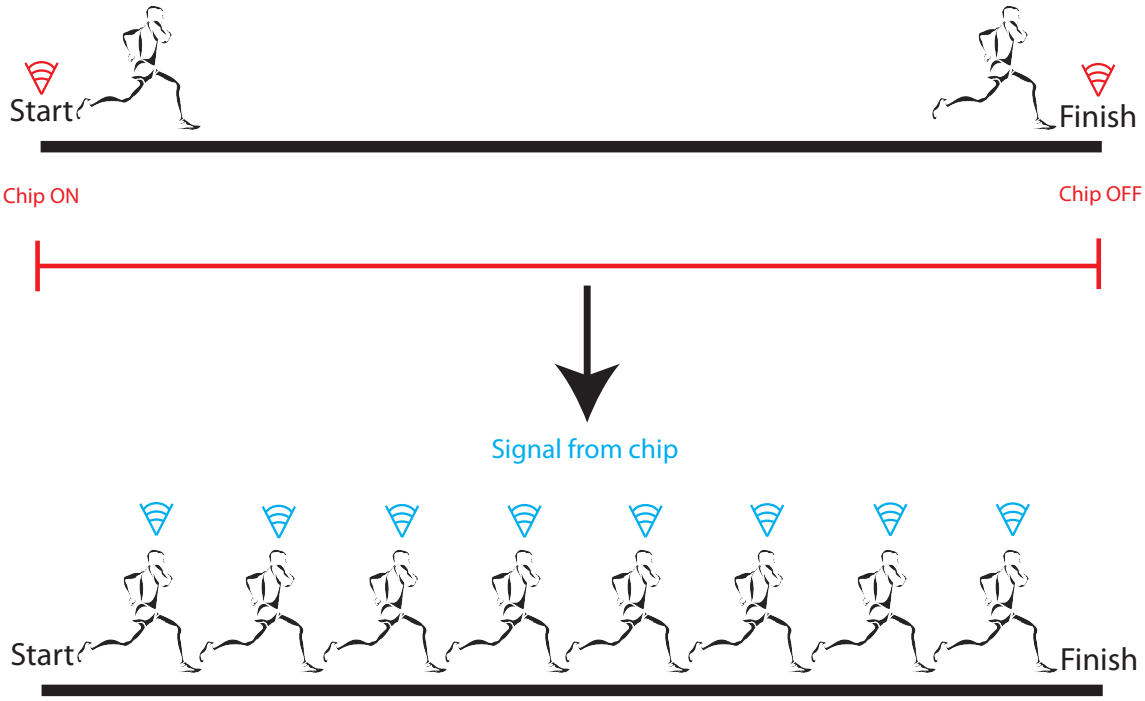

FIGURE 7.3: Potential improvement for timing chips, showing the change from only knowing start/finish time to being able to frequently update the runner's info.

7.2 Dynamics of the Athlete

In order to know the maximum power gained from the athlete, the dynamics of his/her motion must be known. This section describes the motion of an athlete in a running scenario. The data is found by again implementing image processing software, which also gives a beneficial visual representation of the athlete's motion.

7.2.1 Experimental Processes

As opposed to traditional methods of obtaining the dynamics of a system, such as accelerometers, all of the experimental data was found by again using ProAnalyst. This section describes the motion found for a runner.

7.2.2 A Runner

In many previous studies of human motion, inverse dynamics was used to determine the motion attributes. An example of this process for human motion can be seen in [47]. Here, a person walked on a contact plate that determined the ground reaction forces. From this, a link model was used to calculate the corresponding forces and motions up through the leg to the rest of the body. This process can be fairly accurate, but still requires making certain simplifying assumptions, such as viewing human limbs as a link model. Figure 7.4 shows an example diagram of how the forces and accelerations are determined with inverse dynamics.

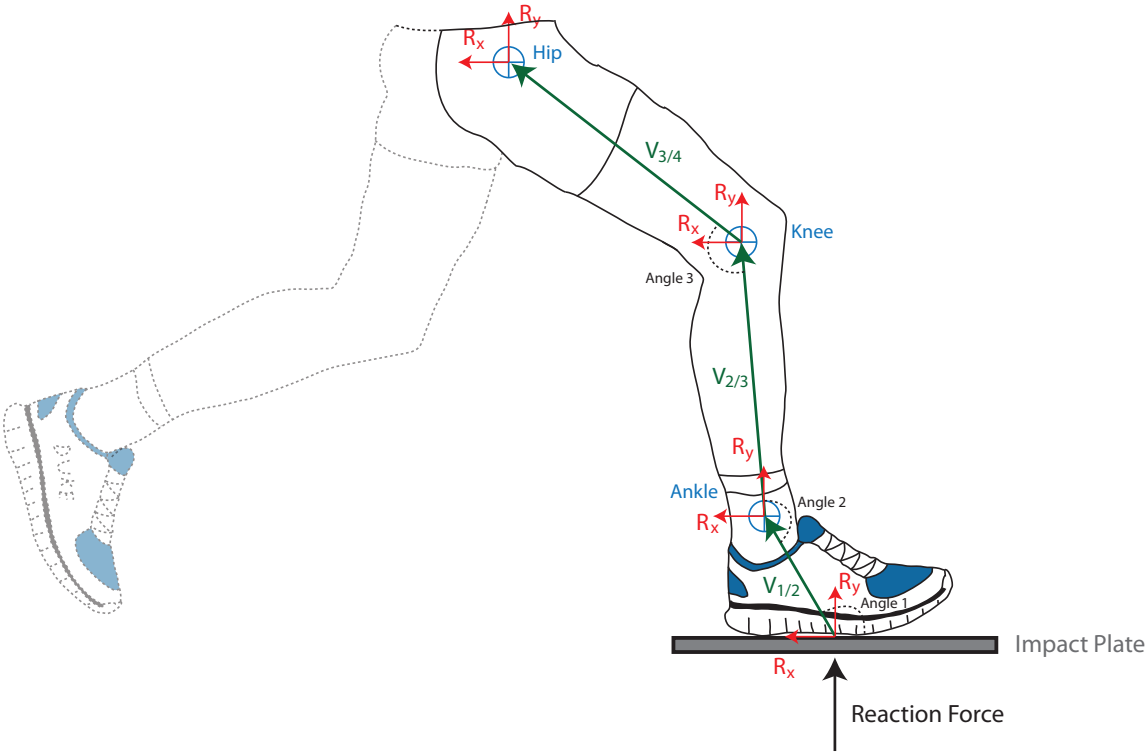

FIGURE 7.4: Example of how inverse dynamics determines forces and accelerations at different body parts by using an impact plate and assuming a link model.

Another common process for determining human motion is image processing. With this, it's simple to track a specific point or points on the body by using some type of marker to distinguish the point from the background. For this study, image

processing is implemented to obtain the dynamics, with an example shown in Fig. 7.5.

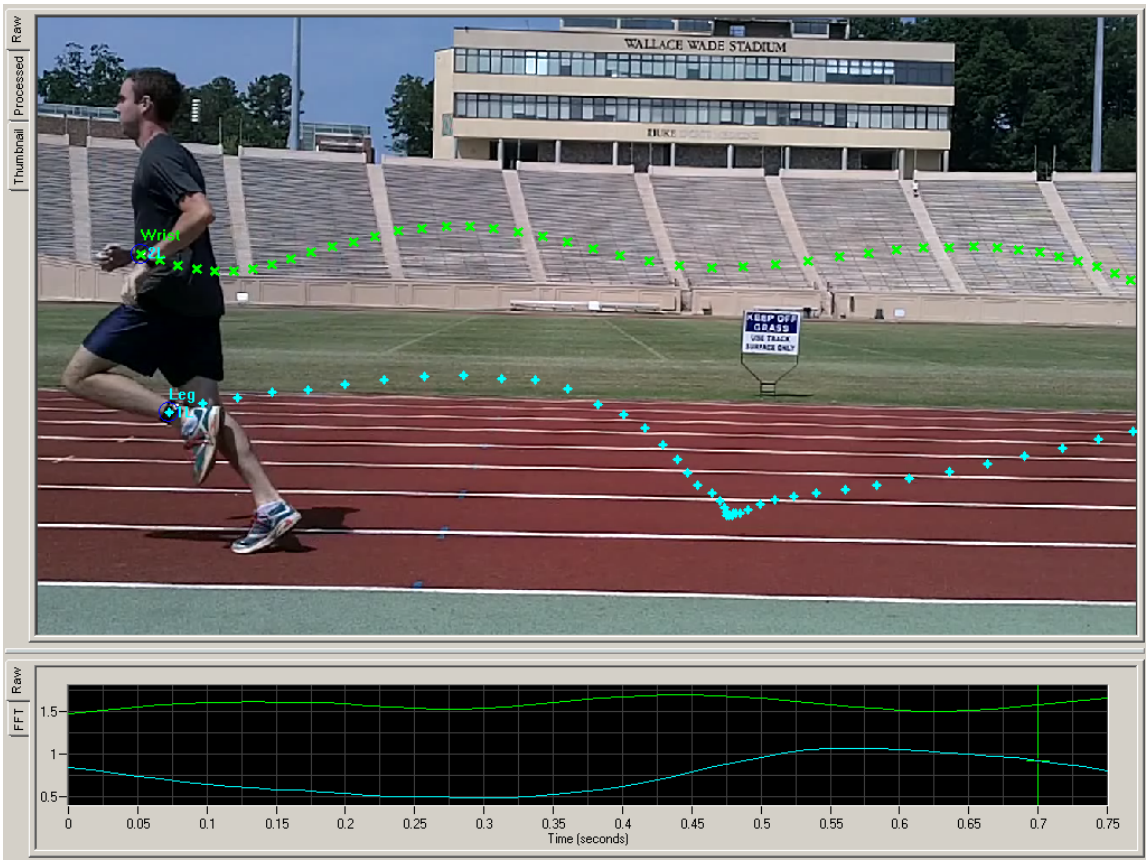

FIGURE 7.5: Runner 1: Example snapshot of how image processing software is used to obtain data.

Filming the runner on the track, as shown in this figure, is not ideal. Unless a track for the camera that moves with the runner is used, sufficient data cannot be obtained. Though it slightly changes the running motion, data in this study was taken from each runner on a treadmill. This allows for sufficient data and knowledge of the exact running speed with very little change in the runner's motion. An example of this is shown in Fig. 7.6.

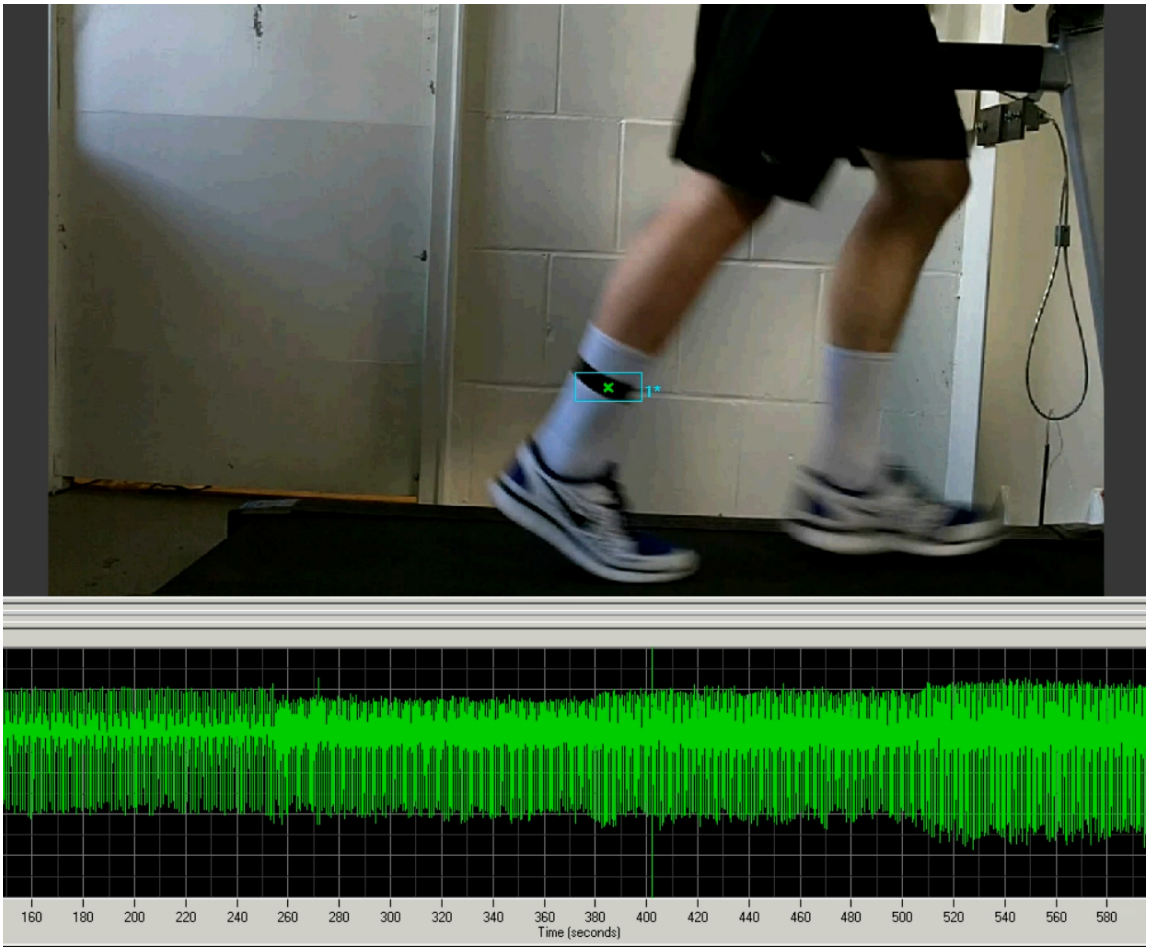

FIGURE 7.6: Runner 2: Example snapshot of image processing software for a runner on the treadmill.

Maximizing Potential Power

The paper by Niu [47] also gives data for multiple body parts, including the ankle, knee and hip. They determined the available power at each body part by using inverse dynamics, as described earlier. Figure 7.7 shows some of the results from the Niu paper. This figure shows that the most available power occurs at the ankle. Therefore, for the purposes of this study where the goal is to harvest to greatest amount of energy from human motion, only the dynamics of the ankle are studied.

Joint/Motion	Work [J/step]	Power [W]	Max moment [Nm]	Negative work [%]
Heel Strike	1 (1-5)	2 (2-20)		
Ankle	34.9 (33.4)	69.8 (66.8)	~140	42 (28.3)
Knee	24.7 (18.2)	49.5 (36.4)	~40	85.2 (92)
Hip	19.6 (18.96)	39.2 (38)	~40	11.5(19)
Elbow	1.07	2.1	1-2	37
Shoulder	1.1	2.2	1-2	61
Center of Mass	0.5	1		

FIGURE 7.7: Taken from [47], gives the experimentally determined available power for different parts of the body while walking, where the ankle is shown to have the highest amount of available power.

Results

Data was taken for multiple subjects running at speeds varying from 0.89-3.98 m/s (2-8 MPH). This speed range includes slow walking (30 min. mile, 0.89 m/s) and relatively high speed running (7.5 min. mile, 3.58 m/s), and therefore covers most of the possible motions of the runner. The statistics of each runner can be seen in Fig. 7.8. After obtaining the experimental data using the image processing software, the acceleration profiles for the different runners were compared.

	Runner 1	Runner 2	Runner 3
Gender	Male	Male	Female
Height	6′1″	6′4″	5′6″
Age	24	25	24
Activity Level (1-10)	8	6	7

FIGURE 7.8: Statistics and attributes of the three runners observed in this study. Activity level is an estimate of the relative athletic/workout level of each subject, ranging from sedentary (1) to regular exercise (10).

Figs. 7.9-7.11 show the acceleration characteristics for speeds 0.89-3.13 m/s (2-7 MPH) for runners 1, 2 and 3, respectively. The acceleration profiles for all three runners at walking speeds runners are similar in shape and phase, with runner 3 having higher amplitudes. When changing from walking, runners 1 and 2 maintain their profile similarities, with runner 3 having a slightly different shape. However, it

can be seen from these profiles that for all runners, the accelerations in the horizontal direction are much larger than the vertical accelerations, which intuitively seems obvious. It therefore becomes apparent that from an energy harvesting standpoint, a potential harvester should be designed to operate along the horizontal direction where the accelerations are the largest.

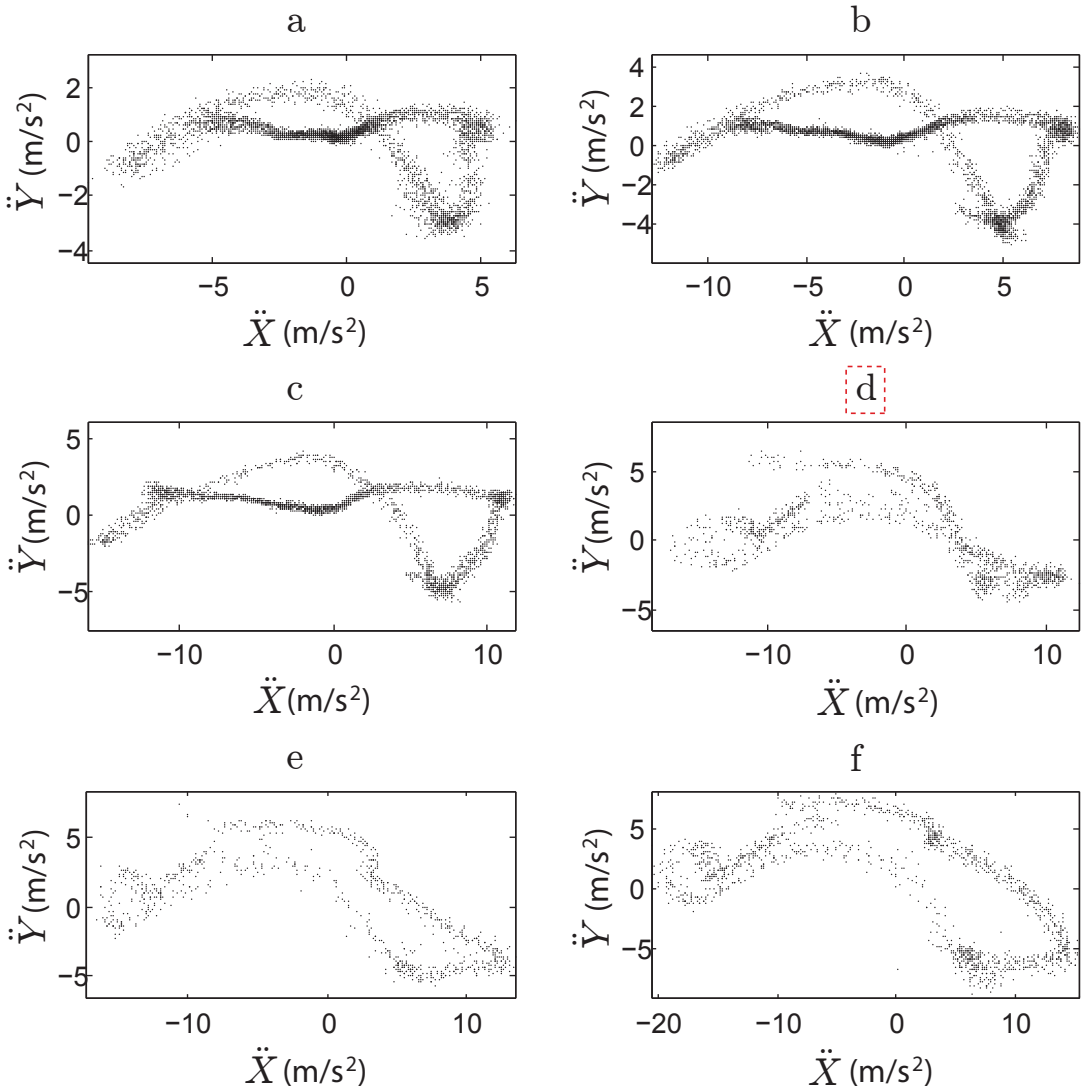

FIGURE 7.9: Runner 1: Second time derivative the configuration space for speeds of 0.89-3.13 m/s (2-7 MPH), with first running speed highlighted. The first four harmonics of the motion are used.

A common shape for a runner's acceleration profile can be seen in Fig. 7.12. Labeled in this figure are the leg positions and corresponding velocities where the vertical and horizontal accelerations reach their maximum and minimum values. Also shown is the direction along this trajectory the accelerations follow throughout a single stride.

Fourier Analysis

Using the data obtained in the previous section, the runners' motions were recreated numerically using Fourier analysis. Though the image processing software gives position data, accelerations are the important values. When the time derivatives are taken for this position data numerically, significant noise is created. Fourier analysis allows for this noise to be filtered out, giving only relevant data. Figs. 7.14-7.17 show the comparison between the original acceleration time series and the recreated time series, the frequency spectrum, and the second derivative of the configuration space for particular runners and speeds. Common among these figures is a large response at the first harmonic, the largest accelerations in the horizontal direction, as well as a relatively sharp decrease in magnitude after the fourth or fifth harmonic.

For runners 1 and 2, the majority of the available power is located within a 2 Hz range for the entire range of speeds 0.89-3.98 m/s (2-8 MPH), as shown in Figs. 7.18-7.21. Though the motion of runner 3 is more spread out over the frequency spectrum, a relatively large percentage of power is still available in the same 3-4 Hz range. This is good news as far as energy harvesting is concerned, since the harvester can operate at a high efficiency while having a relatively small bandwidth.

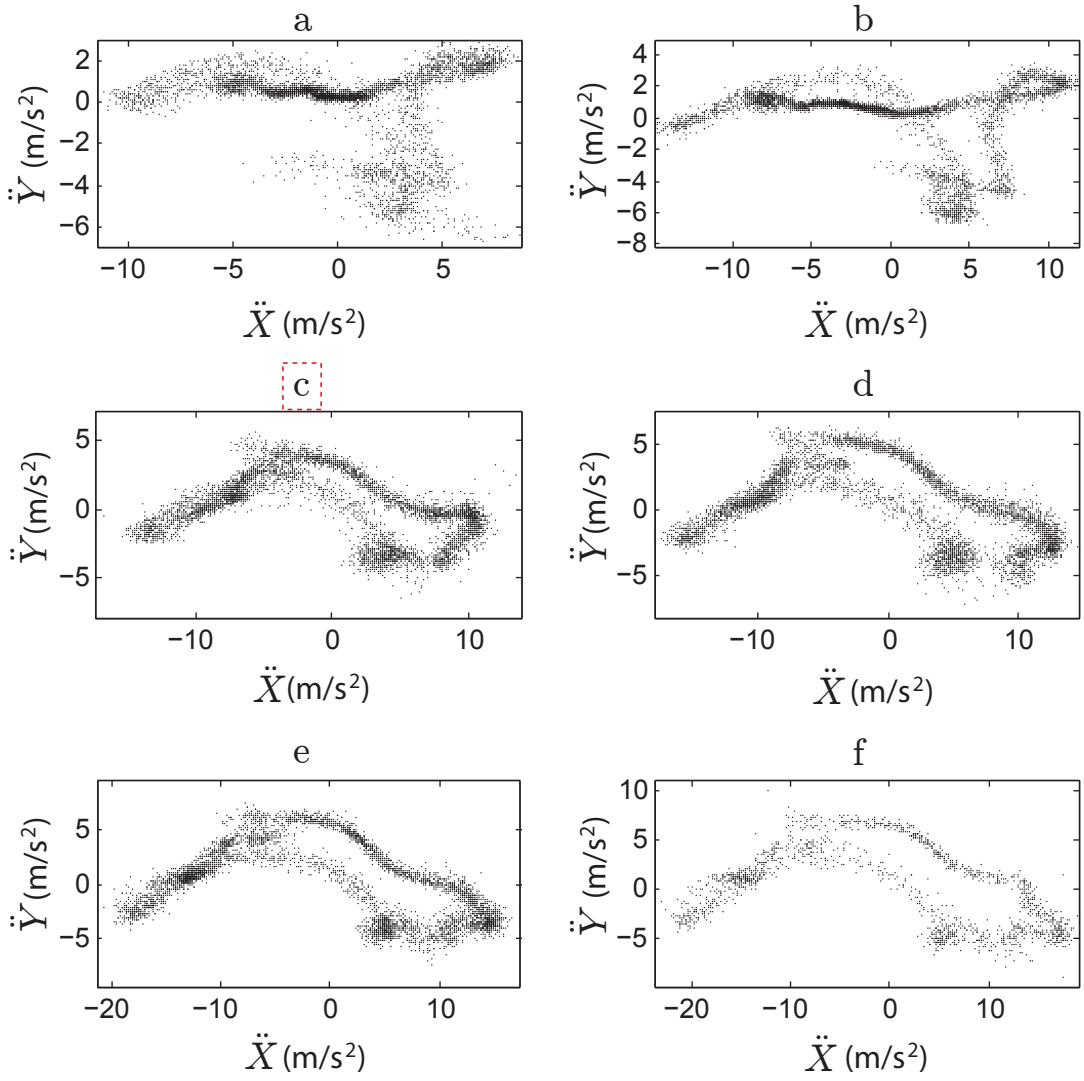

FIGURE 7.10: Runner 2: Second time derivative the configuration space for speeds of 0.89-3.13 m/s (2-7 MPH), with first running speed highlighted. The first four harmonics of the motion are used

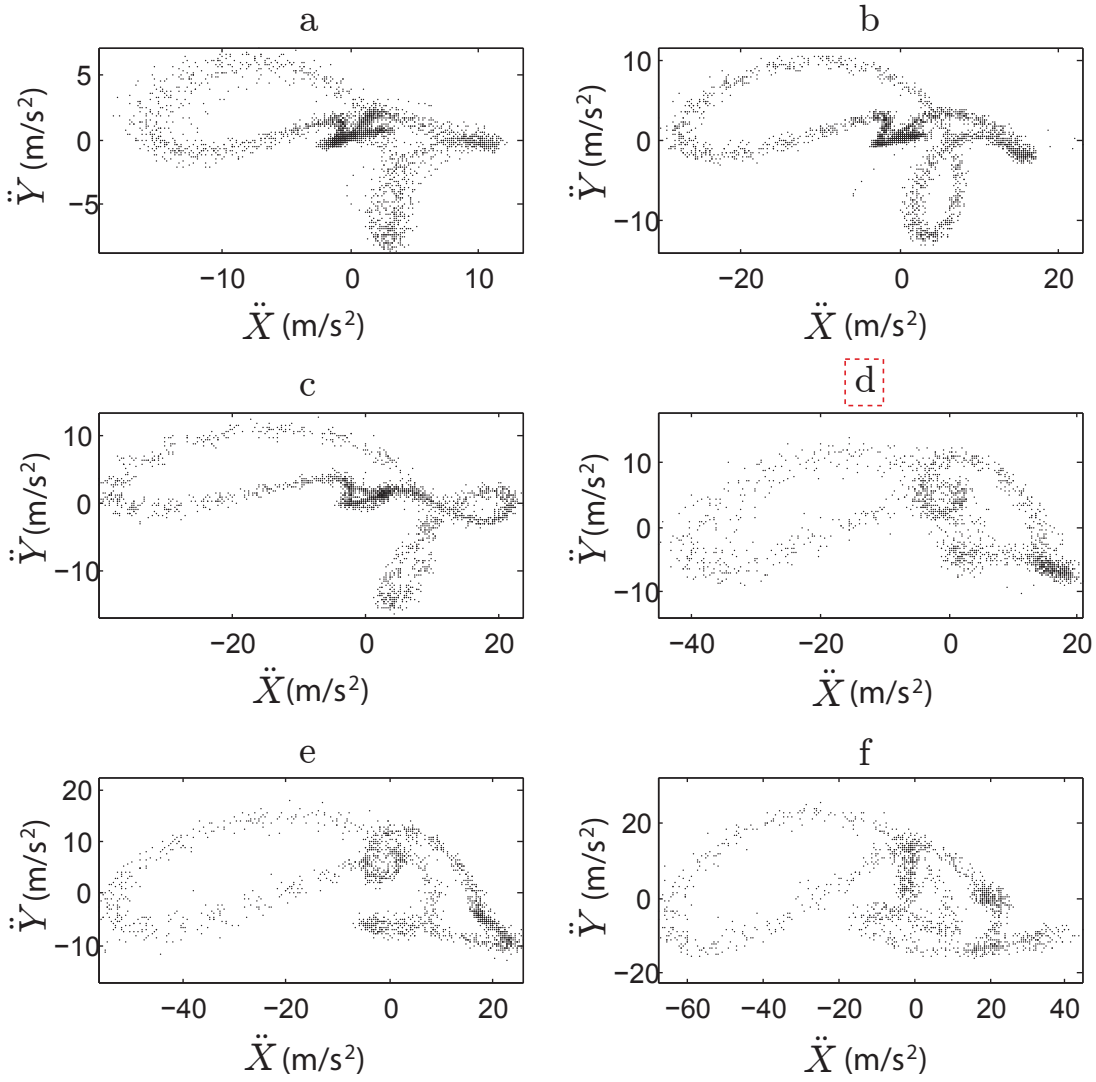

FIGURE 7.11: Runner 3: Second time derivative the configuration space for speeds of 0.89-3.13 m/s (2-7 MPH), with first running speed highlighted. The first four harmonics of the motion are used

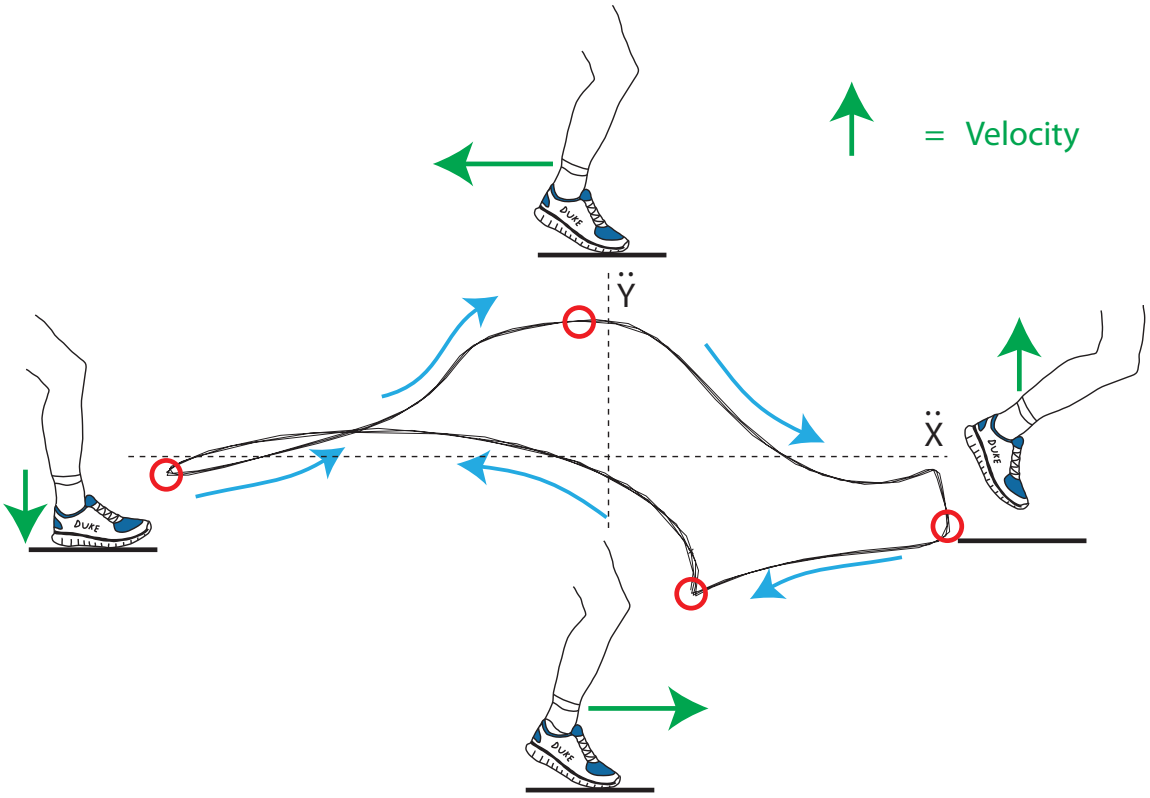

FIGURE 7.12: General acceleration profile for a runner. Shown are the four positions where maximum and minimum X and Y accelerations take place.

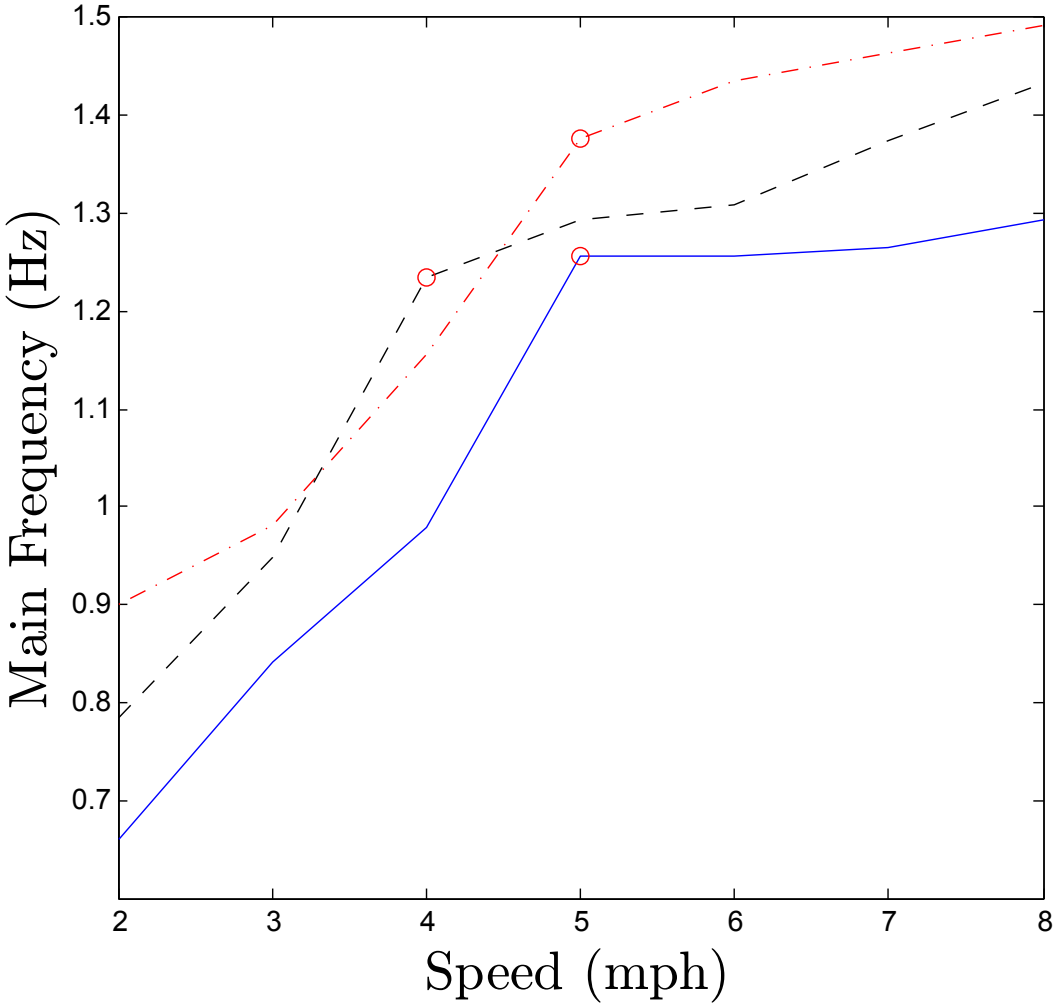

FIGURE 7.13: Runners 1 (black dashed), 2(blue solid), and 3 (red dot-dashed): main frequency as it changes with running speed. Red circle shows where runner changed from walking to running.

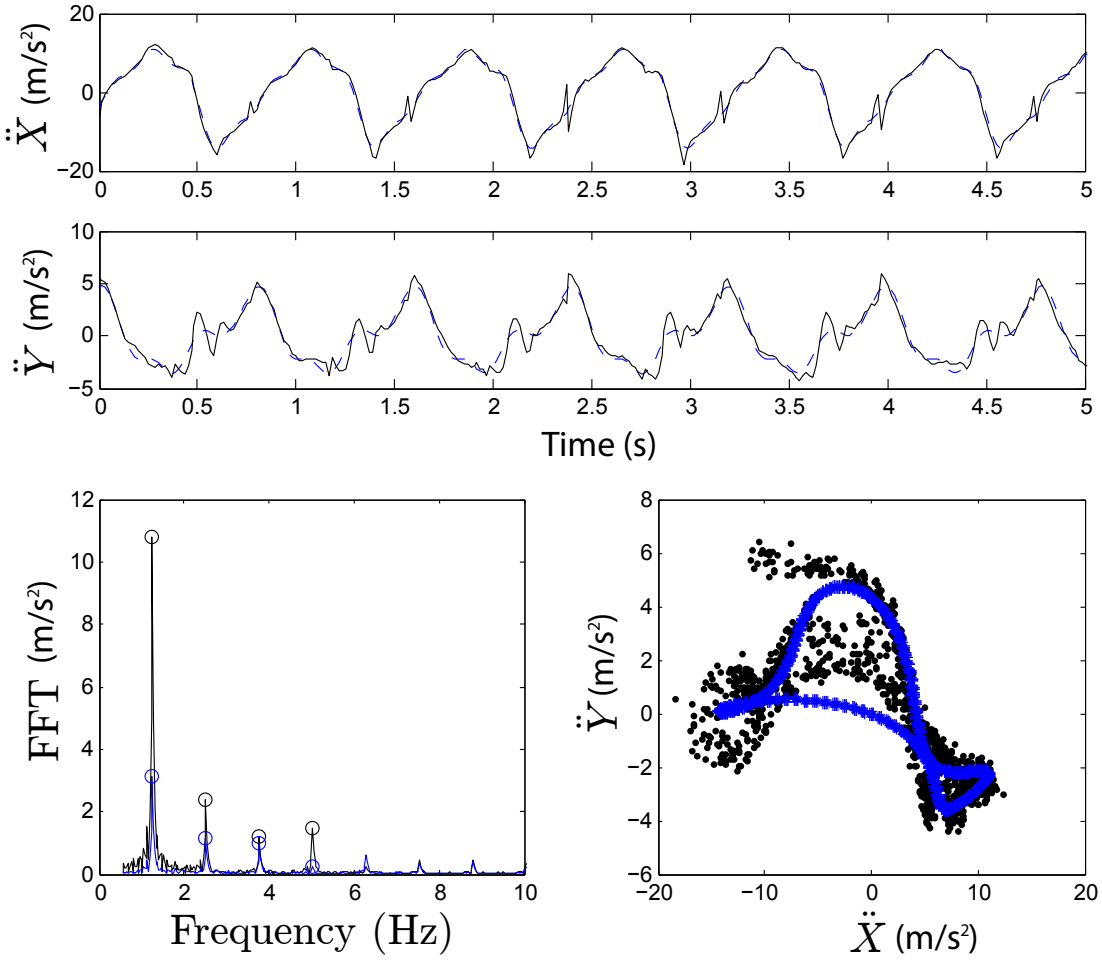

FIGURE 7.14: Runner 1: recreated leg motion for a running speed of 2.24 m/s (5 MPH), the first running speed.

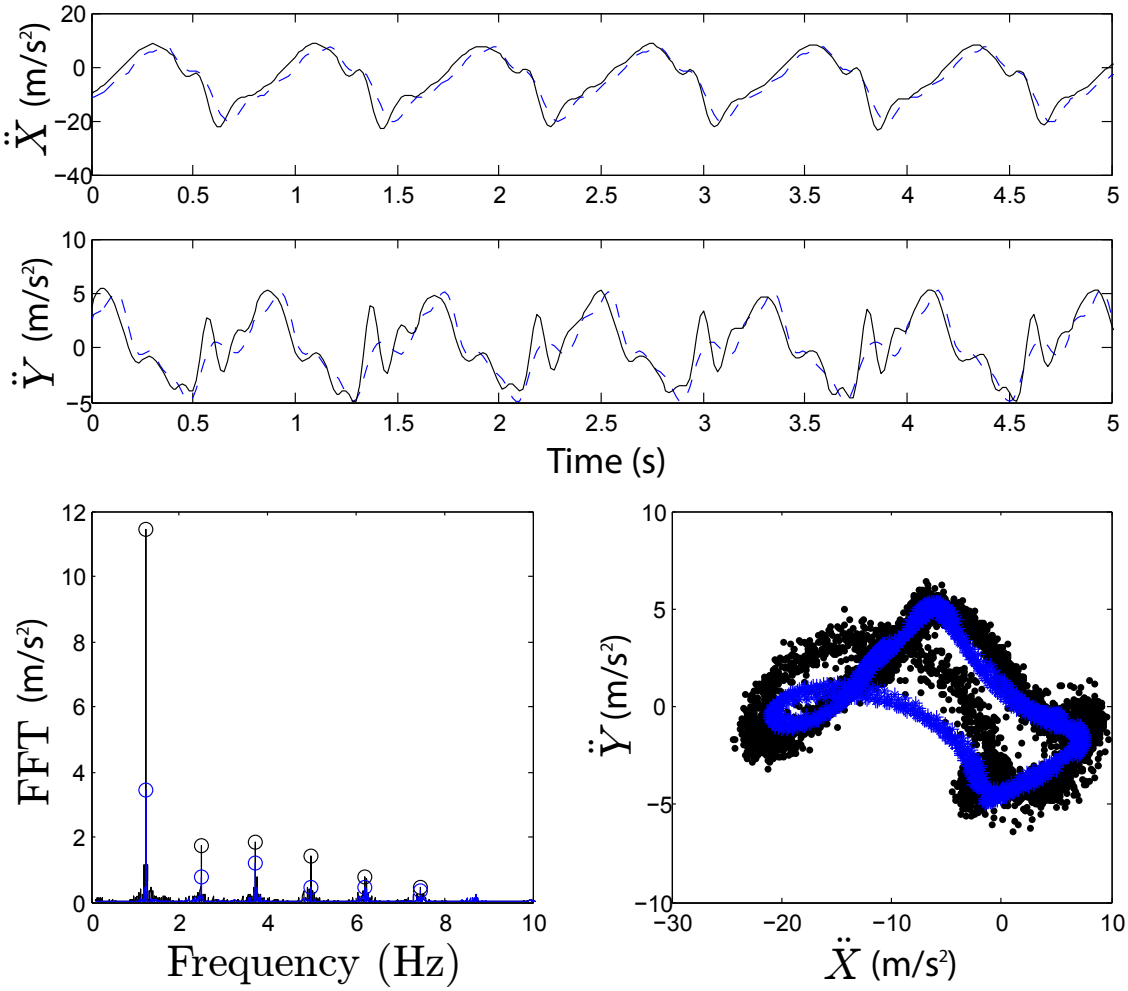

FIGURE 7.15: Runner 2: recreated leg motion for a running speed of 1.79 m/s (4 MPH), the first running speed.

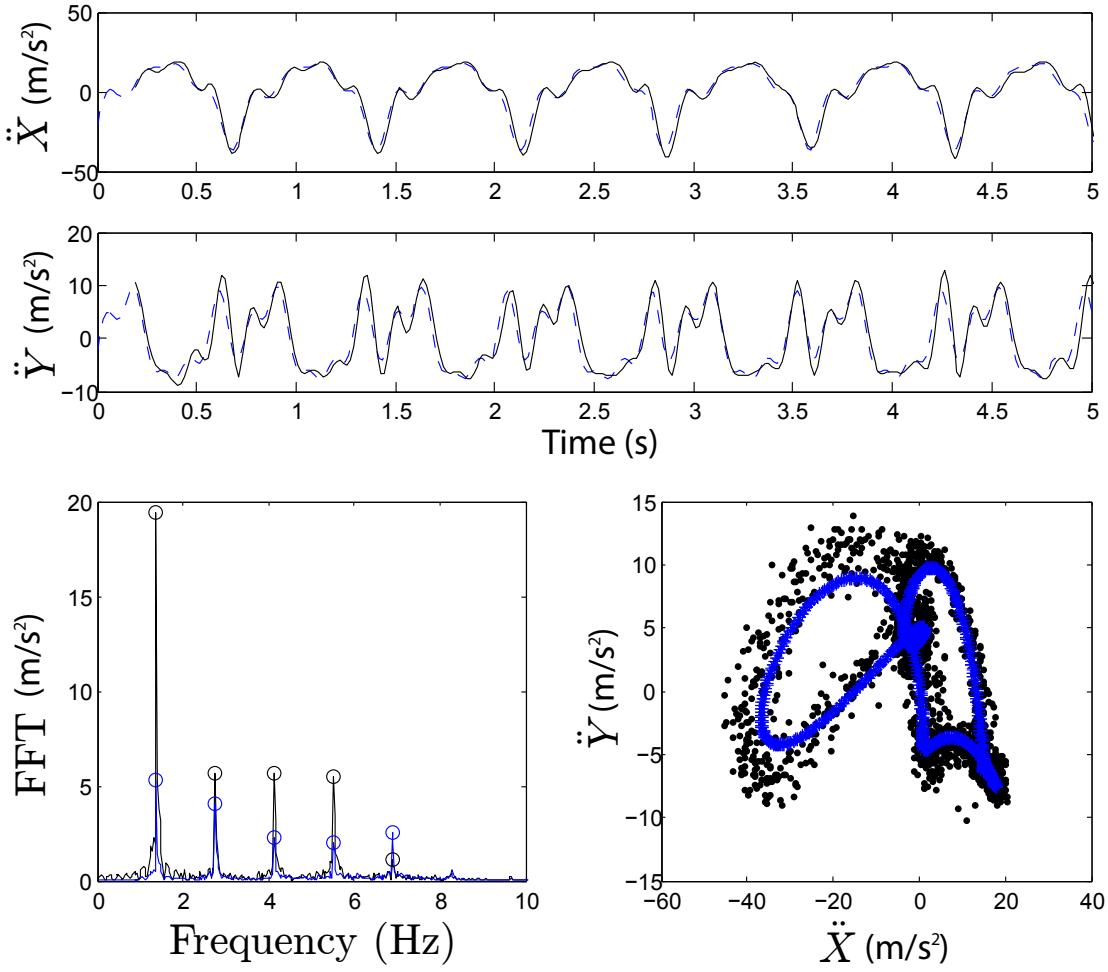

FIGURE 7.16: Runner 3: recreated leg motion for a running speed of 2.24 m/s (5 MPH), the first running speed.

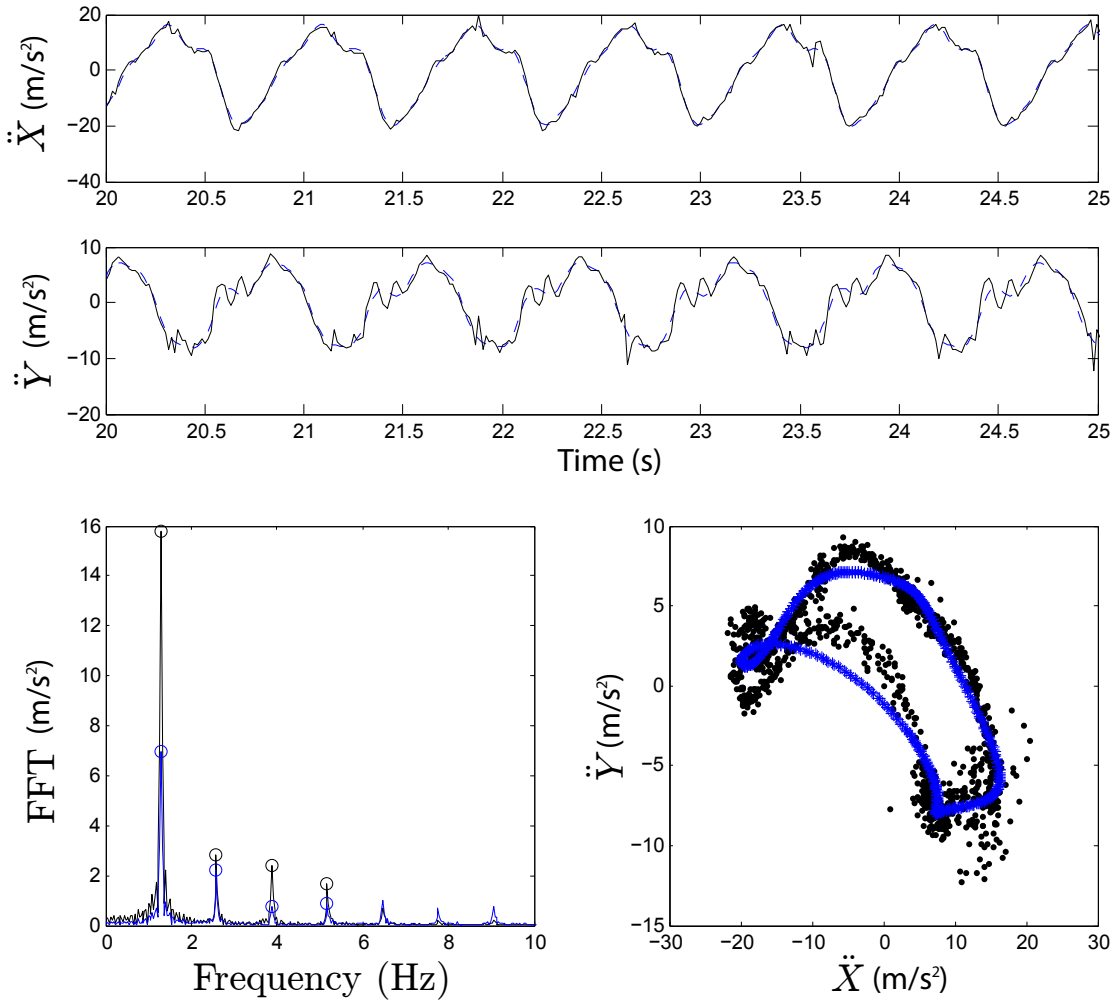

FIGURE 7.17: Runner 1: recreated leg motion for a running speed of 3.58 m/s (8 MPH)

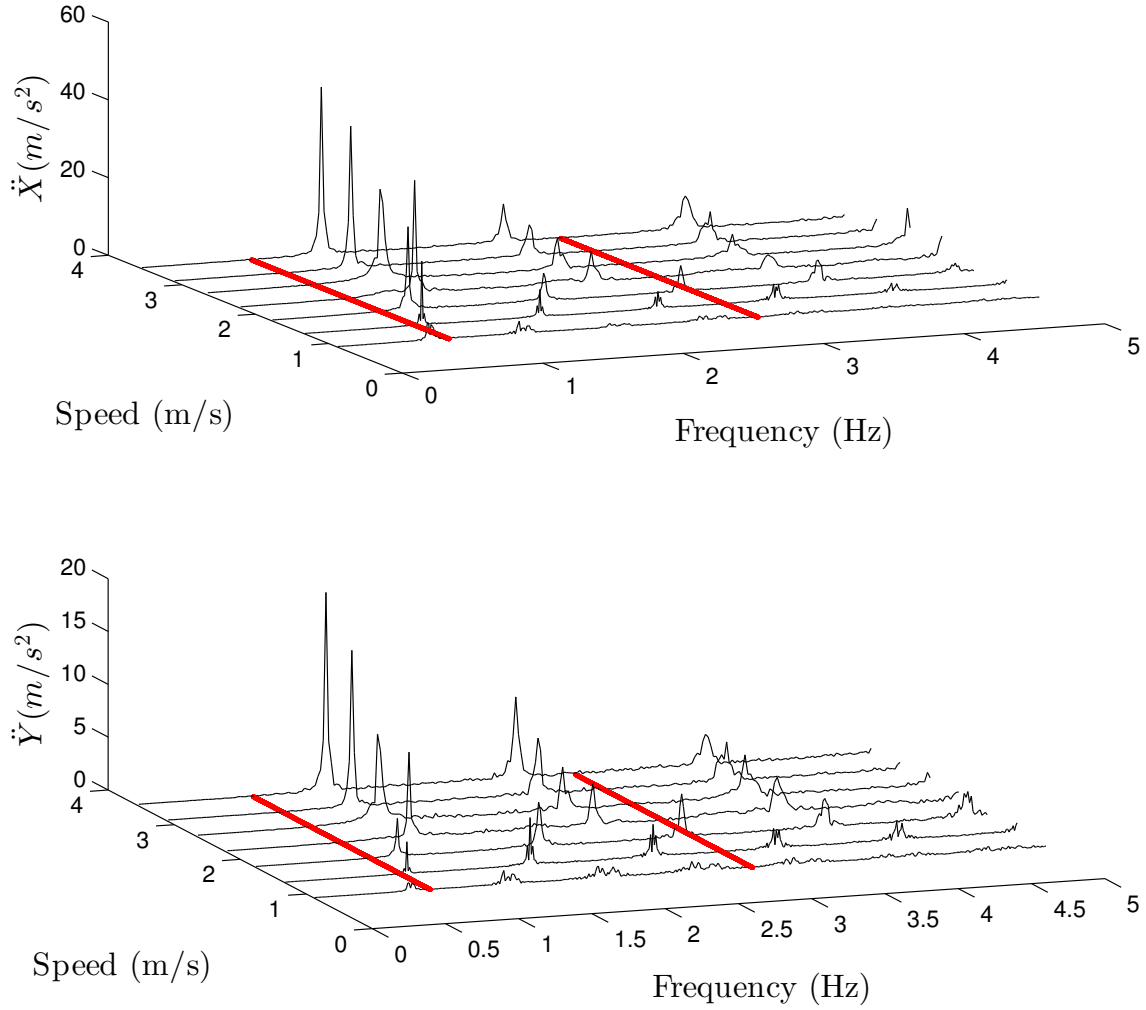

FIGURE 7.18: Runner 1: frequency response including all running speeds from 0.89-3.98 m/s (2-8 MPH), shown in three dimensions. Red lines show that most available energy is between 0.8 and 3 Hz.

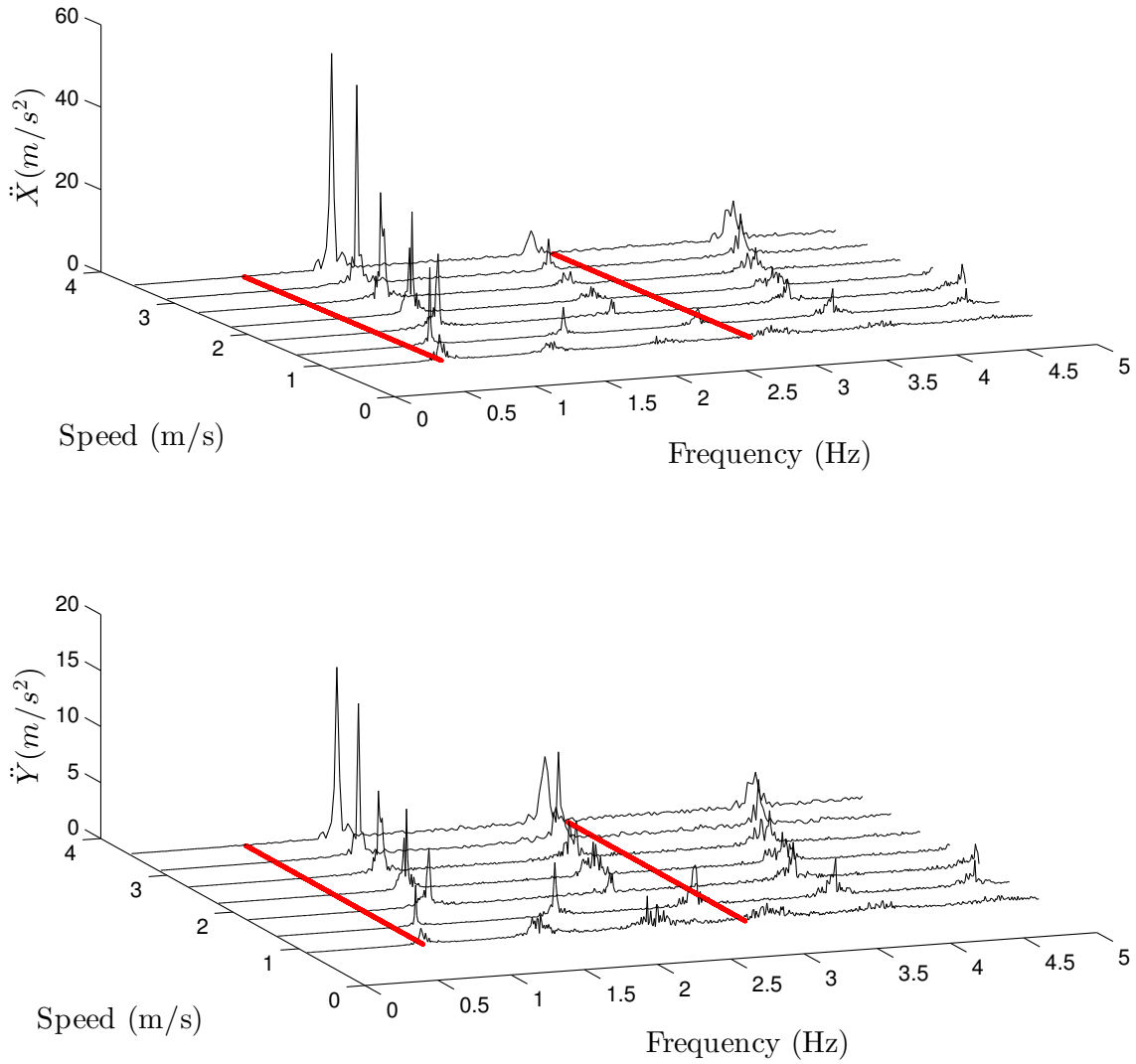

FIGURE 7.19: Runner 2: frequency response including all running speeds from 0.89-3.98 m/s (2-8 MPH), shown in three dimensions. Red lines show that most available energy is between 0.8 and 3 Hz.

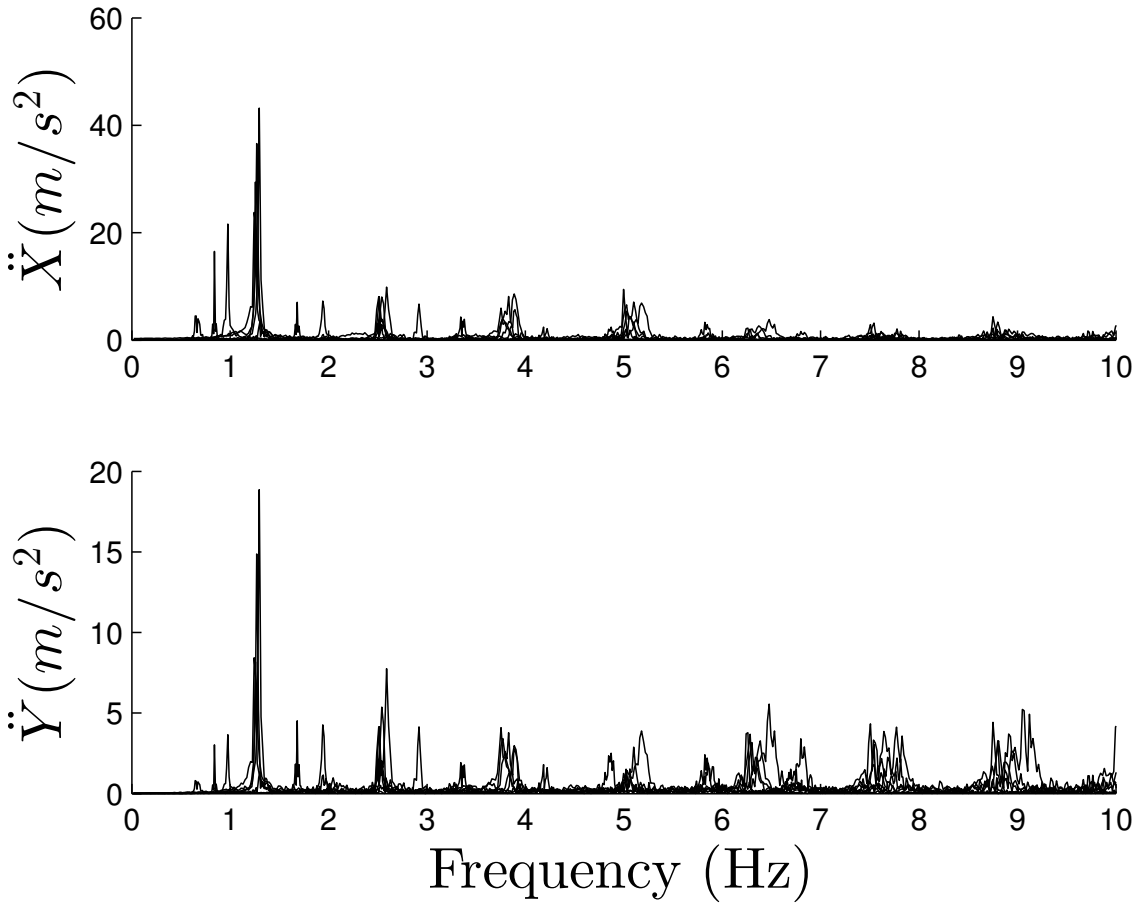

FIGURE 7.20: Runner 1: frequency response including all running speeds from 0.89-3.98 m/s (2-8 MPH). Shows how for this large range of speeds, most of the energy is concentrated in a small range of frequencies.

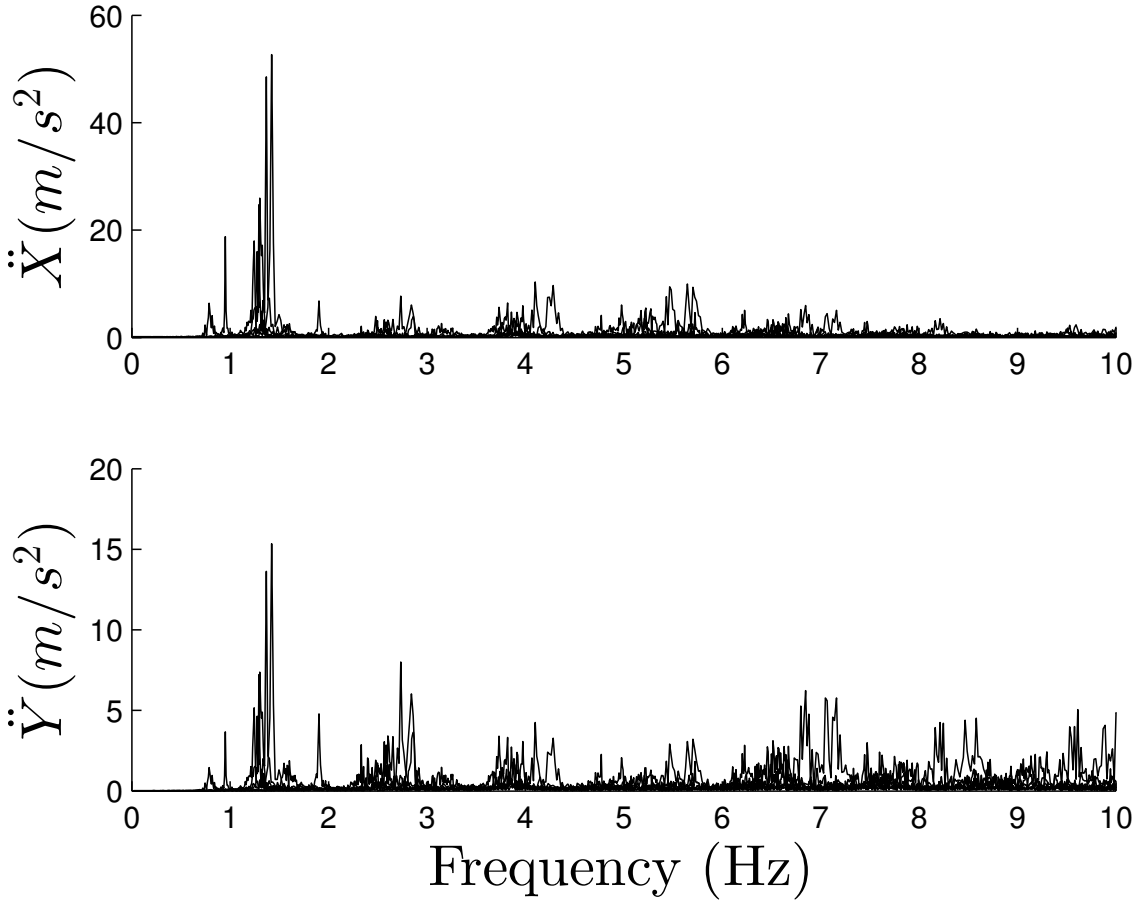

FIGURE 7.21: Runner 2: frequency response including all running speeds from 0.89-3.98 m/s (2-8 MPH).

7.3 Applicable Energy Harvester

Since the prevalent forcing frequencies of human motion are low (< 5 Hz), most of the commonly used energy harvesters are ineffective. For example, while using piezoelectrics on a cantilever beam works well for most vibratory environments, the beam would have to be quite large to have such a low natural frequency. Since our design will be limited in size, this is not a viable option. In addition, since power is, in general, more efficiently transmitted at higher frequencies, the energy harvester design for this particular scenario must be able to convert low frequency energy into more readily usable high frequency energy.

A schematic of the proposed design can be seen in Fig. 7.22. It is a chip where a magnetic ball is allowed to travel along a circular track. When a system of coils is placed in close proximity to the chip, the relative motion of the magnetic ball can induce a current, which is used for energy harvesting.

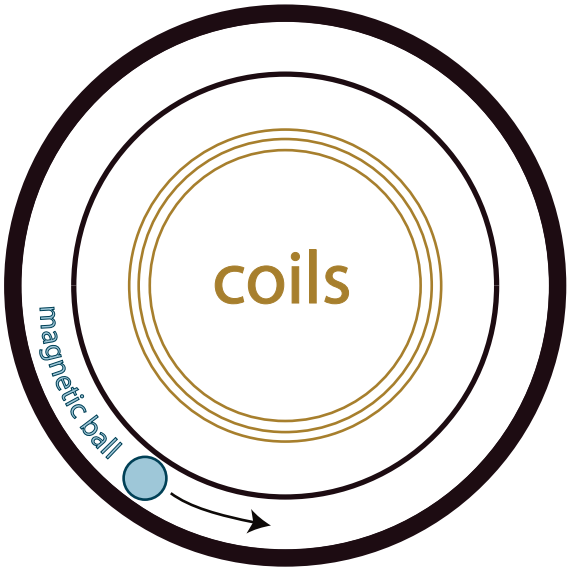

FIGURE 7.22: New, simpler design consisting of a small magnetic ball moving in a circular track around a winding of coils.

To derive the equations of motion for this system, the position vectors are de-

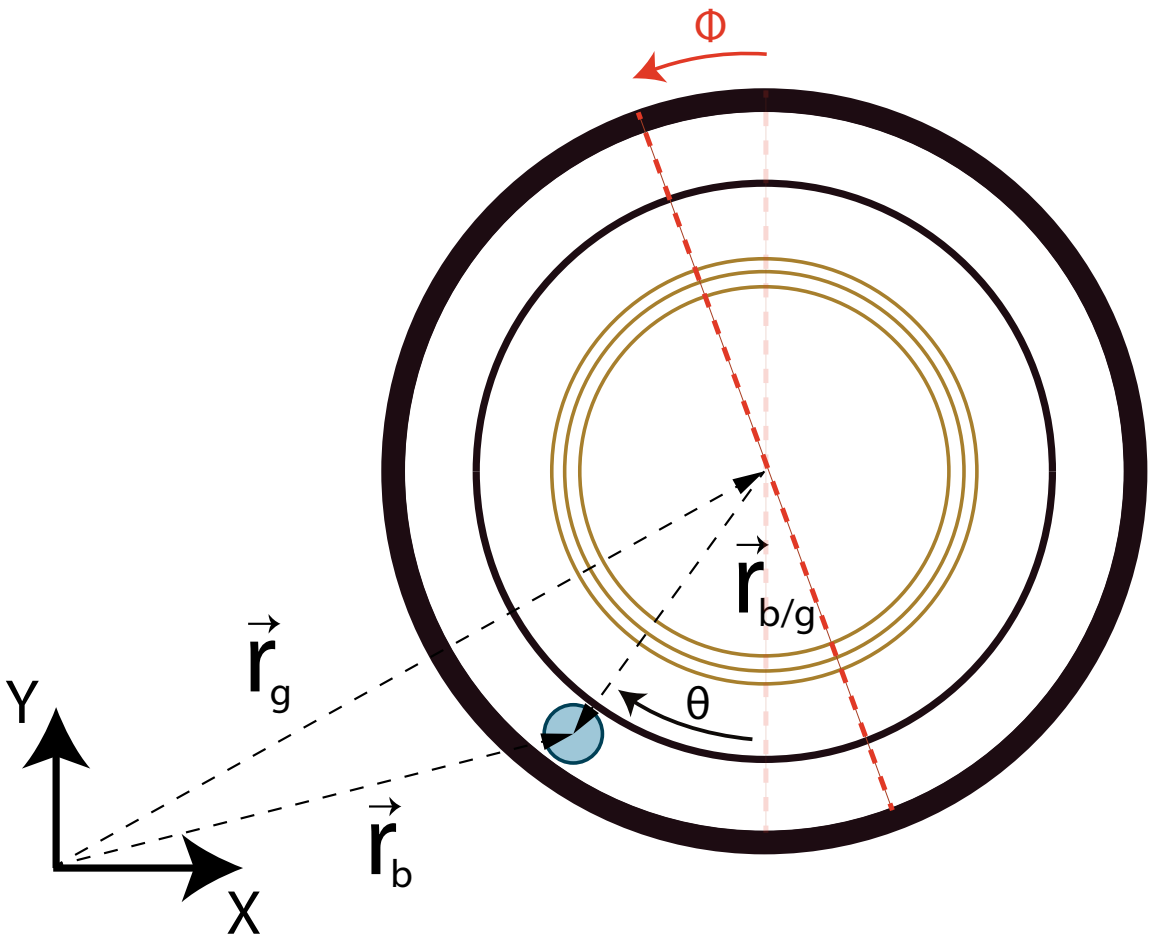

FIGURE 7.23: Harvester design with position vectors.

rived first. The positions and rotation of the chip x, y and ϕ are prescribed values determined from experimental data. Therefore, the equation of motion will only be a function of the variable θ. The position vector to the magnetic ball $\vec{r_b}$ can be written as

$$\vec{r_b} = \vec{r_g} + \vec{r}_{b/g}, \tag{7.1}$$

where these vectors can be seen in Fig. 7.23. The terms on the right hand side of Eqn. 7.1 are

$$\vec{r}_g = \begin{bmatrix} x \\ y \end{bmatrix}, \tag{7.2}$$

$$\vec{r}_{b/g} = \begin{bmatrix} R_m \sin(\theta + \phi) \\ -R_m \cos(\theta + \phi) \end{bmatrix}, \tag{7.3}$$

where R_m is the distance to the middle of the magnetic ball, written as

$$R_m = \frac{R_o + R_i}{2}, \tag{7.4}$$

where R_o and R_i are the outer and inner radius of the chip, respectively. The angles ϕ and θ describe the rotation of the entire chip and the magnetic ball, respectively. It can now be seen that the vector $\vec{r}_b$ becomes

$$\vec{r}_b = \begin{bmatrix} x + R_m \sin(\theta + \phi) \\ y - R_m \cos(\theta + \phi) \end{bmatrix}. \tag{7.5}$$

Taking the time derivative, the total velocity of the ball is found to be

$$\dot{\vec{r}}_b = \begin{bmatrix} \dot{x} + R_m \cos(\theta + \phi)\left(\dot{\theta} + \dot{\phi}\right) \\ \dot{y} + R_m \sin(\theta + \phi)\left(\dot{\theta} + \dot{\phi}\right) \end{bmatrix}. \tag{7.6}$$

From this, the kinetic energy can be written as

$$T = \frac{1}{2} m_b \left(\dot{\vec{r}}_b \cdot \dot{\vec{r}}_b\right). \tag{7.7}$$

The potential energy is simply described as

$$mgy + mgR_m\,(1 - \cos(\theta + \phi)) \tag{7.8}$$

The Lagrangian term becomes

$$L = T - V = \frac{1}{2} m_b \left(\dot{\vec{r}}_b \cdot \dot{\vec{r}}_b \right) - m_b g R_m \ (1 - \cos(\theta + \phi)) \tag{7.9}$$

As done previously, the equation of motion can be found by using Lagrange's equation (2.1). This gives the following equation of motion

$$m R_m \left(R_m \left(\ddot{\theta} + \ddot{\phi} \right) + \ddot{x} \cos(\theta + \phi) + (\ddot{y} + g) \sin(\theta + \phi) \right) = 0 \tag{7.10}$$

Table 7.1 shows the final dimensions for the circular harvester, including the radius of the magnetic ball r_b. These values were chosen by conducting numerical simulations with varying radii to determine which set of values gave the highest possible energy output. A comparison of different radii can be seen in Fig. 7.24.

Table 7.1: Circular Harvester Dimensions

R_o	R_i	r_b
2.5 cm	1.5 cm	0.5 cm

7.3.1 Numerical Simulation

Using the equation of motion given in Eqn. 7.10, the dynamics of the harvester can be simulated with the previously experimentally found human motion as the excitation. The values used can be seen in Table 7.2. Figures 7.27-7.31 show the time series of the velocity of the magnetic ball for multiple running speed excitations. Table 7.3 shows the theoretical max power than can be created by the harvester. This was calculated by using the kinetic energy of the magnetic ball T, as in

$$P_i = \frac{d}{dt}(T) \tag{7.11}$$

where P_i is the instantaneous power and T was given in Eqn. 7.7. These values, of course, are idealized, and are much larger than the actual power that will be harvested

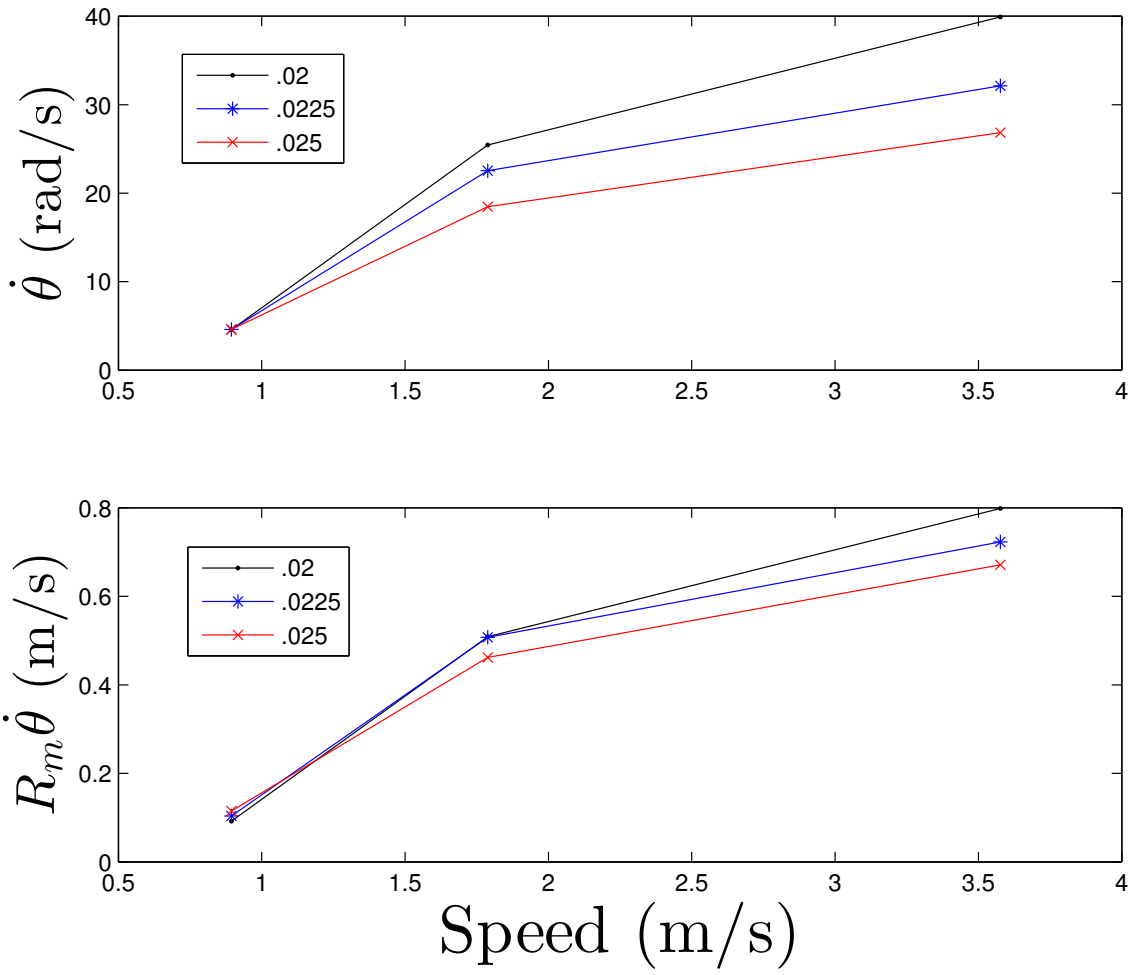

FIGURE 7.24: Comparison of maximum angular and total velocity for varying timing chip radii R_m, with simulations run at speeds of 2, 4, and 8 mph.

through the interaction with the coils. This simplification does, however, allow for a direct comparison between varying chip dimensions and excitation frequencies.

Table 7.2: Runner Excitation Values

Speed (mph)	Freq. (Hz)	Amp. x (m)	Phase x (rad)	Amp. y (m)	Phase y (rad)	ϕ (rad)
2	0.65	0.15	1.74	0.03	-2.34	0.79
4	1.24	0.16	-2.85	0.05	-0.83	1.22
8	1.42	0.2	1.34	0.06	-2.83	1.22

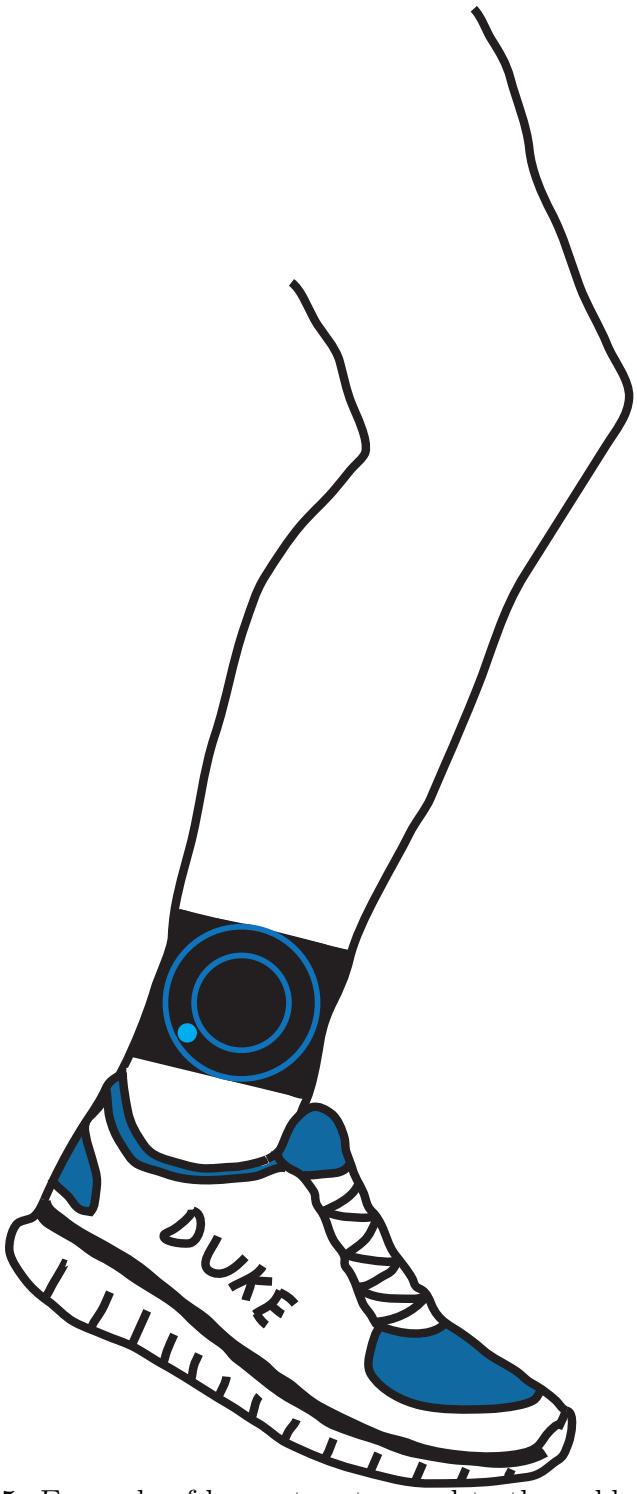

FIGURE 7.25: Example of harvester strapped to the ankle of a runner.

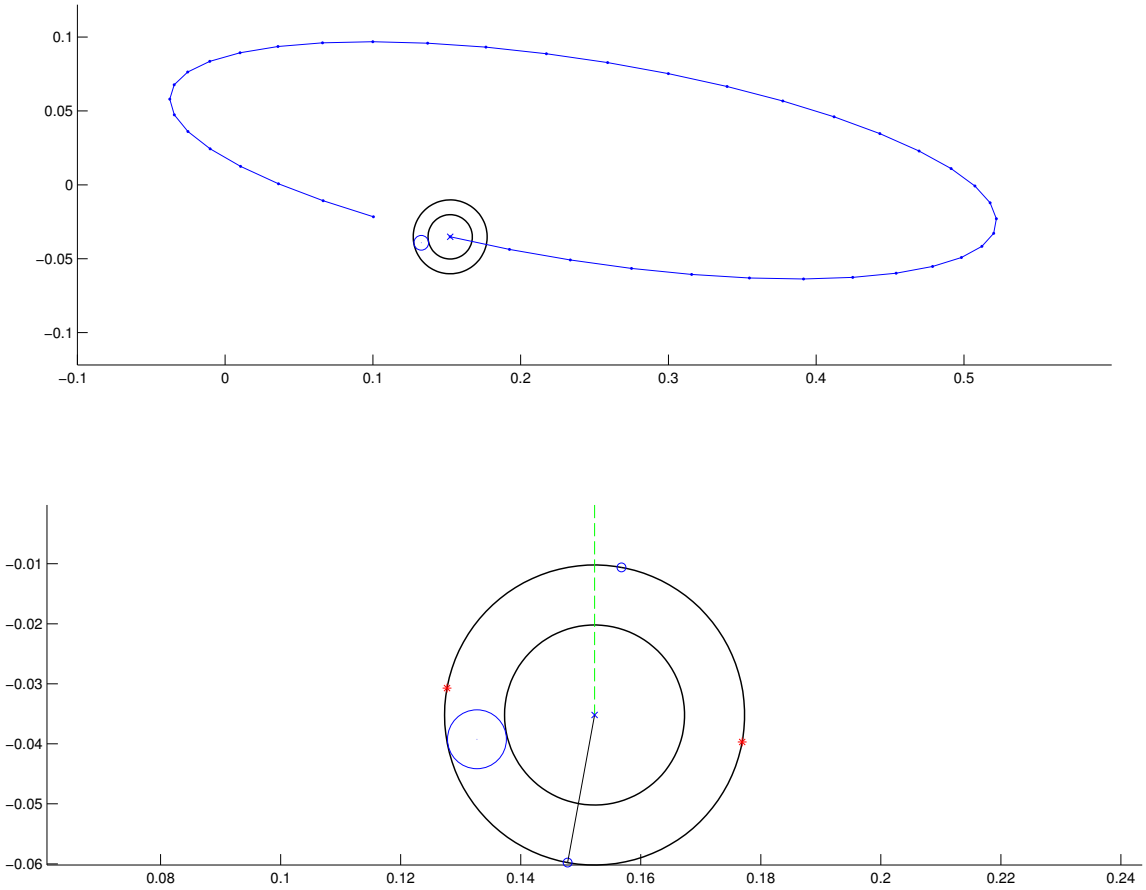

FIGURE 7.26: Screen shot of animation from numerical simulation of the circular energy harvester when excited by human motion.

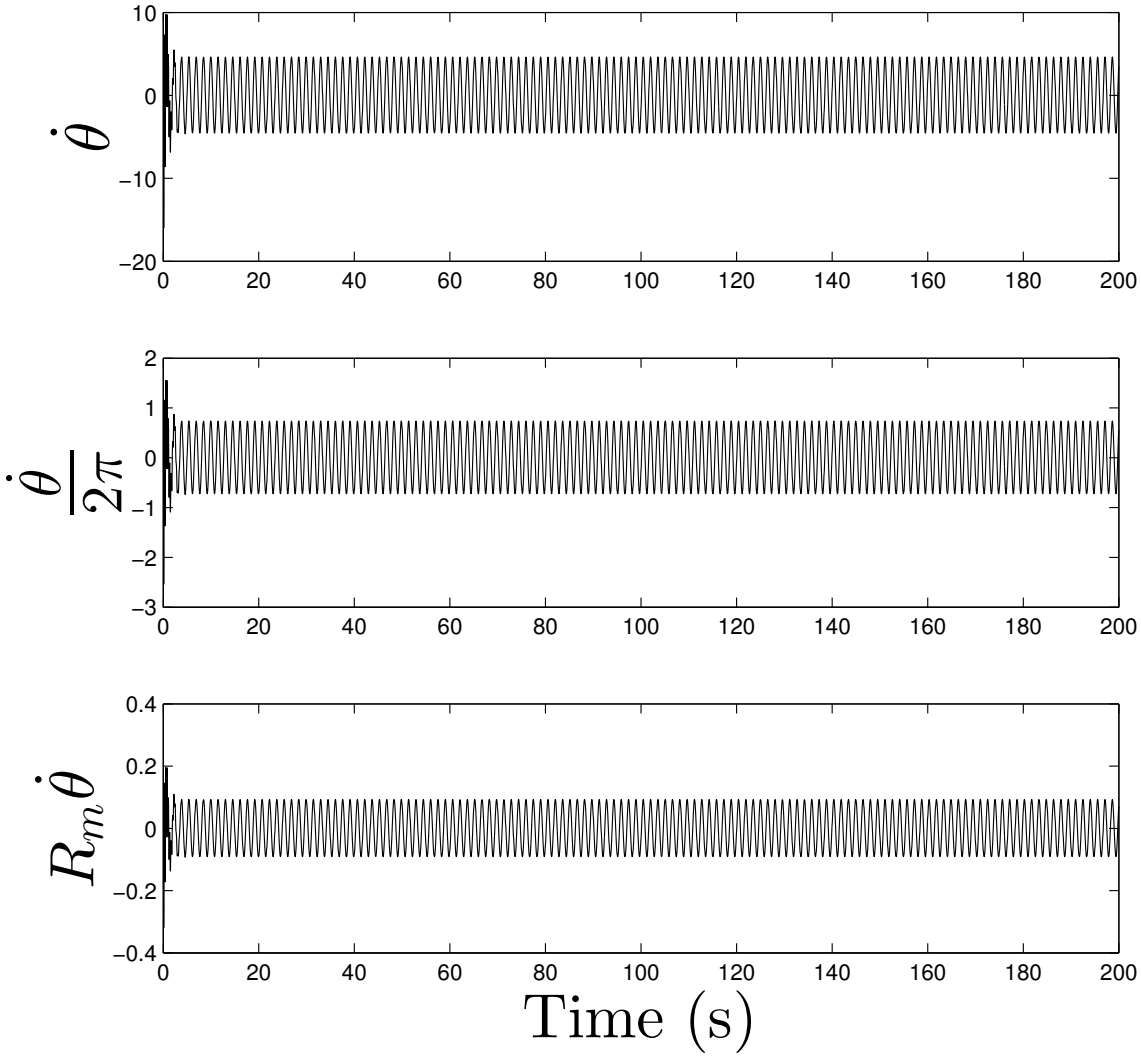

FIGURE 7.27: The simulated velocity of the magnetic ball inside the circular harvester excited by an athlete walking at 2 mph. Shown in terms of [a] angular velocity (radians/second), [b] rotational velocity (rotations/second), and [c] total velocity (meters/second).

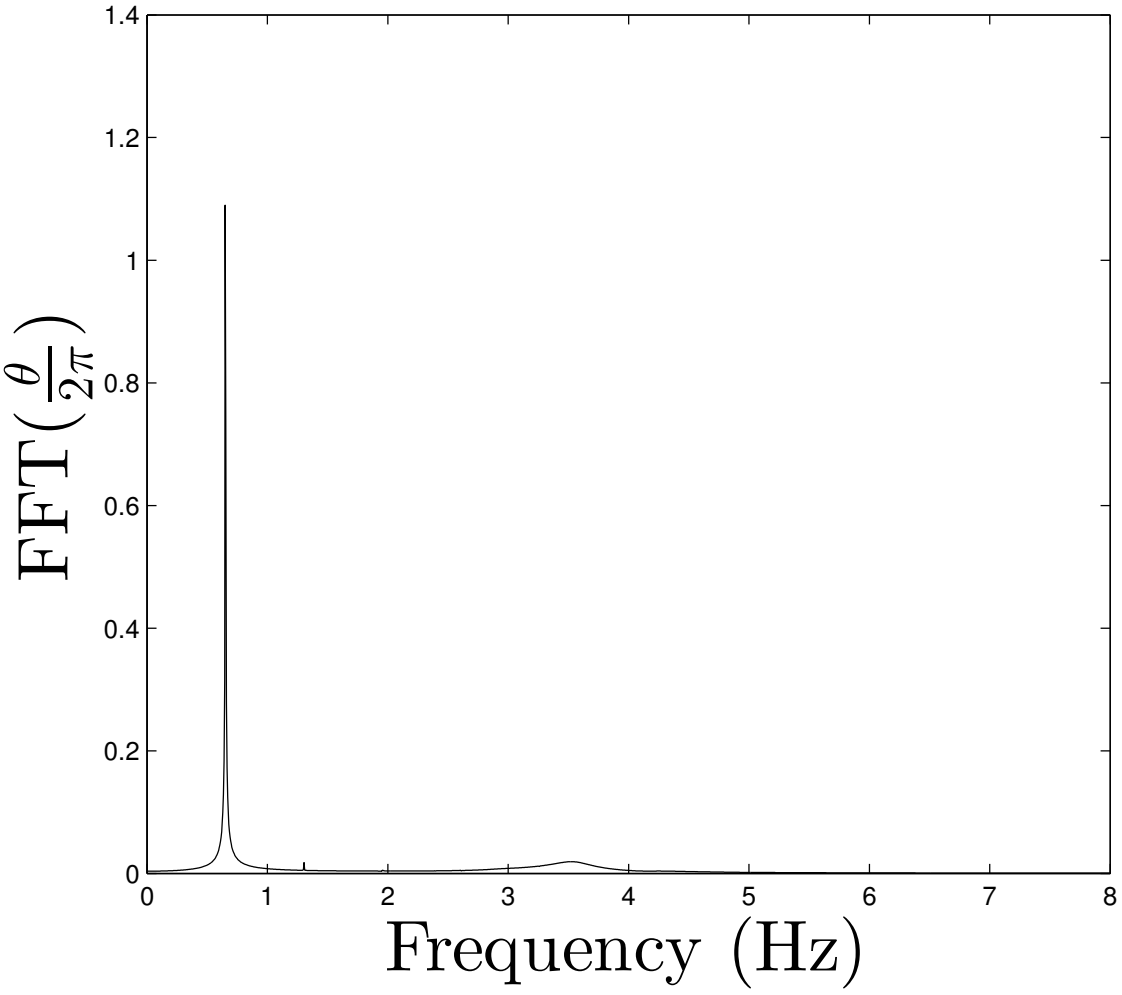

FIGURE 7.28: Frequency response, in terms of rotations per second, for the magnetic ball when excited by the subject walking at 2 mph.

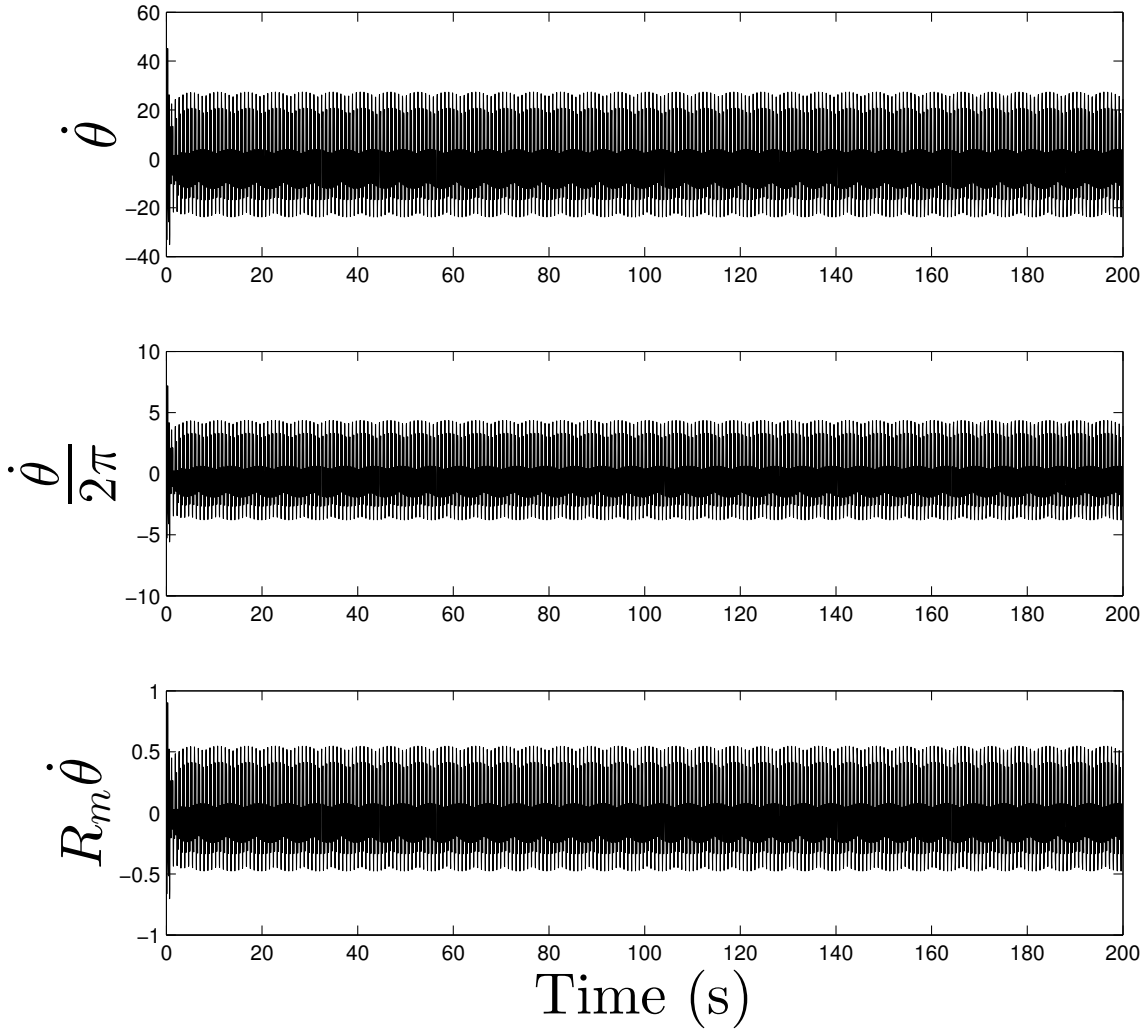

FIGURE 7.29: The simulated velocity of the magnetic ball inside the circular harvester excited by an athlete running at 4 mph. Shown in terms of [a] angular velocity (radians/second), [b] rotational velocity (rotations/second), and [c] total velocity (meters/second).

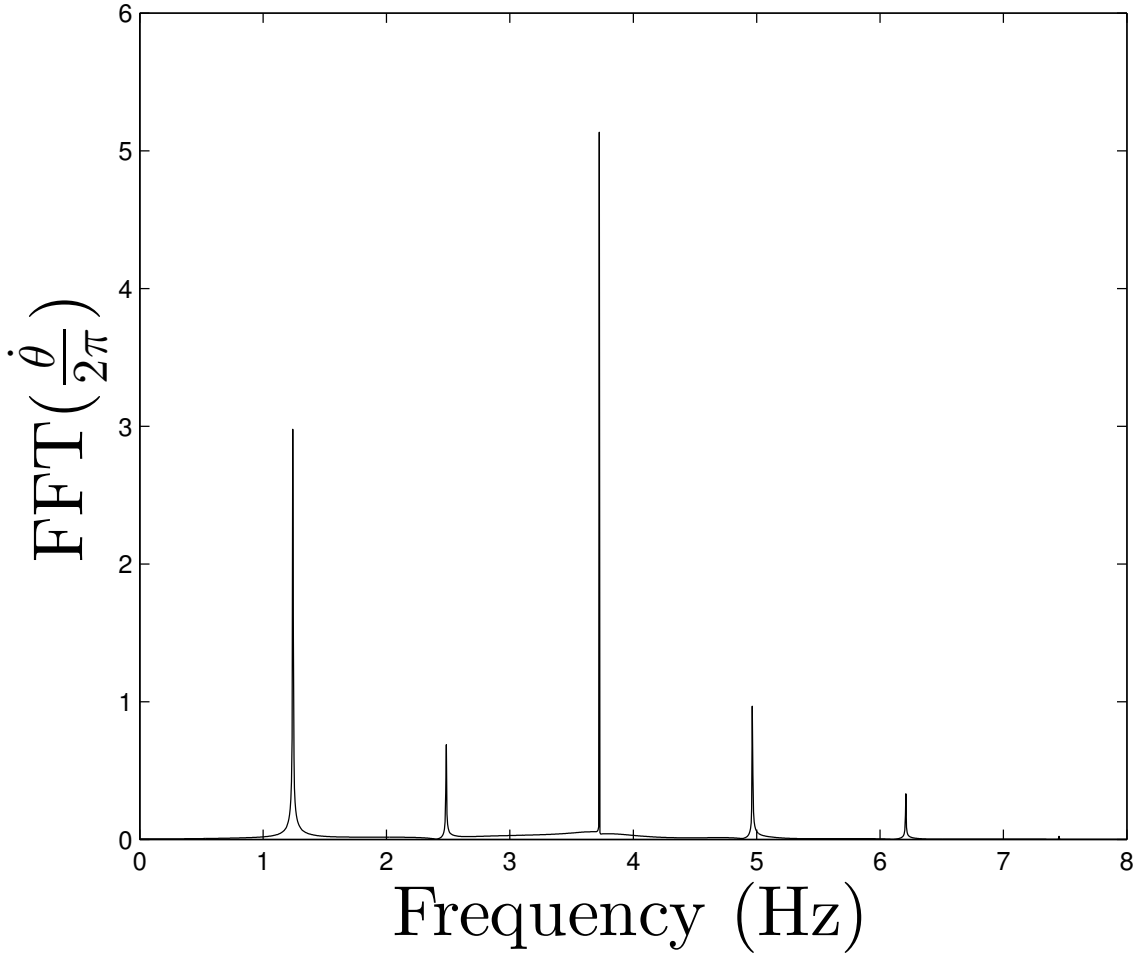

FIGURE 7.30: Frequency response, in terms of rotations per second, for the magnetic ball when excited by the subject running at 4 mph.

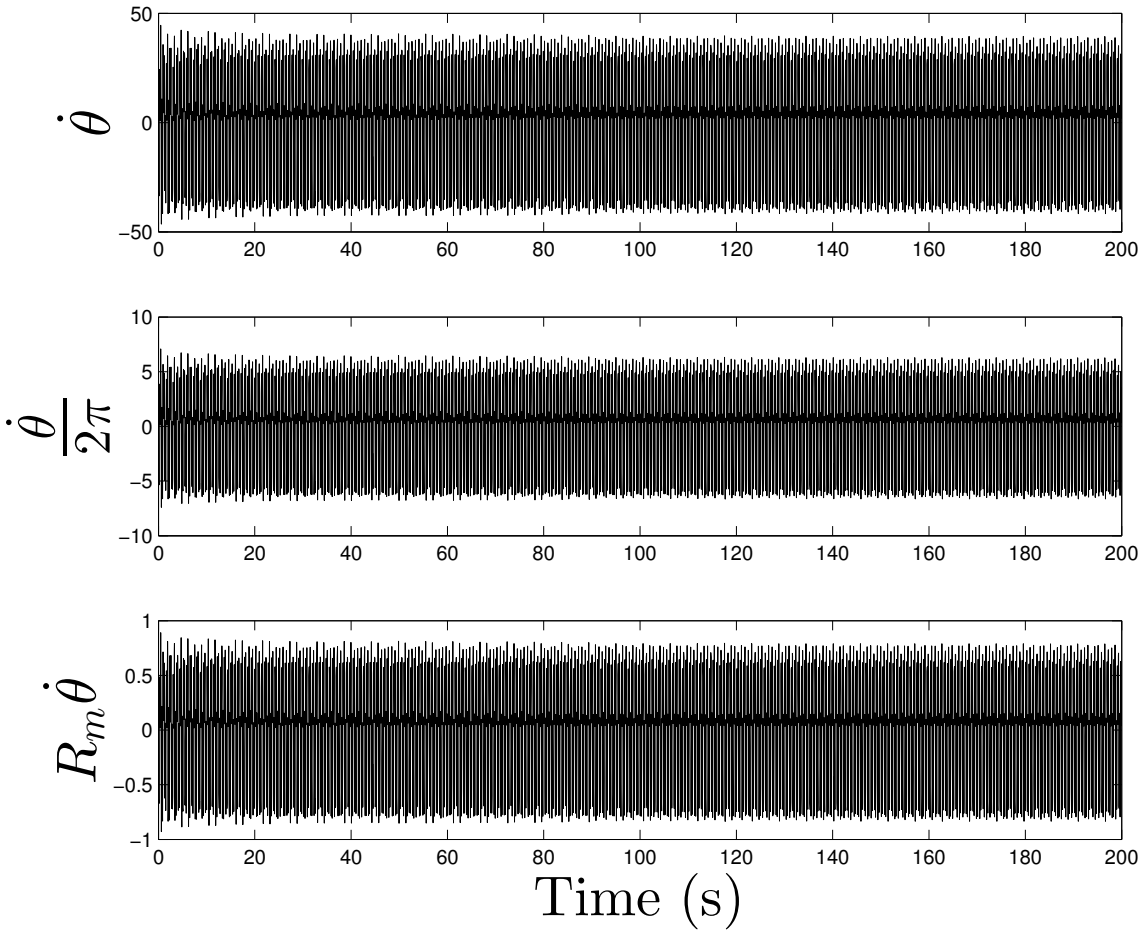

FIGURE 7.31: The simulated velocity of the magnetic ball inside the circular harvester excited by an athlete running at 8 mph. Shown in terms of [a] angular velocity (radians/second), [b] rotational velocity (rotations/second), and [c] total velocity (meters/second).

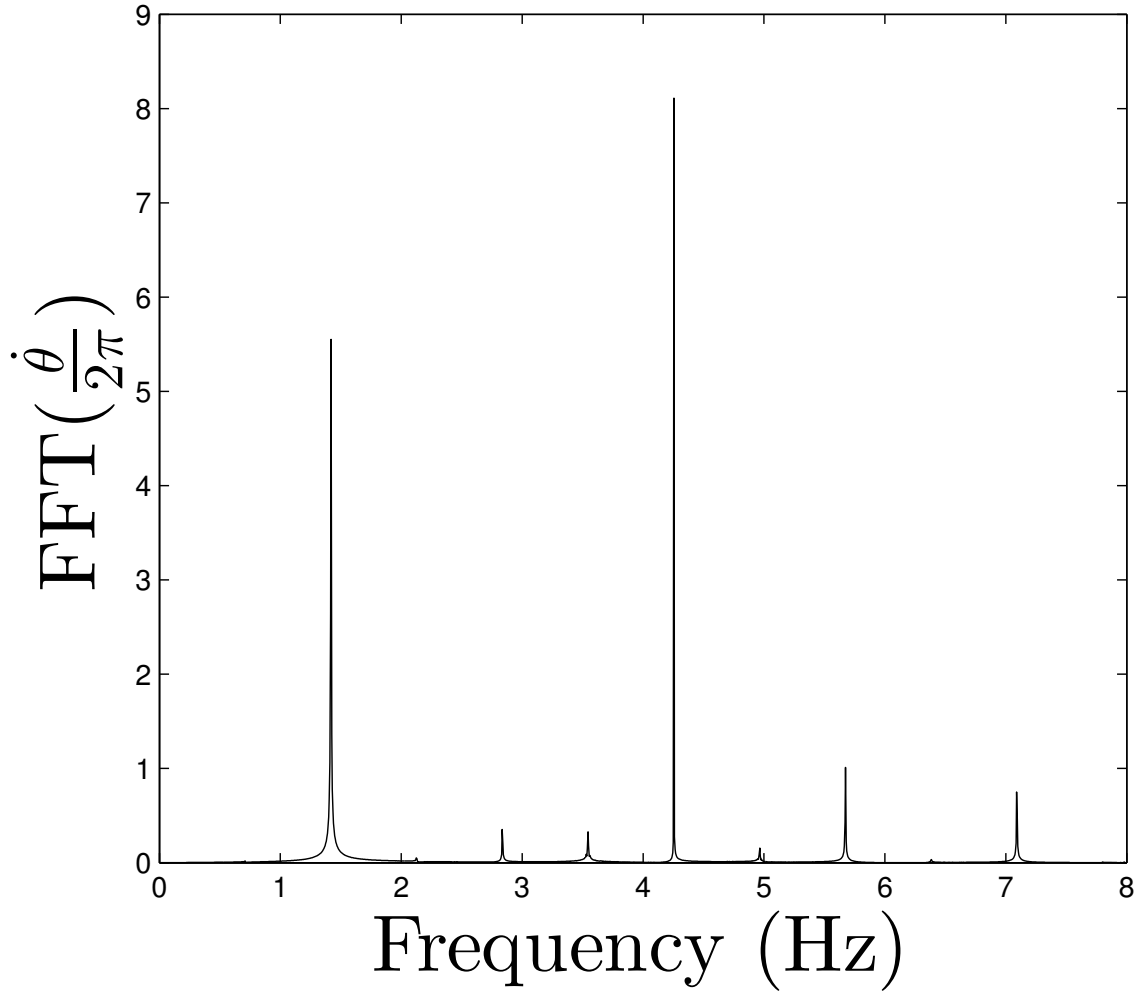

FIGURE 7.32: Frequency response, in terms of rotations per second, for the magnetic ball when excited by the subject running at 8 mph.

Table 7.3: Circular Harvester Theoretical Max Power

Mass (kg)	Speed (mph)	Max Power (W)	Avg. Power (W)
m	2	2m	0.02m
m	4	14.2m	1.1m
m	8	21m	3.2m
0.001	2	0.002	0.00002
0.001	4	0.0142	0.0011
0.001	8	0.021	0.0032
0.01	2	0.02	0.0002
0.01	4	0.142	0.011
0.01	8	0.21	0.032

7.4 Conclusions

The two-dimensional walking/running motion exhibited by athletes was studied by first implementing image processing software. After observing multiple subjects on a treadmill, the data obtained was recreated numerically. Commonality was shown for multiple subjects in both the frequency spectrum and in respective acceleration profiles. This data was then used as input excitations to a potential energy harvesting system. The equation of motion for this design was derived, its dimensions were chosen based on overall harvester performance, and multiple numerical simulations were performed to determine potential power output.

8

Summary, Conclusions, and Future Research

8.1 Summary and Conclusions

The research described in this document explores the nonlinear and multi-frequency dynamics of many systems which have potential applications to energy harvesting. The importance of utilizing the inherently nonlinear attributes of certain harvester designs, as well as ambient vibratory environments, is shown by comparing linear and nonlinear formulations. This research provides a foundation for potential future advances in the area of nonlinear energy harvesting.

Chapter 2 gave brief descriptions of the multiple theoretical methods commonly employed to analyze dynamical systems. This included Lagrange's equation, harmonic balance, and numerical continuation. Examples were shown on how to apply these methods to simple dynamical systems such as a harmonic oscillator, which laid the groundwork for implementing them for more complicated systems studied later.

The throughly researched area of linear energy harvesting was described in Chapter 3. Two energy harvesting systems that are often modeled linearly were shown. These two systems were the linear inertial harvester and the coupled electromechan-

ical harvester. The linear equations for these two systems were derived using some of the methods described in Chapter 2. The idea that linear energy harvesters are not practical for ambient systems was again shown.

Chapter 4 describes the mathematical models for different wave tank designs often used in experimental analysis. These designs include single and double-flap wavemakers, as well as the plunging mavemaker design that is used in the experimental investigations in multiple chapters. Additionally, the wave amplitude was tracked for multiple operating frequencies in order to observe any patterns present. From the obtained data, it was shown that the 'beach' used to minimize reflections was insufficient in size/damping ability.

Chapter 5 described the 2D nonlinear motion of an untethered spherical buoy when excited in a wave environment. The theoretical natural frequency was derived and shown to be accurate through numerical and experimental investigations. A full nonlinear analysis of the buoy was performed using analytical and numerical methods. Additionally, these results were compared to experimental investigations performed using the wave tank described in Chapter 4. The derived equations of motion were shown to be accurate by comparing an analytical solution, numerical simulation, experimental data, and numerical continuation. These solutions were compared to the equations of motion derived for a linear model, and it was shown that the linear model fails to accurately predict the complex motion of the buoy.

Chapter 6 performed all of the analysis from the previous chapter, now on a cylindrical buoy. In addition to the 2D motion, the cylinder was also allowed to rotate in the plane. As before, the theoretical natural frequency was derived and validated through numerical simulation. Certain parameters of the buoy, such as the mass and radius, were altered to show how they affect the natural frequency. A nonlinear analysis was performed using numerical and analytical methods. The 1D vertical motion was shown to be accurate using multiple techniques, including numerical

continuation, simulation, and an analytical solution. Then, the full 2D formulation was simulated numerically for different buoy masses and forcing frequencies to show the patterns exhibited in the motion.

The multi-frequency motion exhibited by athletes during running and walking was shown in Chapter 7. The motion was found experimentally by filming test subjects walking and running on a treadmill. Then, using the image processing software utilized in previous chapters, the 2D motion was analyzed. This motion was then recreated numerically, both to observe common patterns exhibited among different subjects, and to use as an input to numerical simulations of an applicable energy harvesting device. The design for this device was a chip with a circular track containing a magnetic ball. As the ball moves through the track, it interacts with the coil setup located in the center of the chip, providing a certain amount of theoretical power. The purpose of this device was to collect energy from the motion of the subject in order to power a transmitter. This could eventually be used to transmit certain attributes of the subjects motion, such as position and speed, in order to have records of the desired information.

8.2 Future Directions for Research

In addition to providing valuable data and overall trends for the topics discussed, this research creates new paths for possible future investigations. These potential research contributions are arranged by their relevance to the topics covered, including spherical and cylindrical buoy motion, walking/running athlete motion, and expanded energy harvester analysis.

8.2.1 Spherical Buoy

The spherical buoy was studied for multiple masses and forcing frequencies in the wave tank, though all analysis was two-dimensional. Some future directions include:

1. A full 3D analysis of the buoy motion. It is possible to get out-of-plane motion under specific forcing parameters and buoy dimensions. Therefore, it is beneficial from an energy harvesting standpoint to understand and utilize this additional motion.

2. Eccentric mass placement. In this research, the buoy was modeled with the center of mass located at the center of the buoy. However, the spherical buoy can see significant tilting motion if the mass is positioned away from the center, which was also seen in the cylindrical buoy chapter. Again, this could help in terms of energy harvesting.

8.2.2 Cylindrical Buoy

The cylindrical buoy was also studied for multiple masses and forcing frequencies. It was additionally allowed to rotated in the 2D plane. Some possible areas of future research include:

1. As with the spherical buoy, it would be beneficial to understand the full 3D motion of the cylindrical buoy. In experimental trials, significant out-of-plane motion was shown to arise for many buoy dimensions and forcing parameters. As mentioned previously, this could increase energy harvesting potential.

2. Eccentric mass placement analysis. Though an added eccentric mass was studied for the cylindrical buoy, no analysis was done on the effect of altering its placement. Changing the added mass location could have a large effect on the overall motion.

8.2.3 Athlete Motion

The two-dimensional motion of athlete walking/running dynamics was studied for multiple runners and speeds. Experimental data was taken indoors and on a treadmill

for each subject. Future research topics may include:

1. Full walking/running analysis. Experimental data was taken for subjects on a treadmill, both for ease of tracking and in order to more accurately calculate their speed. However, there is most likely some difference in how a runner may perform on a treadmill vs. in an actual running event. Therefore, it would be highly beneficial to design a tracking system that could move with the runner, which would allow for large amounts of more accurate data.

2. Expansion of analysis to triathletes. Focus was placed solely on the runner in this research, though the proposed device would be just as beneficial for other athletic events, such as cycling and swimming. It would therefore be of interest to study cyclist and swimmer motion in order to determine if the energy harvesting device is efficient in these scenarios, or if a new design must be studied.

8.2.4 Energy Harvester Analysis

The proposed energy harvester design was studied in two dimensions for multiple excitation inputs. These inputs were calculated from experimental data obtained for the running subjects. Future areas of research may include:

1. Magnetic interaction. Focus was placed on the dynamics of the harvester itself, and not the magnet-coil interactions that will eventually need to take place in order to harvest energy. This interaction, of course, needs to be studied. This analysis may also provide insights into the harvester design not seen in the dynamic analysis.

2. 3D harvester analysis. In addition to the 2D rotational movement, it may be beneficial to observe the effect of stacking these harvesters. Also, the interactions between each rotating magnet would be an interesting dynamics problem,

and could potentially lead to an increase in harvested energy if designed correctly.

Bibliography

[1] Emmanuel B. Agamloh, Alan K. Wallace, and Annette von Jouanne. Application of fluid-structure interaction simulation of an ocean wave energy extraction device. *Renewable Energy*, 33:748–757, 2008.

[2] Jose Henrique G.M Alves, Michael L. Banner, and Ian R. Young. Revisiting the pierson-moskowitz asymptotic limits for fully developed wind waves. *Journal of Physical Oceanography*, 33:1301–1323, 2003.

[3] M. Bartucelli, G. Gentile, and K. Georgiou. On the dynamics of a vertically driven damped planar pendulum. *Proceedings of the Royal Society of London. Series A,*, 47:3007–3022, 2001.

[4] S.P. Bastien and R.B. Sepe. Ocean wave energy harvesting for buoy sensors. *Energy Conversion Congress and Exposition*, pages 3718–3725, 2009.

[5] S.P. Beeby, R.N. Torah, M.J. Tudor, P. Glynne-Jones, T. O'Donnell, C.R. Saha, and S. Roy. A micro electromagnetic generator for vibration energy harvesting. *Journal of Micromechanics and Microengineering*, 17:1257–1265, 2007.

[6] S.P. Beeby, M.J. Tudor, and N.M. White. Energy harvesting vibration sources for microsystems applications. *Measurement Science and Technology*, 17:175–195, 2006.

[7] S. Bishop, D. Xu, and M. Clifford. Flexible control of the parametrically excited pendulum. *Proceedings: Mathematical, Physical and Engineering Sciences*, 452:1789–1806, 1996.

[8] Rob W. Bisseling and At L. Hof. Handling of imapct forces in inverse dynamics. *Journal of Biomechanics*, 39:2438–2444, 2006.

[9] S.Y. Boo. Linear and nonlinear irregular waves and forces in a numerical wave tank. *Ocean Engineering*, 29:475–493, 2002.

[10] E.B. Carpenter, J.W. Leonard, and S.C.S. Yim. Experimental and numerical investigations of tethered spar and sphere buoys in irregular waves. *Ocean Engineering*, 22:765–784, 1995.

[11] H. Cavendish. Experiments to determine the density of the earth. *Philosophical Transactions of the Royal Society of London*, 88:469–526, 1798.

[12] Jr. C.J. Galvin. Wave height prediction for wave generators in shallow water. *Tech Memo, U.S. Army, Coastal Engineering Research Center*, 4, 1964.

[13] M. Clifford and S. Bishop. Inverted oscillations of a drive pendulum. *Proceedings of the Royal Society of London. Series A*, 454:2811–2817, 1997.

[14] Alex D.D. Craik. The origins of water wave theory. *Annual Review of Fluid Mechanics*, 36:1–28, 2004.

[15] Jeremy C. O'Connor Cristopher L. Vaughan, Brian L. Davis. *Dynamics of Human Gait*. Kiboho Publishers, 1999.

[16] Robert G. Dean. *Water Wave Mechanics for Engineers and Scientists*. World Scientific, Singapore, 1991.

[17] J.M. Donelan. Biomechanical energy harvesting: Generating electricity during walking with minimal user effort. *Life Science*, 319, 2008.

[18] B.D. Dore. On mass transport velocities due to progressive waves. *Department of Mathematics, University of reading*, 1976.

[19] D.S. Dugdale. Stability of a floating cylinder. *International Journal of Engineering Science*, 42:691–698, 2004.

[20] J.P. Schaffer E.J. Shaughnessy, I.M. Katz. *Introduction to Fluid Mechanics*. Oxford University Press, 2005.

[21] Tzeno V. Galchev. *Energy Scavenging from Low Frequency Vibrations*. PhD thesis, The University of Michigan, 2010.

[22] Oded Gottlieb and Solomon C.S. Yim. Nonlinear dynamics of a coupled surge-heave small-body ocean mooring system. *Ocean Engineering*, 24:479–495, 1997.

[23] V. Graizer. Intertial seismometry methods. *Izvestiya, Earth Physics*, 27:51–61, 1991.

[24] V. Graizer. Effect of tilt on strong motion data processing. *Soil Dynamics and Earthquake Engineering*, 25:197–204, 2005.

[25] Gael Sebald Sebastien Pruvost Mickael Lallart Akram Khodayari Guyomar, Daniel and Claude Richard. Energy harvesting from ambient vibrations and heat. *Journal of Intelligent Material Systems and Structures*, 20, 2009.

[26] J. Hubbard. The forced damped pendulum: Chaos, complication and control. *The American Mathematical Monthly*, 106:741–758, 1999.

[27] Mohamed Iskandarani and Philip L.F. Liu. Mass transport in wave tank. *Journal of Waterway, Port, Coastal, and Ocean Engineering*, 119:88–104, 1993.

[28] D. Jordan and P. Smith. *Nonlinear Ordinary Differential Equations: An Introduction for Scientists and Engineers*. Oxford, 2007.

[29] E.B Agamloh et al K. Rhinefrank. Novel ocean energy permanent magnet linear generator buoy. *Renewable Energy*, 31:1279–1298, 2006.

[30] Hiroshi Ban Kiyoshi Kobayashi Kitazawa, Shoichi. Energy harvesting from ambient rf sources. *IMWS-IWPT2012 Proceedings*, 2012.

[31] Hyeongseok Ko and Norman I. Badler. Animation human locomotion with inverse dynamics. *IEEE Computer Graphics*, pages 50–59, 1996.

[32] Bart Koopman, Henk J. Grootenboer, and Henk J. de Jongh. An inverse dynamics model for the analysis, reconstruction, and prediction of bipedal walking. *Journal of Biomechanics*, 28:1369–1376, 1995.

[33] W.M. Kusumawinahyu, N. Karjanto, and G. Klopman. Linear theory for single and double flap wavemakers. *J. Indones. Math. Soc. (MIHMI)*, 12(1):41–57, 2006.

[34] J. Kymissis, C. Kendall, J. Paradiso, and N. Gershenfeld. Parasitic power harvesting in shoes. In *Second International Symposium on Wearble Computers*, 1998.

[35] S. Lenci, E. Pavlovskaia, G. Rega, and M. Wiercigroch. Rotating solutions and stability of a parametric pendulum by perturbation method. *Journal of Sound and Vibration*, 310:243–259, 2008.

[36] Huan Lin and Solomon C.S. Yim. Coupled surge-heave motions of a moored system. 1: Model calibration and parametric study. *Journal of Engineering Mechanics*, 132(6):671–680, 2006.

[37] Huan Lin, Solomon C.S. Yim, and Oded Gottlieb. Experimental investigation of response stability and transition behaviour of a nonlinear ocean structural system. *Ocean Engineering*, 25(4-5):323–343, 1998.

[38] M.S. Longuet-Higgins. Mass transport in water waves. *Philosophical Transactions of the Royal Society of London. Series A, Mathematical and Physical Sciences*, 245(903):535–581, 1953.

[39] B. Mann and M. Koplow. Symmetry breaking bifucations of a parametrically excited pendulum. *Nonlinear Dynamics*, 46:427–437, 2006.

[40] Loreto Mateu, Cosmin Codrea, Nestor Lucas, Markus Pollak, and Peter Spies. Human body energy harvesting thermogenerator for sensing applications. In *International Conference on Sensor Technologies and Applications*, 2007.

[41] Loreto Mateu and Francesca Moll. Optimum piezoelectric bending beam structures for energy harvesting using sole inserts. *Journal of Intelligent Material Systems and Structures*, 16:835–845, 2005.

[42] Loreto Mateu and Francisco de Borja Moll Echeto. Review of energy harvesting techniques and applications for microelectronics. In *Proceedings of the SPIE Microtechnologies for the New Millenium*, 2005.

[43] Clark C. McGehee, Zach C. Ballard, and Brian P. Mann. Horizontal pendulum with sudden changes in platform tilt. In *Proceedings of the ASME 2011 International Design Engineering and Technical Conferences and Computers and Information in Engineering Conference*. ASME, DETC2011/VIB-48423, August 2011.

[44] L.M. Milne-Thompson. *Theoretical Hydrodynamics*. Macmillan and Co LTD, 1962.

[45] P.D. Mitcheson, E.M. Yeatman, Homes A.S. Rao, G.K., and T.C. Green. Energy harvesting from human and electronic machine motion for wireless electronic devices. *Proceedings of the IEEE*, 96(9):1457–1486, 2008.

[46] METIN ERD MILOS KOSTIC KEITH COBRY MICHAEL KROENER MOSER, ANDRE and PETER WOIAS1. Thermoelectric energy harvesting

from transient ambient temperature gradients. *Journal of ELECTRONIC MATERIALS*, 41, 2012.

[47] Penglin Niu, Patrick Chapman, Raziel Riemer, and Xudong Zhang. Evaluation of motions and actuation methods for biomechanical energy harvesting. In *35th Annual IEEE Power Electronic Specialists Conference*, 2004.

[48] Kunihiro Ogihara. Thoretical analysis on the transverse motion of a buoy by a surface wave. *Applied Ocean Research*, 2(2):51–56, 1980.

[49] Takumi Ohyama and Kazuo Nadaoka. Development of a numerical wave tank for analysis of nonlinear and irregular wave field. *Fluid Dynamics Research*, 8:231–251, 1991.

[50] J P Owen and W S Ryu. The effects of linear and quadratic drag on falling spheres: an undergraduate laboratory. *European Journal of Physics*, 26:1085–1091, 2005.

[51] Benjamin A.M. Owens and Brian P. Mann. Linear and nonlinear electromagnetic coupling models in vibration-based energy harvesting. *Journal of Soun*, 331:922–937, 2012.

[52] Joseph A. Paradiso and Thad Starner. Energy scavenging for mobile and wireless electronics. *Pervasive Computing*, 4(1):18–27, 2005.

[53] R. Peters. Mechanically adjustable balance and sensitive tilt meter. *Measurements of Science and Technology*, 1:1131–1135, 1990.

[54] K. Ryan, C.J. Pregnalato, M.C. Thompson, and K. Hourigan. Flow-induced vibrations of a tethered circular cylinder. *Journal of Fluid Mechanics*, 19:1085–1102, 2004.

[55] Si Mohamed Sah and Brian P. Mann. Stability of a pivoting fluid-filled container. In *Proceedings of the ASME 2011 International Design Engineering and Technical Conferences and Computers and Information in Engineering Conference*, 2011.

[56] C.R. Saha, N. Wang T. O'Donnell, and P. McCloskey. Electromagnetic generator for harvesting energy from human motion. *Sensors and Actuators A: Physical*, 147:248–253, 2007.

[57] Robert E. Salomon. Rocking buoy wave energy converter. *Ocean Engineering*, 16:319–324, 1989.

[58] T. Sarpkaya and M. Storm. In-line force on a cylinder translating in oscillatory flow. *Applied Ocean Research*, 7:188–196, 1985.

[59] J. Scmitt and P. Bayly. Bifucations in the mean angle of a horizontally shaken pendulum: Analysis and experiment. *Nonlinear Dynamics*, 15:1–14, 1999.

[60] Samuel Stanton. *Nonlinear Electroelastic Dynamical Systems for Inertial Power Generation*. PhD thesis, Duke University, 2011.

[61] T. Starner. Human-powered wearable computing. *IBM Systems Journal*, 35:618–629, 1996.

[62] K.E. Steele and D.W. Wang. Question of the pitch-roll buoy response to ocean waves as a simple harmonic oscillator. *Ocean Engineering*, 31:2121–2138, 2004.

[63] N.G. Stephen. On energy harvesting from ambient vibration. *Journal of Sound and Vibration*, 293:409–425, 2006.

[64] Robert H. Stewart. Ocean-wave spectra. 2006.

[65] C.C. Tung. Total wave force on cylinder considering free surface fluctuation. *Applied Ocean Research*, 18:37–43, 1996.

[66] A. Umar and T.K. Datta. Nonlinear response of a moored buoy. *Ocean Engineering*, 30:1625–1646, 2003.

[67] Hohlfeld Dennis Veld, Bert Op het and Valer Pop. Harvesting mechanical energy for ambient intelligent devices. *Information Systems*, 11:7–18, 2009.

[68] B.G. Wade and M. Dwyer. Application of morison's equation to fixed offshore platforms. *Journal of Petroleum Technology*, 30(3):pp. 447–454, 1978.

[69] Jan Erik H. Weber, Goran Brostrom, and Oyvind Saetra. Eulerian versus lagrangian approaches to the wave-induced transport in the upper ocean. *Journal of Physical Oceanography*, 36:2106, 2006.

[70] J F Wilson. *Dynamics of Offshore Structures*. John Wiley & Sons, Inc., 2003.

[71] Julian Wolfram. On alternative approaches to linearization and morison's equation for wave forces. *Proceedings: Mathematical, Physical and Engineering Sciences*, 455(1988):2957–2974, 1999.

[72] K. Worden, P. K. Stansby, G. R. Tomlinson, and S. A. Billings. Identification of nonlinear wave forces. *Journal of Fluids and Structures*, 8(1):19 – 71, 1994.

[73] G.X. Wu and R. Eatock Taylor. Hydrodynamic forces on submerged oscillating cylinders at forward speed. *Proceedings of the Royal Society of London. Series A, Mathematical and Physical Sciences*, 414:149–170, 1987.

[74] X. Xu and M. Wiercigroch. Approximate analytical solutions for oscillatory and rotational motion of a parametric pendulum. *Nonlinear Dynamics*, 47:311–320, 2007.

[75] Felix E. Zajac, Richard R. Neptune, and Steven A. Kautz. Biomechanics and muscle coordination of human walking part 1: Introduction to concepts, power transfer, dynamics and simulations. *Gait and Posture*, 16:215–232, 2002.

[76] D. Zhou and W.Q. Liu. Bending-torsion vibration of a partially submerged cylinder with an arbitrary cross-section. *Applied Mathematical Modelling*, 31:2249–2265, 2007.

[77] Huiyu Zhou and Suosheng Hu. Huma motion tracking for rehabilitation - a survey. *Biomedical Singla Processing and Control*, 3:1–18, 2008.

Biography

Zach Ballard was born on April 1st, 1986 in Dallas, Texas. He received his high school diploma from Rockwall High School in 2005. After graduating with a Bachelors of Science in Mechanical Engineering at the University of Texas at Austin in 2009, he was admitted to the graduate program at Duke University to continue his education in mechanical engineering under the supervision of Dr. Brian Mann. He received his Masters of Science in the Fall of 2011, and plans to graduate with his PhD in the Spring of 2013.